The Role of Gold-Graphene Hybrid Nanostructure on Promoting Localized Surface Plasmonic Resonance Sensor Performance

by

Raed Alharbi

A thesis
presented to the University of Waterloo
in fulfillment of the
thesis requirement for the degree of
Doctor of Philosophy
in
Mechanical and Mechatronics Engineering

Waterloo, Ontario, Canada, 2020

This thesis consists of material all of which I authored or co-authored: see Statement of Contributions included in the thesis.

This is a true copy of the thesis, including any required final revisions, as accepted by my examiners.

I understand that my thesis may be made electronically available to the public.

Examining Committee Membership

The following served on the Examining Committee for this thesis. The decision of the Examining Committee is by majority vote.

Internal-External Member	Professor Michal Bajcsy Department of Electrical & Computer Engineering, University of Waterloo, Canada
Supervisor	Professor Mustafa Yavuz Department of Mechanical & Mechatronics Engineering, University of Waterloo, Canada
Internal Member	Professor Kevin Musselman Department of Mechanical & Mechatronics Engineering, University of Waterloo, Canada
Internal Member	Professor Eihab Abdul-Rahman Department of Systems Design Engineering, University of Waterloo, Canada
External Examiner	Professor Yu Sun Department of Mechanical and Industrial Engineering, University of Toronto, Canada

Statement of Contributions

This thesis included co-authored work (published, under review, & to be submitted manuscripts) and the following is the details of the contribution for each author.

Sections 1.4 & 1.5: Part of a published paper in which Raed Alharbi conducted the research and wrote the manuscript; Mustafa Yavuz and Mehrdad Irannejad were the research supervisors.

*Alharbi, R., Irannejad, M., & Yavuz, M. (2019). A Short Review on the Role of the Metal-Graphene Hybrid Nanostructure in Promoting the Localized Surface Plasmon Resonance Sensor Performance. Sensors, 19(4), 862. (**Published, Sec. 1.4 & 1.5**)*

Chapter 2 (Published) & Chapter 3 (Published): Raed Alharbi: conducted the research and wrote the manuscript. Mustafa Yavuz and Mehrdad Irannejad were the research supervisors.

*Alharbi, R., Irannejad, M., & Yavuz, M. (2017). Gold-graphene core-shell nanostructure surface plasmon sensors. Plasmonics, 12(3), 783-794. (**Published, Ch 2**)*

*Alharbi, R., Irannejad, M., & Yavuz, M. (2017). Au-Graphene Hybrid Plasmonic Nanostructure Sensor Based on Intensity Shift. Sensors, 17(1), 191. (**Published, Ch 3**)*

Chapter 4 (Planned for publication): Raed Alharbi: conducted the research and wrote the manuscript. Mustafa Yavuz was the research supervisor.

*Alharbi, R, & Yavuz, M. "Direct Deposition of Graphene Sheets over Gold Nano-Disks Array for Enhancing Localized Surface Plasmon Resonance Sensor Performance" (**Planned for publication**)*

Chapter 5 (Published): Raed Alharbi: conducted the research and wrote the manuscript. Mustafa Yavuz was the research supervisor.

*Alharbi, R., & Yavuz, M. (2019, June). Promote Localized Surface Plasmonic Sensor Performance via Spin-Coating Graphene Flakes over Au Nano-Disk Array. In Photonics (Vol. 6, No. 2, p. 57). Multidisciplinary Digital Publishing Institute. (**Published, Ch 5**)*

Chapter 6 (Submitted): Raed Alharbi: device fabrication, simulation work, wrote the manuscript; Abdullah Alshehri: device fabrication; Victor Wong: SNOM experiment & edited manuscript; Giovanni Fanchini and Mustafa Yavuz: manuscript editors & research supervisors.

*Raed Alharbi, Victor Wong, Abdullah H. Alshehri, Giovanni Fanchini, & Mustafa Yavuz "Scanning near-field optical microscopy assisted design of sensing enhancement devices based on localized surface plasmon resonance". (**Submitted to Ann Phys, Wiley-VCH, Oct. 2019**)*

Abstract

Localized surface plasmon resonance (LSPR) sensors have a wide range of applications, from medical diagnostics to environmental monitoring. In addition, the simplicity of the excitation method leads to simplicity in the sensor setup, which is helpful for device minimization, and may also help in system cost reduction. Generally, LSPR sensors suffer from low performance, which limits their commercialization. In earlier decades, researchers attempted various methods to overcome this problem; however, recently, the integration of plasmonic material, "gold", with a 2D material, "graphene", has been found to be a promising way to enhance light-matter interaction, and hence promote LSPR sensor performance.

In this work, four different novel gold (Au)-graphene (G) hybrid nanostructure schemes are proposed and their sensing performance, as a plasmonic sensor, is studied and evaluated numerically using the Finite Difference Time Domain (FDTD) method. The first gold-graphene hybrid nanostructure studied in this project is a periodic array of Au-G spherical core-shell hybrid nanoparticles (NP) placed on top of a quartz substrate. The second is formed by embedding the medium between Au NPs in an array with multilayers of graphene sheets. Third, is direct deposition of a graphene film on top of a Au NP array and finally, spin-coating graphene flakes on top and between a Au NP array. Based on numerical work, the maximum value of sensitivity and the figure of merit of the LSPR sensor achieved here are 4380 nm/RIU and 857.9, respectively, which is very high and competitive with other studies, and presents the Au-G hybrid LSPR sensor as a promising sensor in a variety of applications such as bio-sensing, thereby enhancing its commercialization. At the end of this work, near-field characterization using a near-field scanning optical microscope (NSOM) is applied to the fabricated Au NP array to study light-Au NP interaction and to illustrate how the structure can be utilized as an LSPR sensor.

Acknowledgements

I would like to thank all the people who made this possible.

Dedication

This is dedicated to

My father “Abdullah”

My mother “Bakita”

My wife “Hind”

My little man “Abdullah”

My brothers and my sisters

Table of Contents

List of Figures

List of Tables

List of Abbreviations

SP	Surface plasmon
SPR	Surface plasmon resonance
SPP	Surface Plasmon Polaritons
LSPR	Localized surface plasmons resonance
PSPR	Propagated surface plasmon resonance
∅	Resonance angle
RI	Refractive index
$FWHM$	Full-width at half maximum
S	Sensitivity
FOM	Figure of merit
NP	Nanoparticle
RIU	Refractive index unit
G	Graphene
FDTD	Finite difference time domain
FIB	Focused ion beam
ND	Nano-disk
Vis	Visible
UV	Ultra-Violet
NIR	Near infra-red
IR	Infra-red
CVD	Chemical vapor deposition

Chapter 1 Introduction

1.1 Background

In 1959, Richard Feynman, an American theoretical physicist, described nanotechnology in his famous lecture titled "There's Plenty of Room at the Bottom"[1]. He explains it as a technology that deals with materials, systems, and devices at the nanoscale range (1-100 nm). Following Feynman's talk, the direction of nanoscience has been successfully predicted, dealing with the idea of miniaturization of devices in various applications. The main aspect that attracts many researchers from around the world is the observation of altered properties in a given material when its size is reduced from bulk to nano-scale. This phenomenon has led to the development of novel materials and devices with significant impact on our society. Today's nanotechnology is well-established in industry and different areas of the research field.

The Roman glass cup, known as the Lycurgus cup, which dates to the fourth century (Fig. 1.1) [2], is an example of absorption of incident electromagnetic waves and emitting light at resonance wavelength. When the cup is illuminated externally with visible light, it appears a jade-green color, while it is a deep ruby-red when illuminated interiorly. It has been shown that the cup contains an alloy of gold (31.2%)-silver (66.2%)-copper (2.6%) nanoparticles up to 100 nm in size embedded in the glass; the particles scatter and absorb incident light at different visible wavelengths [2]. During that era, Roman glassmakers produced these objects with various colors, without awareness of the nanoparticles they were producing. However, the interaction of light with metal nanoparticles leads to a phenomenon called localized surface plasmon resonance (LSPR), which has been introduced for various sensing applications, such as bio-sensing. In the

following section, the physics of LSPR, and how it has been used for sensing purposes, is further discussed.

Figure 1.1: Lycurgus (Roman) cup as it is illuminated from outside (left) and inside (right) [2]

1.2 Localized Surface Plasmon Resonance (LSPR) Sensor

Prior to discussing the LSPR sensor, it is preferable to initially consider the physical phenomena called surface plasmon resonance (SPR), which is observed when metal film is illuminated with polarized light under total internal reflection conditions. The light should be p-polarized light (i.e. polarization occurs parallel to the plane of incidence) in order to excite the surface free electrons in the metal film [3]. The light is partly reflected and partly refracted when it comes from a high-to-low refractive index, until a specific incident angle called the critical angle: the light above this angle is then totally internally reflected [4]. At a total internal reflection condition, an evanescent wave penetrates into the lower refractive index medium (detection area in Fig. 1.2) and where intensity diminishes exponentially with distance from the boundary. By placing a thin metal film

on top of a prism, the evanescent wave then interacts with free electrons in the metal thin film, generating a plasmonic wave at the surface of the metal layer [4].

At a particular angle (above the critical angle), the resonance condition occurs when the incident light wave vector match with the moving electron (plasmons) vector, and that angle is called the "resonance angle" [4]. At this resonance condition, some of the photon energy of the incident light is transmitted to the plasmons, and this appears as a dip in the reflection spectrum. As surface plasmons propagate at the metal-dielectric interface, any change in the dielectric property (i.e. refractive index) of the medium above the metal film surface will alter the resonance condition and result in a shift in the resonance angle. Therefore, this mechanism allows the SPR phenomena to be utilized for sensing applications. Due to the propagation of surface plasmons at the metal-dielectric interface, this sensor is referred to as a propagating surface plasmon resonance (PSPR) sensor and its performance can be quantified through the sensitivity (S) and figure of merit (FOM) assessments using equations 1.1 and 1.2 [5].

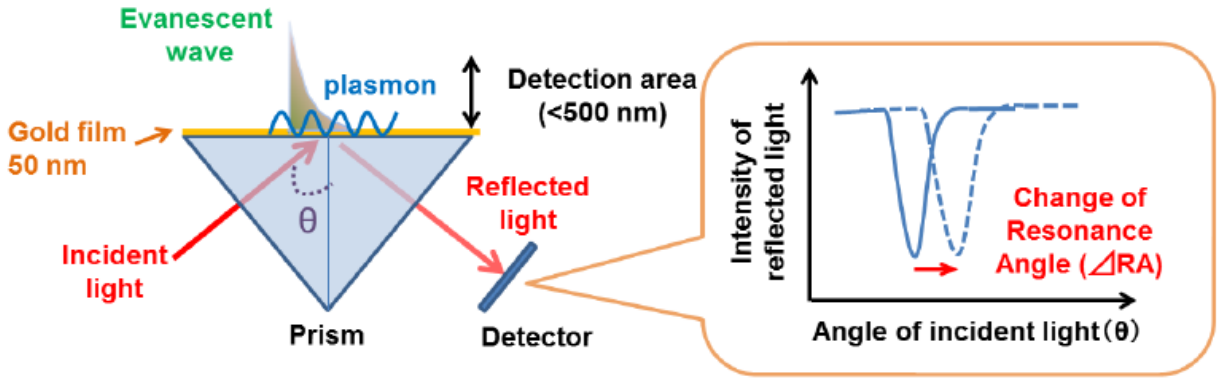

Figure 1.2: Schematic representation of the PSPR sensing mechanism [4]

$$S = \frac{\Delta \emptyset}{\Delta n} \qquad 1.1$$

$$FOM = \frac{S}{FWHM} \qquad 1.2$$

Where $\Delta\emptyset$ and Δn are the amount of resonance angle shift and the change that occurs in the refractive index of the sensing medium, respectively. $FWHM$ refers to full-width at half-maximum where the resonance band width (using incident angle) is measured at half of the maximum recorded reflection.

When the metal film is reduced to a metal nanoparticle (NP) layer, excited plasmons are localized in the vicinity of the NP, which leads to another phenomena called localized surface plasmonic resonance (LSPR) that can be explained using Mie theory [6]. In 1908, Gustav Mie described the interaction between the electromagnetic wave and metal nanoparticles by solving Maxwell's equations analytically for a spherical metal nanoparticle in a homogenous medium and deriving the optical extinction (σ_{ext}) for the metal NP with radius smaller than the wavelength of the incident wave ($2r << \lambda$) as in equation 1.3 [6].

$$\sigma_{ext}(\lambda) = \frac{24\pi^2 r^3 \varepsilon_d^{3/2} N}{\lambda \ln(10)} \frac{\varepsilon_i(\lambda)}{(\varepsilon_r(\lambda)+2\varepsilon_d)^2+\varepsilon_i(\lambda)^2} \qquad 1.3$$

where N is the electron density, λ is the incident wavelength, ε_d is the permittivity of the dielectric medium, ε_r and ε_i are the real and imaginary parts of the dielectric constant of metal NP, respectively. By applying a uniform static electric field around a metallic nanoparticle, it can be considered as an electric dipole, and its polarizability, $\alpha(\lambda)$, can be given [6] by:

$$\alpha(\lambda) = 4\pi r^3 \frac{\varepsilon(\lambda)-\varepsilon_d(\lambda)}{\varepsilon(\lambda)+2\varepsilon_d(\lambda)} \qquad 1.4$$

Where $\varepsilon(\lambda)$ is a complex dielectric constant of the metal NP, r is the radius of the NP and $\varepsilon_d(\lambda)$ is the permittivity of the dielectric medium. When $\varepsilon(\lambda) \approx -2\varepsilon_d(\lambda)$, the denominator approaches zero, hence the maximum polarization that can be achieved at the resonance frequency of a dipolar LSP can be determined by equation 1.5 [7]:

$$\omega_{LSP} = \frac{\omega_p}{\sqrt{1+2\varepsilon_d}} \qquad 1.5$$

In equation 1.5, ω_p is the plasma frequency of gold and ε_d is the permittivity of the surrounding medium. At a resonance frequency, dipole free electrons move away from their equilibrium position, as shown schematically in Fig. 1.3. The electrostatic interaction between the displaced electrons and atomic core acts as a restoring force that results in a localized plasmon oscillation.

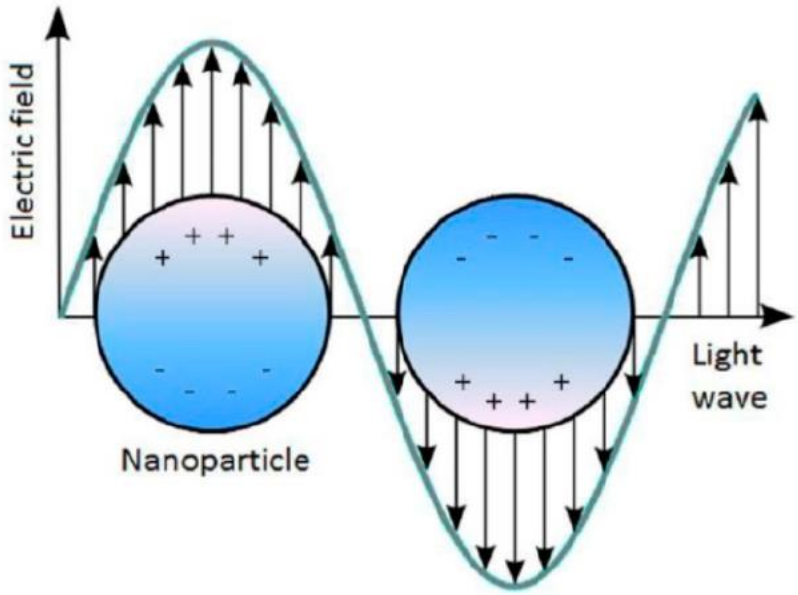

Figure 1.3: Schematic diagram of the interaction of gold NP with incident electric field [8].

When the dielectric permittivity of the surrounding medium changes, for example, due to surface immobilization, the LSP resonance condition is altered. Increasing the dielectric permittivity of the surrounding medium causes screening of the surface charges, which weakens the restoring force of the electrons [9]. Therefore, less energy is required to excite electrons, and this causes a redshift in the resonance wavelength. Equation 1.5 clearly shows that when the dielectric permittivity of the surrounding medium increases, the frequency is decreased, and as known, the wavelength is inversely proportional to frequency, thus an increase or redshift in the

resonance wavelength occurs. Therefore, metal NPs can be used as an active material in an LSPR sensor where its sensitivity depends on the polarizability and strength of the restoring force of the metal NP, which is a function of the NP's material type, size, and shape.

In an LSPR sensing experiment, as shown in Fig. 1.4, the nanostructure is illuminated with light from the bottom and the transmission or absorption spectrum is obtained.

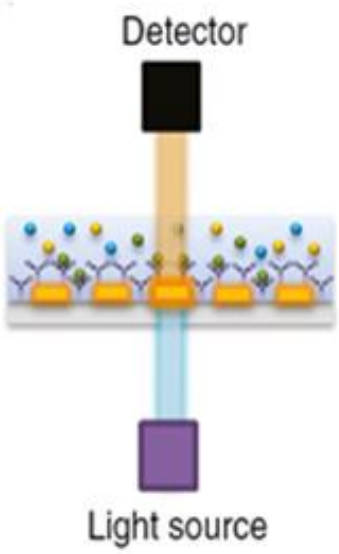

Figure 1.4: Schematic representation of the LSPR sensor [10]

Therefore, when the refractive index of the sensing medium is changed, both the resonance wavelength and intensity values change, and then the sensor performance (S and FOM) can be assessed, based on either intensity or resonance wavelength shift as summarized in equations 1.6 – 1.9 below [11].

$$S_\lambda = \frac{\Delta\lambda}{\Delta n} \ (nm/RIU) \qquad (1.6)$$

$$S_I = \frac{\Delta I}{\Delta n} \ (RIU^{-1}) \quad (1.7)$$

$$FOM_\lambda = \frac{S_\lambda}{\text{FWHM}} \quad (1.8)$$

$$FOM_I = \frac{S_I}{I_{ref.}} \quad (1.9)$$

In equations 1.6 – 1.9, $\Delta\lambda$ is the change in the resonance wavelength (nm), ΔI is the change in intensity, and S_λ, FOM_λ , S_I , FOM_I are sensitivity and figure of merit based on wavelength and intensity shift, respectively. FWHM in Eq. 1.8 can be measured using the wavelength in the optical spectrum of the nanostructure instead of the incident angle as in Eq 1.2.

1.3 Advantages of the LSPR sensor

The LSPR sensor offers a simple optical configuration [12]. In a PSPR system, the source and detector must be positioned at a specific angle to obtain a correct signal. For this reason, in addition to the complexity of the PSPR system, it is therefore less robust to withstand the expected vibrations and mechanical noise during an experiment [13]. On the other hand, an LSPR sensor is angle-independent, and plasmons can be excited at any angle, which makes it more robust against experimental noise and may help in system cost reduction, as there is no need to revisit any source of vibration and mechanical noise as in a PSPR sensor. In addition, there is simplicity in the setup of the experiment using normal incident configuration. Therefore, as the LSPR sensor requires simple experimental setup, it offers a capability for miniaturization and integration with

chips [12]. LSPR sensors also offer label-free [14] and real-time detection [15], in addition to multiplexed and microfluidics capability [16] as for PSPR sensors.

The PSPR sensor offers a high FOM that could reach 292 [17] and is commonly used commercially in bio-sensing applications [13]. However, in the PSPR sensor, ~ 10 um x 10 um is the chip area required for a sensing experiment [13]. This requirement limits this type of sensor in that it lacks localized sensing volume. The LSPR sensor offers a localized sensing volume where a single NP or a few NPs can be used as probes for detection. Thus, these plasmonic NPs with proper functionalization can be used as an effective biosensor in various applications, such as an immunosensor [18] and detecting Deoxyribonucleic acid (DNA) hybridization [19]. A sensor's detection limit is defined as the minimum concentration of analyte that can be detected where the lower limit is preferred. An LSPR sensor presents a better small molecule sensitivity, which is an indication of a better detection limit compared to a PSPR sensor [13]. Lower detection limits are required in bio-applications, such as in the detection of cancer at an early stage. For instance, carcinoembryonic antigen (CEA) is a human cancer-associated antigen and a tumor biomarker for the diagnosis of breast tumors. The threshold level of this protein in healthy adult human blood serum is 3-5 ng/ml, and detection sub ng/ml is required for monitoring this protein's level and detection of cancer at an early stage [20]. Therefore, as LSPR with localized sensing volume can present a low-detection limit, it is a promising technology for many biosensing applications. However, low-sensing performance limits its chance to be a commercialized technology due to low penetration depth of the plasmon field in the dielectric (sensing) medium. As shown in Fig. 1.5a, due to localization of plasmon oscillation in the gold nanosphere, penetration depth of the plasmon field in the dielectric medium is much smaller than in the case of an SPR sensor, Fig. 1.5b, and thus lower bulk-sensing performance results in an LSPR sensor [21].

For example, penetration depth in an LSPR sensor may reach 30 nm, while in an SPR sensor it could reach a few hundred nm [21].

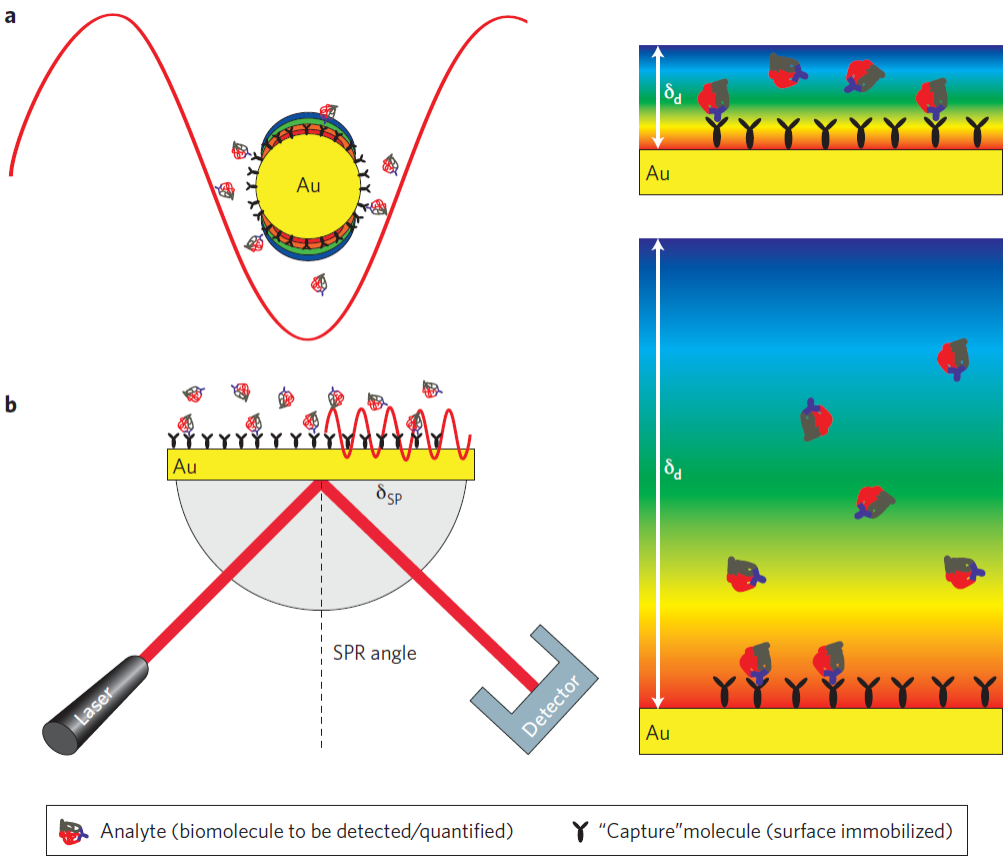

Figure 1.5: Schematic representation of LSPR sensor (a) and SPR sensor (b) showing penetration depth for both cases [21]

In previous decades, different approaches have been applied to the LSPR sensor to overcome its performance issues, as summarized in the following two sections.

1.4 Different Approaches Used to Enhance LSPR Sensor Performance

The performance of plasmonic sensors is related to the amount of loss in metallic nanostructure upon excitation. For example, using a metallic nanostructure with a high optical loss results in

broadening the resonance plasmonic band (absorption) due to an increase in scattering [22] and hence, the FOM of the sensor is decreased. It is known that silver has lower absorption loss than gold or copper [23]. Gold and copper are nevertheless considered to be low-loss materials, close to silver, when compared with aluminum, which has the highest losses in the visible spectrum [23]. A plasmonic sensor, e.g., an LSPR sensor, requires a material that has lower losses in order to achieve better refractive index sensing performance. In comparing gold and silver, silver offers superior sensitivity [24,25]. Upon using a spherical NP with a diameter of 60 nm, silver exhibits better sensitivity (160 nm/RIU) (i.e. RIU: refractive index unit) compared to that of gold (60 nm/RIU). However, the optical loss of the material is not the only physical property that needs to be considered in the design of an LSPR sensor. Compatibility of the sensor with the sensing medium is also essential. If the material used in an LSPR sensor becomes corroded in an aqueous medium or oxidized in the air, the refractive index sensitivity diminishes significantly [26]. Therefore, while gold has higher absorption loss than silver, it is preferred in most LSPR applications. Silver [27] and other metals such as copper [28], aluminum [29], or metal oxides such as zinc oxide [30], experience corrosion in aqueous mediums and oxidize in air, which limits their application in LSPR sensor engineering. In addition to the NP material type used in LSPR sensors, NP size also affects the refractive index sensitivity of sensors. Particle size affects the position of the surface plasmon peak, and it shifts towards longer wavelengths upon increasing the size of NPs. It has been verified that the SP peak of Au NPs can be redshifted up to 60 nm upon increasing the particle radius from 10–100 nm [31]. By examining the extinction equation 1.3, the radius of the NP is linearly related to the wavelength, and an increase in the size of the NP leads to resonance at longer wavelengths. Longer wavelength resonance is reported [32] to exhibit better sensitivity; however, increasing NP size causes increased scattering, and thus, broadens the

resonance band [22] which is not conducive for the FOM of the sensor. Therefore, tuning LSPR performance from the NP size side could be done in two ways: creating longer wavelength resonance to obtain superior sensitivity, or decreasing NP size to reduce FWHM to obtain better FOM. In addition, this is an indication of the high level of tunability of plasmonic properties of nanostructures, and shows that NP size must be carefully considered so as to achieve better sensitivity and FOM in plasmonic sensors.

The shape of a NP is also used as a tunable parameter to improve LSPR sensor performance. Changing the shape of NPs causes a resonance peak shift [33]. Tuning particle shape is a method used to tune the wavelength of resonance at longer wavelengths, and hence, optimize the sensitivity of an LSPR sensor. Mock et al. studied the effect of different shapes (sphere, cube, and triangle) of silver NPs on the sensitivity of a single NP to changes in the refractive index of surrounding medium [24]. They reported that the triangular NP exhibited greater sensitivity (i.e., 350 nm/RIU) than a spherical NP (i.e., 160 nm/RIU). Sun et.al [25] showed that a gold nanoshell shows higher sensitivity (i.e., 406 nm/RIU) than a gold spherical NP with a sensitivity of 60 nm/RIU. The main reason for observing higher sensitivity in triangular [24], nanoshell [25], and nanocube [34] structures relative to the spherical NPs [35] is due to the sharper edges of these NPs, which increase the intensity of the localized electric field around the NPs. Changing the aspect ratio also helps to produce multi-modal resonances at longer wavelengths, thus increasing sensor sensitivity. Hanarp et al. studied nanodisc structures with aspect ratios of 1:1–5:1 at refractive indices of 1.30–1.50 [36]. Greater resonance shift was observed in the case of 5:1 than in the case of 1:1 aspect ratio, which offers better sensor performance. Enhancement in sensitivity is acquired due to stronger excitation resulting from the elongated nanodisc resonance mode [36]. Aspect ratio is therefore another powerful key used to tune the plasmonic properties of a nanostructure.

By using two or more NPs separated by a specific distance in one-, two-, or three-dimensions, interaction between these incident waves and the excited surface plasmon wave from NPs results in an additional shift of resonance wavelength to the red region because of coupling interaction, which enhances sensor sensitivity [37]. Erik et al. [38] studied the effect of inter-coupling between two gold NPs (10 nm in diameter) on electric field enhancement. The spacing of NPs affects the position of the resonance peak, and with decreasing separation distance, resonance wavelength shifts toward a longer wavelength. However, upon using a structure with a larger separation distance between NPs than the NPs' dimensions, the resonance wavelength shift is negligible, as discussed elsewhere [39]. Furthermore, upon reducing the distance between two consecutive NPs, the electric field in a near-field regime is enhanced in the gap between NPs. Erik et al. also showed that induced electric field distribution between two consecutive NPs with a separation distance of 3 nm is stronger than in the case of 10 nm. Furthermore, in Erik et al.'s report, it was shown that with keeping NP's geometry and material fixed, a lower inter-particle distance is preferred to enhance the local field, which helps to increase sensor sensitivity [7,40].

Plasmon mode hybridization is another promising method that has been applied to promote the performance of LSPR sensors. Nanorings and nanoshells are the best nanostructures that represent plasmon hybridization effects [41]. In general, two different plasmonic modes are observed from hybridization phenomena: bonding and antibonding modes [42]. The bonding mode and anti-bonding mode, which are observed at a lower and higher frequency respectively, result from symmetrical and asymmetrical coupling of induced plasmonic waves and incident light in a nanostructure [42]. The geometry of a nanostructure plays a crucial role in tuning hybridized plasmonic modes. Tao et al. [43] showed that by using nanoring structures, greater sensitivity could be achieved than with nanodisc structures. Sensitivity improvement is attributed to strong

localization of the field in the ring's center. They also reported that the effect of ring-width variation is more significant for spectral properties than other geometrical parameters, such as ring size and ring-separation distance. As ring-width is increased, the plasmonic resonance peak narrows, which helps to enhance sensor performance, and specifically, the FOM of the sensor, due to the reduction of FWHM of the resonance peak. There are several other studies on nanostructures and the plasmonic hybridization effect, such as hollow nanoshells [25], nanorice shells [44], and nanotube arrays [45], and the use of nanoparticle arrays. Coupling plasmonic waves and incident waves demonstrates improvement in plasmonic resonance properties, and this could improve LSPR sensor performance [25].

1.5 Metal-Graphene Hybrid LSPR Sensor

Longer wavelength resonance, high resonance intensity, and sharper resonance band (minimum FWHM) are indications of enhanced sensitivity and FOM of the LSPR sensor. Therefore, engineering a plasmonic material by choosing a proper material type, tuning the geometry of the NP, or hybridizing it with another material in a way that improves one of the mentioned three plasmonic properties, could lead to improving plasmonic sensor performance. When considering the type of plasmonic material, silver is the best choice among other plasmonic materials in terms of sensor performance due to low optical loss in the visible range compared to other metals. However, in addition to an oxidation problem, Ag_2S forms on the Ag surface due to a reaction of carbonyl sulfide (OCS) and hydrogen sulfide (H_2S) with the Ag surface; this affects the plasmonic properties of the Ag nanostructure and results in an increase in material loss [46]. Furthermore, another source of loss arises from scattering due to an increase in the surface roughness of an Ag surface [47]. For this reason, gold is used more frequently in applications, even though gold suffers from higher optical loss in the visible range. Passivating and encapsulating the Ag surface to

prevent the formation of Ag_2S to maintain the excellent plasmonic properties of the Ag nanostructure has been explored [48]. However, the thickness of the passivation layer is high, up to a level that affects near-field interaction, which is very strong in the vicinity of the nanoparticle [48,49]. Therefore, a passivation material that prevents the formation of Ag_2S and is sufficiently thin, is desired to help solve the limitations of Ag in LSPR sensor applications. Leenaerts et al. studied the permeability to helium gas molecules of a graphene sheet with different levels of defects [49]. They found that the penetration of small atoms and molecules through a defective graphene sheet decreases exponentially with decreased size of sheet defects, and thus, a large defect size is preferred to increase graphene permeability to gas molecules. This result led to the use of graphene as a passivation layer for Ag NPs, in addition to the good plasmonic properties of graphene itself. Jason et al. [49] studied the effect of graphene passivation on the plasmonic properties of Ag NPs. They fabricated two sets of an Ag nanoantenna array, and one of these was passivated with graphene by transferring CVD-grown graphene onto the Ag nanoantenna array, as shown in Fig. 1.6 a, b. From the SEM image of the passivated and unpassivated arrays, it is clear how Ag_2S formed on the Ag surface affects the morphology of the Ag nanoantenna, which in turn affects plasmonic resonance over 30 days of optical reflection measurement. They observed that the resonance peak shifts 216 nm after 30 days of fabrication for unpassivated arrays, while a very large reduction in resonance shift of 15 nm occurs in the case of graphene-passivated Ag NPs; see Fig. 1.6 c, d. This provides greater stability of plasmonic properties of Ag NPs over the time it is passivated with graphene. To assess the effect of passivating Ag NPs with graphene on LSPR sensor performance, they measured the sensitivity of a passivated Ag NP array and a Au NP array, by monitoring resonance shift over change in the refractive index of the surrounding medium. Sensor sensitivity of the Au NP array was found to be 102 nm/RIU and jumped to 162 nm/RIU

for the graphene-passivated Ag NP array, which represents ~60% enhancement in sensor performance. This enhancement in performance of a Ag-based sensor after using graphene as a passivation material means that graphene is a promising material to solve the problem of utilizing a Ag-based LSPR sensor in different applications.

Another example showing the effectiveness of using graphene as a passivation material for an LSPR device is with passivating copper NPs, as reported by Li et al. [50]. Copper is a good plasmonic material; however, it comes as a third choice in plasmonic applications after silver and gold, due to its property of experiencing higher loss. The low cost of copper compared to gold and silver is advantageous. However, under an ambient environment, copper oxidizes rapidly, resulting in degradation in LSPR intensity, and thus, a reduction in sensing performance [51,52]. In order to overcome this issue, Cu surfaces must be protected from oxidation. As mentioned, protecting NPs with a thin layer of material helps to detect the near-field effect of plasmonic NPs after being excited with light. Li et al. transferred CVD graphene (1–3) layers on top of a Cu NP array fabricated on a quartz substrate, and absorption spectra were measured; see Figure 1.6e. They observed drastic field enhancement after adding graphene, and additional graphene layers enhanced the intensity of plasmonic resonance. This enhancement is due to strong field localization at the graphene/copper interface [53]. Furthermore, the resonance peak redshifted with increasing graphene layers, resulting from an increase in the refractive index of the Cu surrounding medium. Both improvements of plasmonic resonance intensity and redshift in the position are indicators of enhancement of performance of this device when used as an LSPR sensor. Therefore, in addition to protecting the Cu surface from oxidation, graphene, based on its plasmonic properties, also enhances the plasmonic properties of a sensor-based device.

Decorating a graphene film with metal NPs is another approach used to tune the plasmonic properties of an LSPR device. Xu et al. fabricated Ag NPs on top of a CVD graphene film [54]. They observed that as the Ag NP size increased from 50 nm–150 nm, plasmonic resonance redshifted from 446–495 nm. This redshift is due to an increase in the size of Ag NPs; it is known that as metal NP size increases, longer wavelength resonance is produced [31]. Furthermore, Xu et al. reported that as graphene film thickness increases, plasmonic resonance redshifts, which is another parameter used to tune plasmonic resonance to enhance performance [54,55].

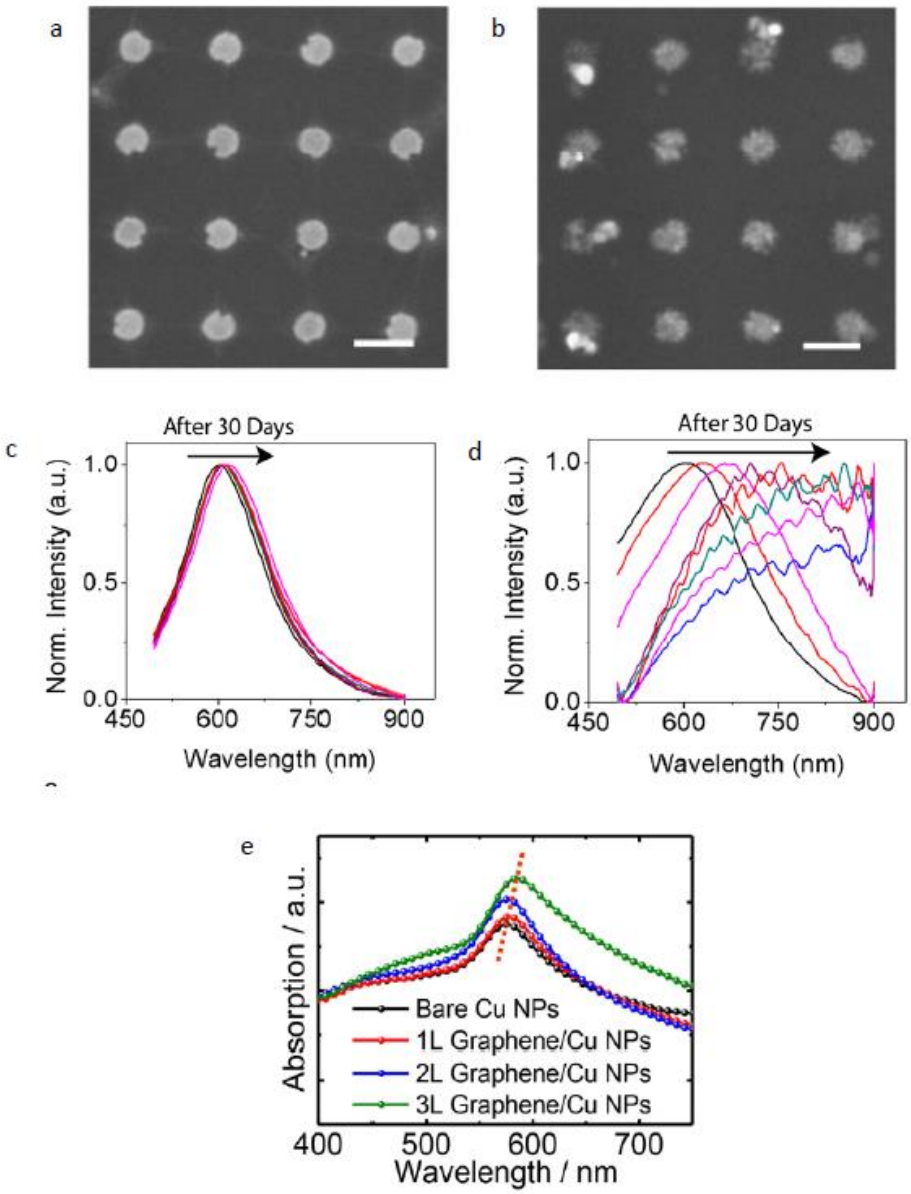

Figure 1.6: Scanning electron microscopy (SEM) images of a bare Ag nanoantenna (a) and a graphene-passivated Ag nanoantenna (b) after 30 days (scale bars are 200 nm), show how graphene protects Ag NPs from degradation. Bare Ag nanoantenna's (c) and graphene-passivated Ag NPs' (d) normalized (Norm.) reflection spectra over 30 days, show how passivation of Ag with graphene enhances the stability of Ag NPs [49]. (e) Optical absorption spectra for Cu NPs coated with a few graphene layers [50]

Another metal-graphene hybrid system that studied the effect of hybrid nanostructure on plasmonic resonance of the nanostructure is reported by Nan et al. [56]. They studied the effect of two different gold-graphene hybrid systems on the plasmonic resonance of a nanostructure. The first hybrid structure covered Au NPs with graphene (Fig. 1.7e), and the second "sandwiched" Au NPs between graphene layers (Fig. 1.7d). In both hybrid schemes, there is an obvious redshift for the resonance peak (Fig. 1.7 a, b), but there is no clear effect on redshifting as graphene layers increase (Fig. 1.7c). The redshift in plasmonic resonance is attributed to electron transfer from Au NPs to graphene. Consequently, modulating the electron transfer process could provide the capability to tune the plasmonic resonance, and thereby improve sensor performance by producing longer wavelength resonance.

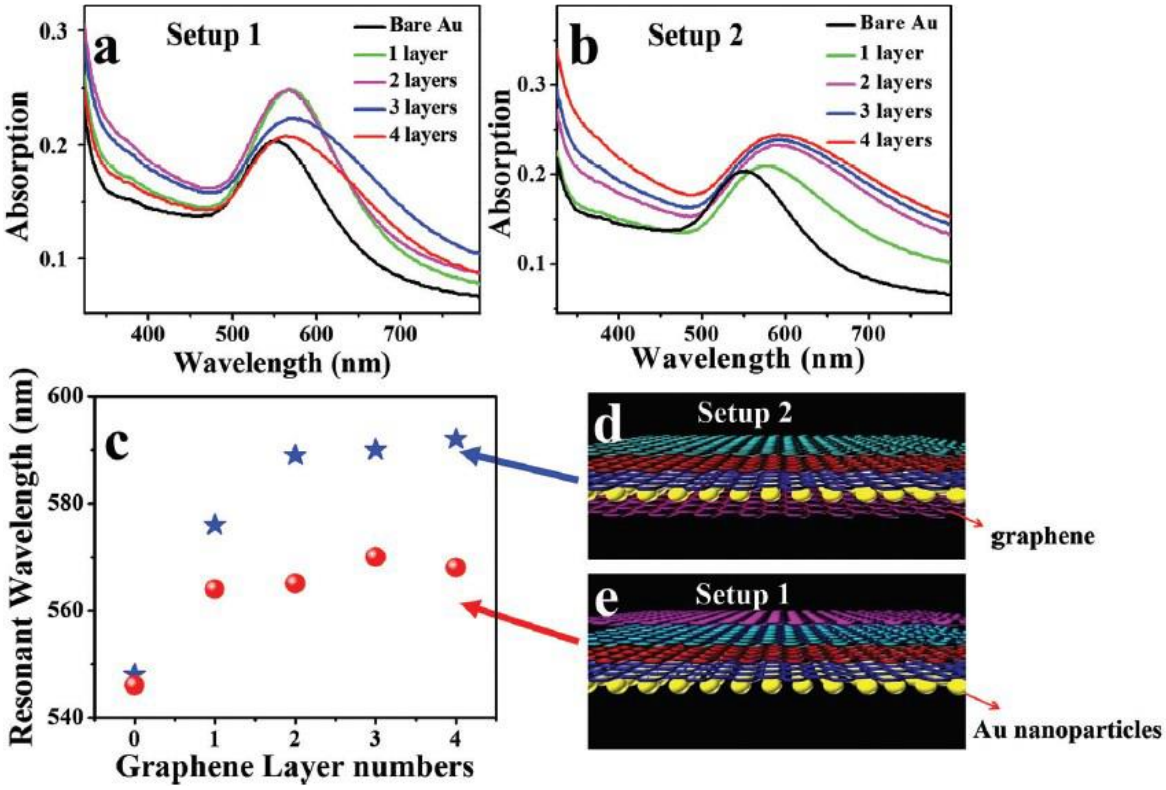

Figure 1.7: Absorption spectra of gold NPs coated (a) and encapsulated (b) by graphene layers. (c) Gold NP LSPR wavelengths for Setups 1 and 2. (d, e) The structures of setups used in (b, a) [56].

A plasmonic material that has high absorption in the visible region, such as metal, is preferred in plasmonic applications such as LSPR sensors. Graphene has very low absorption in the visible spectrum, and therefore enhancing its absorption will increase its potential to be used as a plasmonic material for an LSPR sensor in the visible region [57]. The hybridizing of graphene with metal enhances graphene absorption, as reported by Wu et al. [58]. They fabricated graphene nano-mesh samples and filled the empty part of the mesh with Au nanodiscs. An immense improvement was observed in absorption of the hybrid nanostructure compared to bare graphene. This improvement can help to enhance the LSPR-based sensor in two ways. First, enhancing absorption will increase the localized field around a nanostructure, and thus it will be more sensitive to a change in the surrounding refractive index. Secondly, an increase in the absorption band could lead to a decrease in the FWHM of the resonance band, thus enhancing the resulting FOM of the sensor. Integration of graphene with metal therefore increases the opportunity for a graphene-based device to be used in the visible region for various LSPR sensor applications.

The direct effect of hybridizing graphene with metal nanostructures on LSPR sensors has been studied by Maurer et al. [59]. They studied the effect of a graphene layer as a spacer between Au film and Au NPs. Graphene film was deposited on top of a Au film and subsequently the layers were decorated with a Au nano-disc array. They compared the optical absorption between AuNPs/Au film and AuNPs/graphene film/Au film nanostructures, observing ~ 23% enhancement in the extinction due to a localization field after adding the graphene spacer. This enhancement in the localization plasmon field led to ~33% enhancement in the sensitivity of the sensor. Maurer et al.'s work provides evidence of the effectiveness of the metal-graphene hybrid nanostructure on the performance of the LSPR sensor. Enhancing the absorption of the nanostructure reduces the scattering effect, and thus low FWHM of the resonance band is expected. Therefore, further

enhancement in the optical absorption could also yield a reduction in the FWHM and help to improve the FOM as well. However, LSPR phenomena are affected by a number of factors, including nanoparticle geometry and material type, and when two materials hybridize, the interaction between the nanostructure and the electromagnetic wave increases in complexity. Therefore, in the following section, computer-aided simulation modeling of an LSPR sensor is presented, which can help in designing a novel LSPR sensor and assessing its performance, with lower time and cost compared to experimental methods.

1.6 Simulation Modeling of LSPR Sensor

Simulation is considered to be one pillar of the scientific method, in addition to theory-building and experimentation [60]. When the theoretical study of a phenomenon becomes very complex or experimentation requires considerable time and expense, the role of simulation offers several advantages over theory-building and experimentation. Simulation can model a real system, with the help of computer technology and study of how a system works. Moreover, simulation is helpful in designing a physical system and examining its performance. A high level of controllability of input variables makes simulation an effective tool to improve system performance, helping to reduce time and cost of system development compared to experimentations. To attain additional insight about simulation modeling, the rest of this section discusses the simulation modeling performed in this research in greater detail.

As stated in previous sections, plasmonic properties of nanostructures depend on a number of factors, including nanostructure geometry and material type. This is an important point in terms of achieving a high level of tunability; however, exploring plasmonic properties and assessing sensing performance of the device experimentally demands much time and cost. Therefore, simulation plays an important role for researchers in engineering fields where it can help in the design and performance assessment, as well as save time and cost. Therefore, the first point to be considered in simulation is what the physics and mathematical models explain regarding the system or the device to be simulated. The LSPR sensor is based on interaction between light and metal nanoparticles, which can be well described using Maxwell's equations [6]. Therefore, Maxwell's equations will be the building block to carry out calculations for the required results. So far, there are a number of calculation methods used to solve Maxwell's equations; however, a finite difference time domain (FDTD) method has been widely applied to study the interaction of an electromagnetic wave and surrounding medium and objects [61]. The first step in simulation is defining the simulation region of this research, the substrate, hybrid gold-graphene nanostructure, and sensing medium as shown in Fig. 1.8.

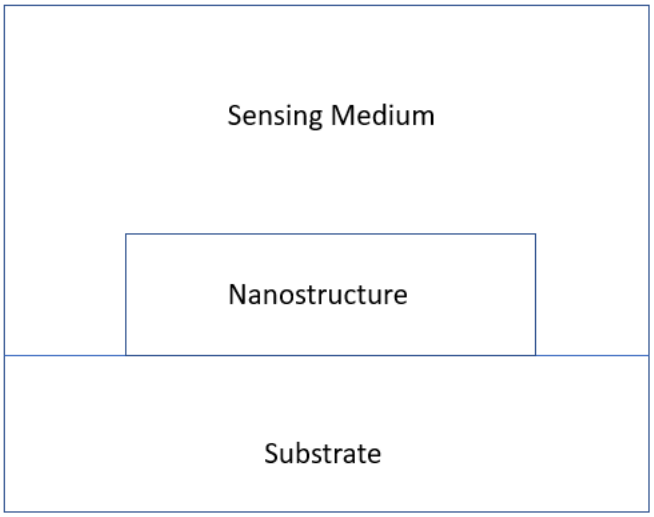

Figure 1.8: Schematic representation of the simulation region parts

Three-dimensional simulation is applied in this research, where the first hybrid nanostructure involved in this study is a spherical core-shell (Chp. 2) and it is required to perform the calculation in all three dimensions. In the 3D FDTD calculation, the simulation region is divided into many cubic grids as shown in Fig. 1.9 and each grid contains both electric (E) and magnetic (H) fields. This cubic grid is sometimes called a Yee lattice, referring to Chinese-American applied mathematician, Kane S. Yee, who established this method [62]. In this method, E and H fields are assumed to be interleaved around a cell, whose origin is located at i, j, k, see Fig. 1.9. In the center of each grid edge, electric field components are assigned and their vector directions are parallel to each edge; at the center of each grid face, magnetic field components are assigned, and their vector directions are perpendicular to each face. Following this meshing method, it is shown that electric and magnetic fields are separated in a half-spatial step.

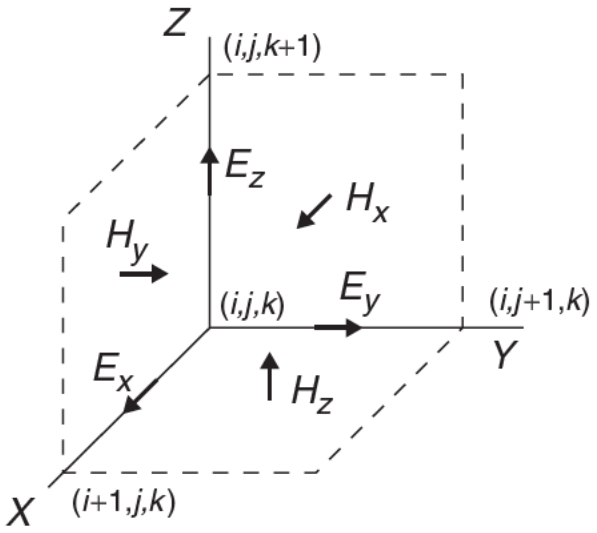

Figure 1.9: Yee basic unit cell [62]

The starting point in the FDTD calculation method involves the basic Maxwell's equations (Eqs. 1.10 - 1.12), shown below [63].

$$\frac{\partial D}{\partial t} = \frac{1}{\sqrt{\varepsilon_0 \mu_0}} \nabla \times \mathrm{H} \qquad 1.10$$

$$D(\omega) = \varepsilon_r(\omega).E(\omega) \qquad 1.11$$

$$\frac{\partial H}{\partial t} = -\frac{1}{\sqrt{\varepsilon_0 \mu_0}} \nabla \times \mathrm{E} \qquad 1.12$$

Where D is a displacement field, ε_0 & μ_0 are permittivity and permeability of the free space, and ε_r is the complex relative permittivity of the material.

In 3D simulation, and based on equations 1.10 -1.12, the x, y, & z components of electric and magnetic fields can be expressed as the following [63].

$$\frac{\partial D_x}{\partial t} = \frac{1}{\sqrt{\varepsilon_0 \mu_0}}\left(\frac{\partial H_z}{\partial y} - \frac{\partial H_y}{\partial z}\right) \quad 1.13$$

$$\frac{\partial D_y}{\partial t} = \frac{1}{\sqrt{\varepsilon_0 \mu_0}}\left(\frac{\partial H_x}{\partial z} - \frac{\partial H_z}{\partial x}\right) \quad 1.14$$

$$\frac{\partial D_z}{\partial t} = \frac{1}{\sqrt{\varepsilon_0 \mu_0}}\left(\frac{\partial H_y}{\partial x} - \frac{\partial H_x}{\partial y}\right) \quad 1.15$$

$$\frac{\partial H_x}{\partial t} = \frac{1}{\sqrt{\varepsilon_0 \mu_0}}\left(\frac{\partial E_y}{\partial z} - \frac{\partial E_z}{\partial y}\right) \quad 1.16$$

$$\frac{\partial H_y}{\partial t} = \frac{1}{\sqrt{\varepsilon_0 \mu_0}}\left(\frac{\partial E_z}{\partial x} - \frac{\partial E_x}{\partial z}\right) \quad 1.17$$

$$\frac{\partial H_z}{\partial t} = \frac{1}{\sqrt{\varepsilon_0 \mu_0}}\left(\frac{\partial E_x}{\partial y} - \frac{\partial E_y}{\partial x}\right) \quad 1.18$$

After producing the three-dimensional components of the electric and magnetic fields, the finite difference approximations are performed and then computer equations are written and solved. For example, as reported by Dennis M. Sullivan [63], using equations 1.15 & 1.18, the finite difference approximations can be written as in equations 1.19 & 1.20. Note that the superscript refers to the temporal locations in the time interval [t^n, t^{n+1}]. For example, n+1/2 refers to the half time point that is between t^n and t^{n+1}.

$$D_z^{n+\frac{1}{2}}\left(i,j,k+\frac{1}{2}\right) = D_z^{n-\frac{1}{2}}\left(i,j,k+\frac{1}{2}\right) + \frac{\Delta t}{\Delta x \cdot \sqrt{\varepsilon_0 \mu_0}}\left[H_y^n\left(i+\frac{1}{2},j,k+\frac{1}{2}\right) - H_y^n\left(i-\frac{1}{2},j,k+\frac{1}{2}\right) - H_x^n\left(i,j+\frac{1}{2},k+\frac{1}{2}\right) + H_x^n\left(i,j-\frac{1}{2},k+\frac{1}{2}\right)\right] \quad 1.19$$

$$H_z^{n+1}\left(i+\frac{1}{2},j+\frac{1}{2},k\right)=H_z^{n}\left(i+\frac{1}{2},j+\frac{1}{2},k\right)-\frac{\Delta t}{\Delta x\cdot\sqrt{\varepsilon_0\mu_0}}\left[E_y^{n+\frac{1}{2}}\left(i+1,j+\frac{1}{2},k\right)-\right.$$
$$\left.E_y^{n+\frac{1}{2}}\left(i,j+\frac{1}{2},k\right)-E_x^{n+\frac{1}{2}}\left(i+\frac{1}{2},j+1,k\right)+E_x^{n+\frac{1}{2}}\left(i+\frac{1}{2},j,k\right)\right] \qquad 1.20$$

Then, from the difference equations (eq. 1.19 & 1.20), the computer equations can be written as:

```
dx [i] [j] [k]  =  dx [i] [j] [k]
                        +  0.5 * (hz [i] [j] [k]  -   hz [i] [j-1] [k]
                              -    hy [i] [j] [k] +  hy [i] [j] [k-1])    ;
dy [i] [j] [k]  =  dy [i] [j] [k]
                        +  0.5 * (hx [i] [j] [k]   -   hx [i] [j] [k-1]
                              -    hz [i] [j] [k]  +  hz [i-1] [j] [k])    ;
dz [i] [j] [k]  =  dz [i] [j] [k]
                        +  0.5 * (hy [i] [j] [k]   -   hy [i-1] [j] [k]
                              -    hx [i] [j] [k]  +  hy [i] [j-1] [k])    ;
hx [i] [j] [k]  =  hx [i] [j] [k]
                        +  0.5 * (ey [i] [j] [k+1]   -   ey [i] [j] [k]
                              -    ez [i] [j+1] [k]  +  ez [i] [j] [k])    ;
hy [i] [j] [k]  =  hy [i] [j] [k]
                        +  0.5 * (ez [i+] [j] [k]   -   ez [i] [j] [k]
                              -    ex [i] [j] [k+1] + ex [i] [j] [k])     ;
hz [i] [j] [k]  =  hz [i] [j] [k]
                        +  0.5 * (ex [i+] [j+1] [k] -   ex [i] [j] [k]
                              -    ey [i+1] [j] [k] + ey [i] [j] [k])     ;
```

Note that d, h, and e in the above equations refer to displacement, magnetic, and electric fields, respectively.

Furthermore, calculations of the E and H fields are performed in a repeating manner: H field value is solved at a time point, and E field is solved at the next time point. In this way, the calculation runs cyclically until the fields in the entire simulation region are solved [61]. From Maxwell's equations, the optical constant (permittivity or refractive index) as a function of

wavelength for the material under study is required. Lumerical FDTD Solution is the software package used to carry out calculations in this research. Lumerical obtained experimental or analytical data is from the literature in the material library. Refractive index values obtained from the literature cannot be applied directly in the calculation, so Lumerical software generates an analytic material model automatically based on experimental data and will be used in the simulation. In addition, a fitting tool is available to enhance fitting of FDTD model data with experimental data obtained from the literature. In this research, gold and graphene are used, and their refractive index values as a function of wavelength are modeled and fitted with experimental data of gold [64] and analytical data of graphene [65], as shown in Fig. 1.10.

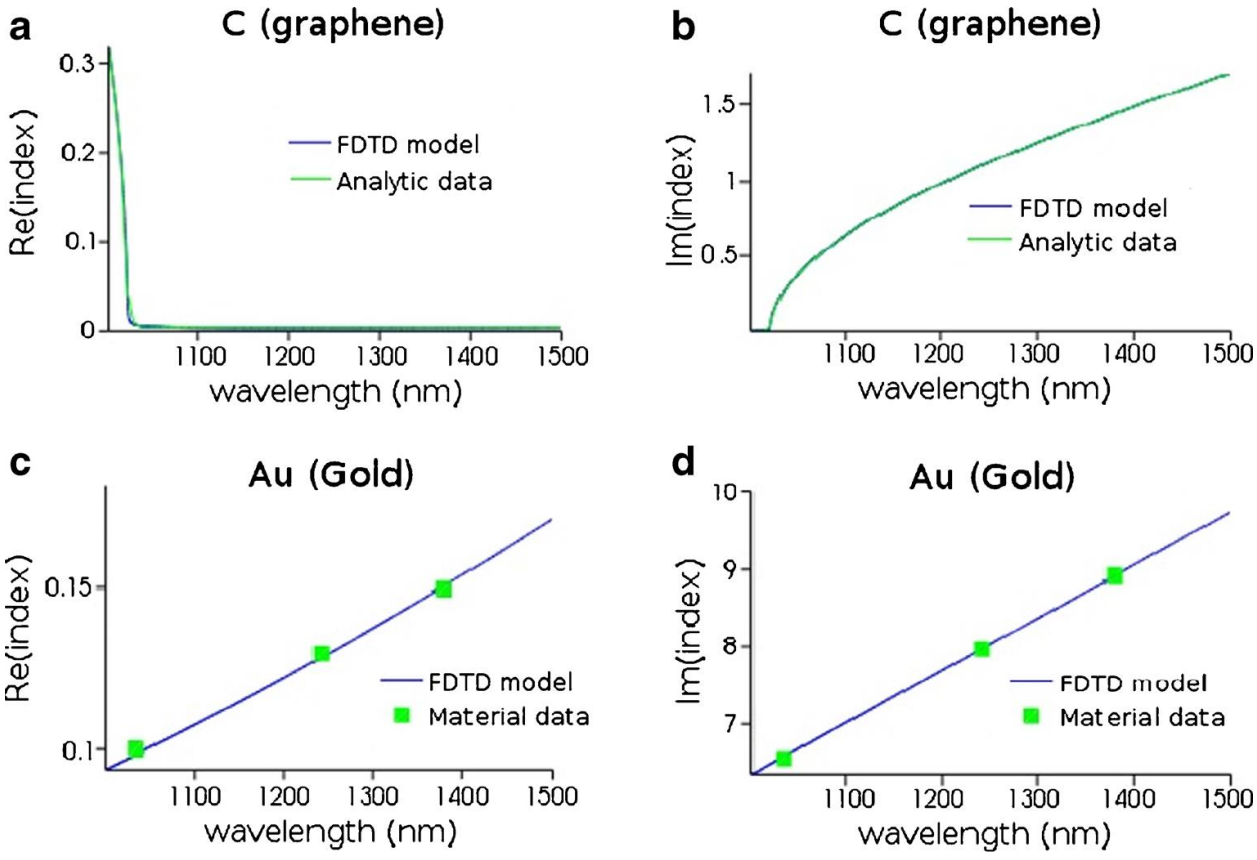

Figure 1.10: The real part and imaginary parts of (a–b) graphene refractive index and (c–d) gold refractive index obtained from the FDTD model and literature data as a function of wavelength in

the range of 1 to 1.5 μm. Experimental and analytical refractive indices (material data in the figure) were taken from [66] and [67] for gold and graphene, respectively.

Boundary conditions (BCs) play an important role in the simulation work to be defined for the simulation region, and in 3D simulation, BCs in all three directions must be specified. In this research, the hybrid nanoparticle is repeated as an array in the x and y directions, and boundary conditions insure periodicity is required. The periodic array of a nanostructures involves a plane of symmetry, and thus, using symmetric BCs is the proper choice [68]. As there are symmetric BCs, so there also are anti-symmetric BCs as shown in Fig. 1.11, indicating the electric and magnetic field components for different types of symmetry [68]. From this figure, it is clear that using two types of BCs (i.e. symmetric and anti-symmetric) is required to involve all possible components of electric and magnetic fields, and thus, symmetric and anti-symmetric BCs were used for x and y directions, respectively [68].

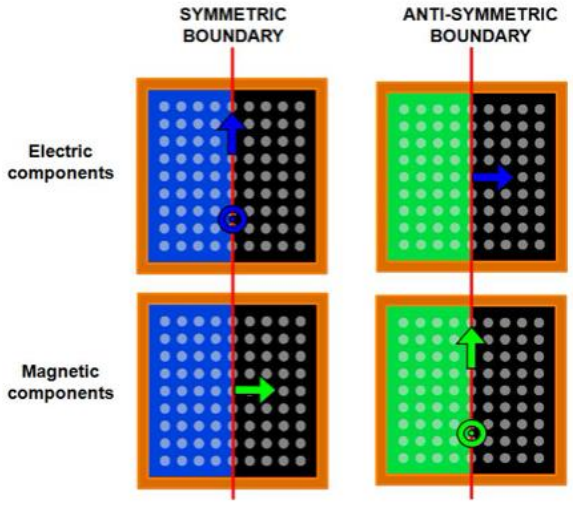

Figure 1.11: Electric and magnetic field components in the symmetric and anti-symmetric BCs

In the z-direction, a perfect matched layer (PML) boundary condition is applied. PML is an artificial layer introduced in 1994 by Berenger [69] and is capable of absorbing light waves (both propagated and evanescent) with minimal reflection [68,69]. It is used in simulation to avoid back reflection, which may affect the optical spectrum obtained for the nanostructure [68]. In the z-direction, the nanostructure is shined with a plane wave from the bottom, and a frequency domain monitor is placed at the top of the nanotecture. This monitor collects the data at frequency points, so optical spectrum (optical transmission, reflection, or absorption versus wavelength) can be obtained where the optical spectrum is required to study the plasmonic sensor sensitivity as explained previously in section 1.2. Finally, after defining the refractive index of the substrate (n = 1.45) and sensing medium (n = 1.333), a simulation can be run, and when completed, the optical spectrum (transmission) can be obtained through the frequency domain monitor. This, in brief, is how the simulation for the device (LSPR sensor in this research) is performed, starting with defining the mathematical equation and calculation method to running the simulation and obtaining the desired results using the computer software package (Lumerical FDTD Solution, in this research).

1.7 Research Problem and Contributions

Though the LSPR sensor has advantages over the PSPR sensor, the PSPR sensor has so far been used commercially in bio-sensing applications. The reason is the high and competitive sensing performance offered by the PSPR sensor, which is the main limitation of the LSPR sensor with respect to bio-sensing applications. The LSPR sensor performance reported so far in the literature has not been competitive enough to allow the LSPR sensor to be utilized in bio-sensing

applications commercially, and more research is necessary. Recently, hybrid graphene with metal nanostructure has provided some improvement to the sensing performance of the LSPR sensor, which motivates this research. Therefore, this research is conducted to design and engineer various novel gold-graphene hybrid nanostructures numerically, using a finite difference time domain (FDTD) method, aimed at competitive-sensing performance to promote the potential of utilizing the LSPR sensor in bio-sensing applications, by utilizing the good plasmonic properties and bio-compatibility of graphene. Another objective is to conduct an optical near-field characterization experiment to study light-NP interaction to show how to use excited localized plasmons in plasmonic sensing applications.

This dissertation includes a number of contributions as summarized below*:*

1- Study the effect of wrapping spherical gold NPs with a multilayer graphene shell on optical absorption of the gold NPs array nanostructure, followed by optimizing plasmon resonance width (reduce FWHM), considering periodicity (periodic NP to NP distance), gold NP size, and graphene shell thickness parameters. Following this, sensing simulation of the gold-graphene core-shell hybrid NP array has been performed and sensing performance assessed by evaluating the sensitivity and FOM of the sensor. The work was numerically performed using the finite difference time domain (FDTD) method.

2- Effects of imbedding the medium between gold NP with multilayer graphene sheets on the optical absorption of a gold NP array and then on the sensing performance of a gold-graphene hybrid nanostructure have been studied and analyzed numerically using the FDTD method. Gold NP size to separation ratio and gold NP shape (disk, cube, and prism) are the two optimization parameters included in this study. Moreover, during a sensing

simulation, the refractive index of the nanostructure's surrounding medium was changed by a very low value (~ 0.001) to ensure a low detection limit.

3- A gold-graphene hybrid nanostructure with more controlled and fewer fabrication steps is designed by direct deposition of a graphene film on top of a Au NP array. After study of the effect of graphene thickness on optical absorption of the hybrid nanostructure, a sensing simulation was conducted for the gold-graphene hybrid nanostructure, and its sensing performance was assessed numerically using the finite difference time domain (FDTD) method. In this hybrid nanostructure, some graphene film is inserted between gold NPs and the rest is placed on top of gold NPs.

4- A hybrid gold NP array with graphene flakes of different shapes and sizes is a new and simple hybrid scheme that is developed in this research, and its contribution to enhancing LSPR sensor performance is studied. A new and simple gold-graphene hybrid scheme is proposed and its plasmonic sensing performance is numerically evaluated using the finite difference time-domain (FDTD) method. The proposed sensor can be developed by growing a Au nano-disk (ND) array on a quartz substrate and then spin-coating graphene flakes of different sizes and shapes randomly on top of and between the Au NDs.

5- Scanning near-field optical microscopy (SNOM) technique is applied to study light-gold NP interaction and show how this interaction can be utilized for plasmonic sensor applications. Near-field study is essential to characterize the nanostructure due to localization of the plasmonic field in the proximity of the nanostructure upon excitation,

which is difficult to perform using a regular optical microscope. A gold NP array has been fabricated on top of a quartz substrate using two fabrication steps: gold film deposition and then milling using focused ion beam (FIB) technology.

1.8 Thesis Overview

In this dissertation, Chapters 2 – 5 present numerical work (design and analysis) for four different hybrid nanostructures and their sensing performance assessment through application of the FDTD method using Lumerical FDTD solutions. Then, Chapter 6 includes optical near-field characterization of a fabricated Au NPs array, followed by Chapter 7 in which a research conclusion and summary of accomplished and future works are given.

Chapter 2 Gold-Graphene Core-Shell Hybrid Nanostructure for Localized Surface Plasmonic Resonance Sensors[1]

In this chapter, a 2D array of gold-graphene spherical core-shell nanostructure on a quartz substrate was introduced as a liquid sensor with FOM and sensitivity as large as 102.6 and 350 nm/RIU, respectively. The results show a significant improvement in the FOM, compared to previous works and common surface plasmon resonance refractive index sensors.

[1] This is an Accepted Manuscript of an article published by Alharbi, R., Irannejad, M., & Yavuz, M. in Plasmonics on 29 June 2016, available online https://link.springer.com/article/10.1007%2Fs11468-016-0325-z [Article DOI : 10.1007/s11468-016-0325-z]. "Gold-Graphene Core-Shell Nanostructure Surface Plasmon Sensors"

2.1 Introduction

Hybridizing gold with graphene is presently a promising way to overcome the issue of poor sensing performance of LSPR sensors. It has been reported that the gold-graphene core-shell hybrid nanoparticle enhances the plasmonic properties of gold nanoparticles. For example, encapsulating Au-SiO_2 core-shell nanoparticles with a graphene oxide (GO) layer was reported by Sreejith and coworkers [70]. They observed an enhancement of > 200% in the absorption of Au-SiO_2 core-shell plasmonic resonance (λ = 532 nm) after GO coating. Using finite difference time domain (FDTD) analysis they found through electric field distribution that enhancement was attributed to a combined absorption by Au and GO components. Absorption enhancement in the vicinity of plasmonic hybrid NP is a preferred method for improving LSPR sensing performance, where it is related to stronger resonance [6], and hybrid graphene with gold showed good tunability of plasmonic properties of Au NPs through enhancing absorption at the same resonance wavelength. Furthermore, Li and Zhang explain that the plasmonic modes resulted from plasmonic coupling in the core-shell dimers. As seen in Fig. 2.1, two basic plasmon modes resulted where the polarizability of the core and the shell component determine the type of resonance mode. In this structure, the coupling between the surface plasmon modes of the core and shell structures can be explained by a hybridization theory [71] in which plasmon resonances resulted from the interaction of the sphere and cavity plasmons, producing bonding (symmetric) and antibonding (antisymmetric) modes. The bonding mode offers stronger plasmon absorption than the antibonding mode, which can be used for improving the performance of LSPR sensors. Therefore, engineering the core-shell hybrid nanostructure using metal-graphene hybrid NP can help to overcome the LSPR sensor performance issue as addressed in this study.

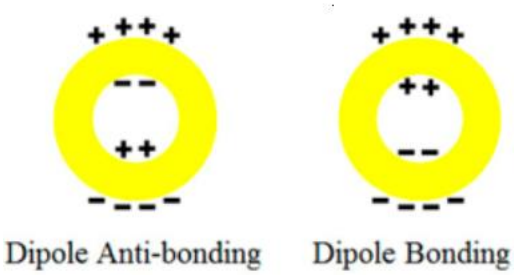

Figure 2.1: Dipole anti-bonding and dipole bonding plasmon modes of the core-shell NP [71]

In this work, a 2D array of gold-graphene spherical core-shell nanostructure on a quartz substrate was introduced as a liquid sensor, and the effects of using different parameters such as periodicity, diameter, and thickness of the Au-graphene hybrid nanostructure on the sensitivity and FOM of an LSPR sensor are studied. A series of periodic arrays of the Au-graphene spherical core-shell nanostructure on a quartz substrate were studied numerically, as a local refractive index sensor for liquids. The refractive index variation is considered to be in the range of 1.333 to 1.373, and the sensitivity and FOM of the designed structure are calculated using the FDTD method. Choosing a suitable wavelength range is one of the important parameters in designing the nano-sensors that are used in in vivo measurements [72]. To detect a biomarker of a cancer cell such as breast cancer, blood serum is used to detect the concentration of the biomarker. Due to the transmissivity of blood in the NIR region, the study of the proposed nano-biosensor was performed in the NIR region [73]. Illustration of the research methodology is followed by discussion of obtained results, fabrication possibility of this plasmonic sensor, and conclusion.

2.2 Methodology

In this work, FDTD method was employed to calculate the extinction spectra of gold-graphene (Au-G) hybrid nanostructure arrays placed on top of a silica substrate, as schematically shown in Fig. 2.2a. The refractive indices of glass substrate and superstrate (i.e., target materials for sensing application), were 1.45 and n, respectively, where n is the refractive index of the target liquids.

The numerical analysis was carried out using the FDTD commercial software package (Lumerical FDTD Solutions). The Au-G hybrid nanostructure, plane wave source, and transmission were co-planar with the boundary conditions that made them infinite in the x- and y directions. Herein, an unpolarized plane electromagnetic wave in the wavelength range of 1 to 1.5 μm, with an electric field amplitude of 1 V/m, which propagates in the z-axis (as labeled by arrows in Fig. 2.2), was used as an incident light source.

Anti-symmetric and symmetric boundary conditions were used in the x- and y-directions, respectively. The perfect matching layer (PML) was chosen in the z-direction to study the transmission properties of the electromagnetic field at normal incidence. As reported [68], the rule of thumb in meshing the nanostructure involves dividing the object under study into ~ 10 units. There may be more than 10 units but this will result in a longer simulation run time. The calculation grid resolution (i.e., mesh cell size) was 5 nm (point-to-point distance) in the x- and y-directions. In the z-direction, 1 nm mesh cell size is used in the simulation cell. A combination of grading mesh and conformal meshing methods, which are offered by the Lumerical FDTD package, were used to calculate the electromagnetic field at the rounded region of the Au-G hybrid nanostructures [68]. The calculation time (i.e. time required for the optical signal to pass the simulation region completely [68]) was set as 3000 fs, and the extinction spectrum was calculated using an x-y monitor at 150 nm away from the Au-G /superstrate (liquid) interface. The plane

wave source was placed 150 nm below the structure as shown in Fig. 2.2 where as reported [68], there is no apparent or significant effect of the source distance on the results, and to reduce the simulation run time, a small distance (150 nm) is used, which is also close to what is employed in the literature [74]. The background refractive index was chosen as 1 (air), and water (n = 1.333) was used as a reference liquid in the sensitivity and FOM measurements.

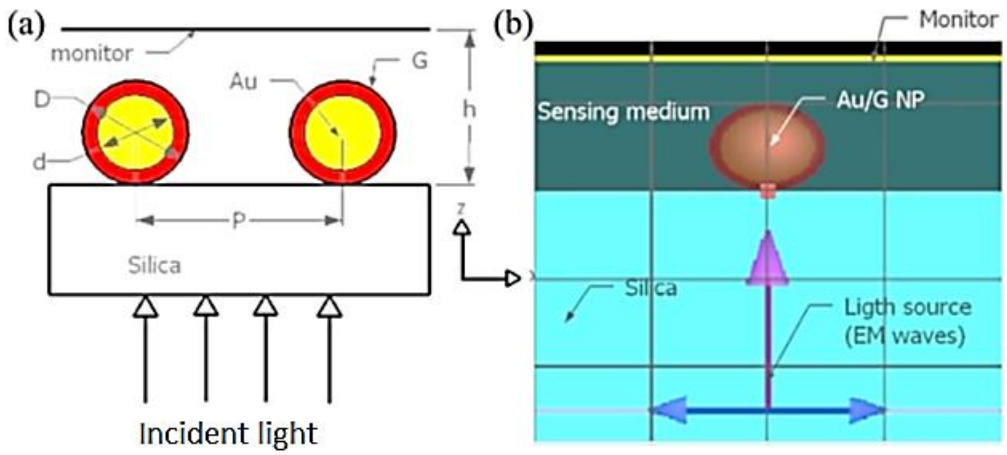

Figure 2.2 2D (a) is a schematic diagram and (b) is a numerical layout of the designed sensor used in this study. D is the Au-G hybrid nanostructure diameter, d is the Au nanoparticle diameter, t is the graphene thickness (t = D/2 − d/2), and P is the structural periodicity.

Herein, a series of Au-G hybrid nanostructures were studied with different structural periodicities (P), Au diameter (d), and graphene thickness (t = D/2 − d/2) while the total size of the hybrid nanostructure (D) was constant. The optimum parameters were obtained for a structure with the highest extinction (1 − T) intensity and narrowest resonance peak. The sensitivity and FOM of the Au-G hybrid nanostructure with optimum parameters were calculated by changing the target liquid refractive indices in the range of 1.333 to 1.373.

2.3 Results and Discussion

2.3.1 Effects of Graphene Contribution on the Au Nanostructure Extinction Spectrum

The effects of graphene contribution on the surface plasmon resonance properties of the Au NP periodic array in the NIR region were investigated by calculating the extinction (1 − T) spectrum of the Au-G hybrid nanostructures and comparing it with that of the Au nanoparticle periodic arrays as shown in Fig. 2.3. The diameter of the Au nanoparticles was fixed at 40 nm, while in the second structure (i.e., Au-G hybrid nanostructure), the gold diameter and the graphene shell thickness (t; t = D/2 − d/2) were chosen as 34 nm and 3 nm, respectively, to maintain the whole nanoparticle diameter at 40 nm (D in Fig. 2.2). The structural periodicity for both nanostructures was fixed at 300 nm. The nanostructure is repeated in a square array in the x & y directions.

From Fig. 2.3a and Fig. 2.3b, it is evident that by introducing a 3-nm-thick graphene shell around the Au nanoparticle, a strong and sharp plasmonic resonance mode at a wavelength of 1363 nm was recorded in hybrid configuration (Fig. 2.3a), which was not observed in the case of Au NP alone (Fig. 2.3b). From Fig. 2.3e, the electric field profile of the Au-G hybrid NP showed that this resonance (λ = 1363 nm) is attributed to a bonding resonance mode resulting from coupling of plasmons of gold and graphene components, as explained by Li and Zhang [71], which shows strong absorption and field localization at the Au-G interface, and in turn, low scattering within the surrounding medium, which resulted in low FWHM (FWHM = 7.8 nm). Furthermore, enhancement in the localized field has been shown in the electric field profile recorded for both Au NP and Au-G hybrid NP as shown in Fig. 2.3 c & d, respectively. The maximum electric field value recorded for Au NP was ~ 2.5 V/m, which was enhanced to > 60 V/m after coating the Au

NP with a graphene shell. In addition, by comparing Fig. 2.3 d with Fig. 2.3e, it is evident that the bonding mode results in a higher maximum electric field (>60 V/m) compared with the antibonding mode (~ 8 V/m), which is expected due to stronger absorption as reported [71]. Other resonance modes (λ = 1271 nm and λ =1409 nm) result in a weaker resonance mode, which can be attributed to anti-bonding modes as reported [71]. Furthermore, strong enhancement in the absorption (~55 folds) after coating the Au NP with a graphene shell was observed, which can be attributed to a combined absorption of gold and graphene as reported experimentally by Sreejith et al. [70]. Enhancement in the localized electric field and sharpening the resonance peak helps to improve local sensitivity of the refractive index changes, and enhances the performance of the LSPR-based sensor accordingly.

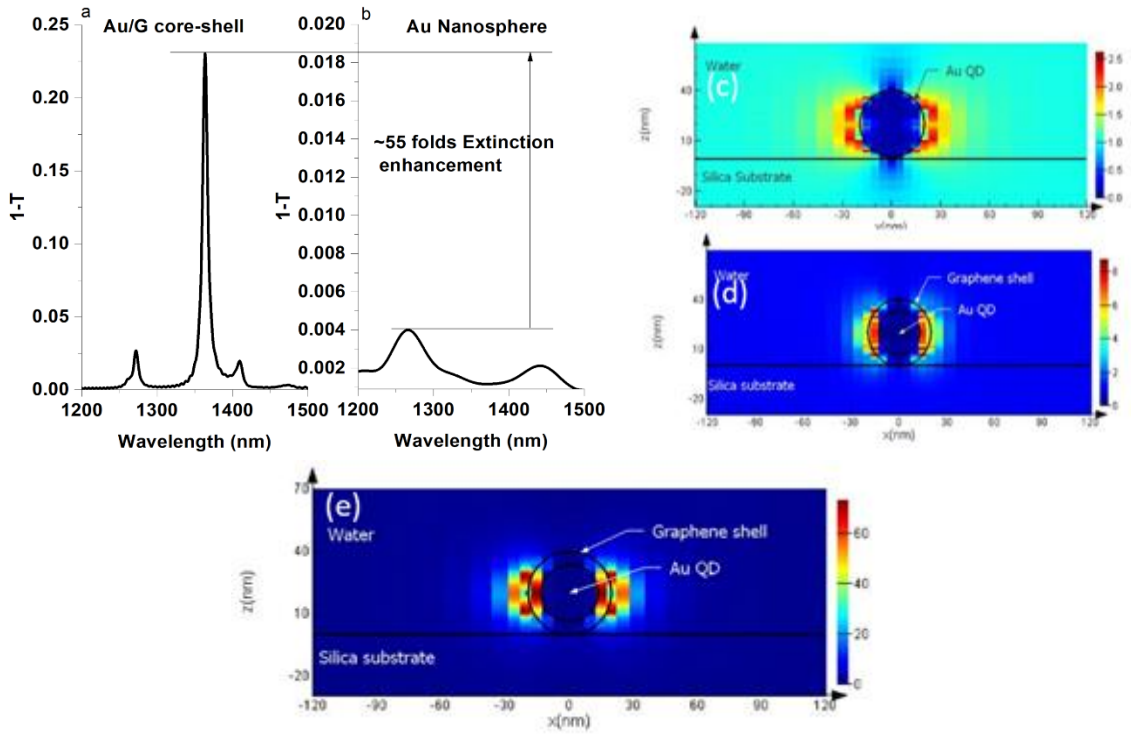

Figure 2.3 (a) Extinction spectrum of the Au-G hybrid nanostructure with Au diameter of 34 nm and graphene shell thickness of 3 nm and (b) Au nanoparticle with a diameter of 40 nm. In both structures, the structural periodicity was fixed at 300 nm. (c, d, & e) Electric field profile of (c) Au nanoparticles at λ = 1265 nm, (d) Au-G hybrid nanostructure at λ = 1271 nm (antibonding mode) and (e) Au-G hybrid nanostructure is at λ = 1363 nm (bonding mode).

2.3.2 Effects of Varying Structural Periodicity

To determine the effects of varying periodicity on the surface plasmon resonance properties of the proposed structure, a series of encapsulated Au spheres of a diameter of 34 nm with 3 nm thick graphene shell were studied numerically. The structural periodicity along the x-axis and y-axis was changed in the range of 300 to 500 nm with an increment step of 50 nm.

Fig. 2.4a shows the effects of varying periodicity on the extinction spectrum of the Au-G hybrid nanostructure. Intensity of the resonance peaks was gradually increased while the calculated FWHM of the resonance peak at a wavelength of 1363 nm was decreased from 8.1 to 7.8 nm, with decreasing the structural periodicity from 500 to 300 nm as presented in Fig. 2.4c. Increases in the resonance intensity at a resonance wavelength of 1363 nm can be attributed to the suppression of the scattered surface plasmon modes from the Au-G hybrid nanostructure at smaller structural periodicity; hence, the enhancement of the electric field amplitude localization at resonance, which resulted in absorption enhancement of the Au-G hybrid NP that agrees with the research work reported by Li and Zhang [71]. They found that as the hybrid core-shell structures of TiO2-Ag approach each other, coupling effects of the plasmon modes become notable due to stronger interactions of the charges on the surface of the metal. Therefore, here it can be said that upon decreasing periodicity, the surface charge interaction of the graphene shell increases, which results in enhanced absorption at the Au-G interface and thus the intensity of the plasmonic resonance obtained in the spectrum is increased. A periodicity of 300 nm is not the optimum value; however, it is practically applied as reported by Maurer et al. where they fabricated the Au NPs array with 300 nm periodicity on top of a quartz substrate [59]. Fabricating smaller than 300 nm may improve the resonance intensity as reported by Erik Martinsson [75], where they found that the localized field between two NPs was enhanced as the spacing decreased down to 3 nm. However, the complexity in the fabrication process is the drawback with smaller nanostructure size as reported [76].

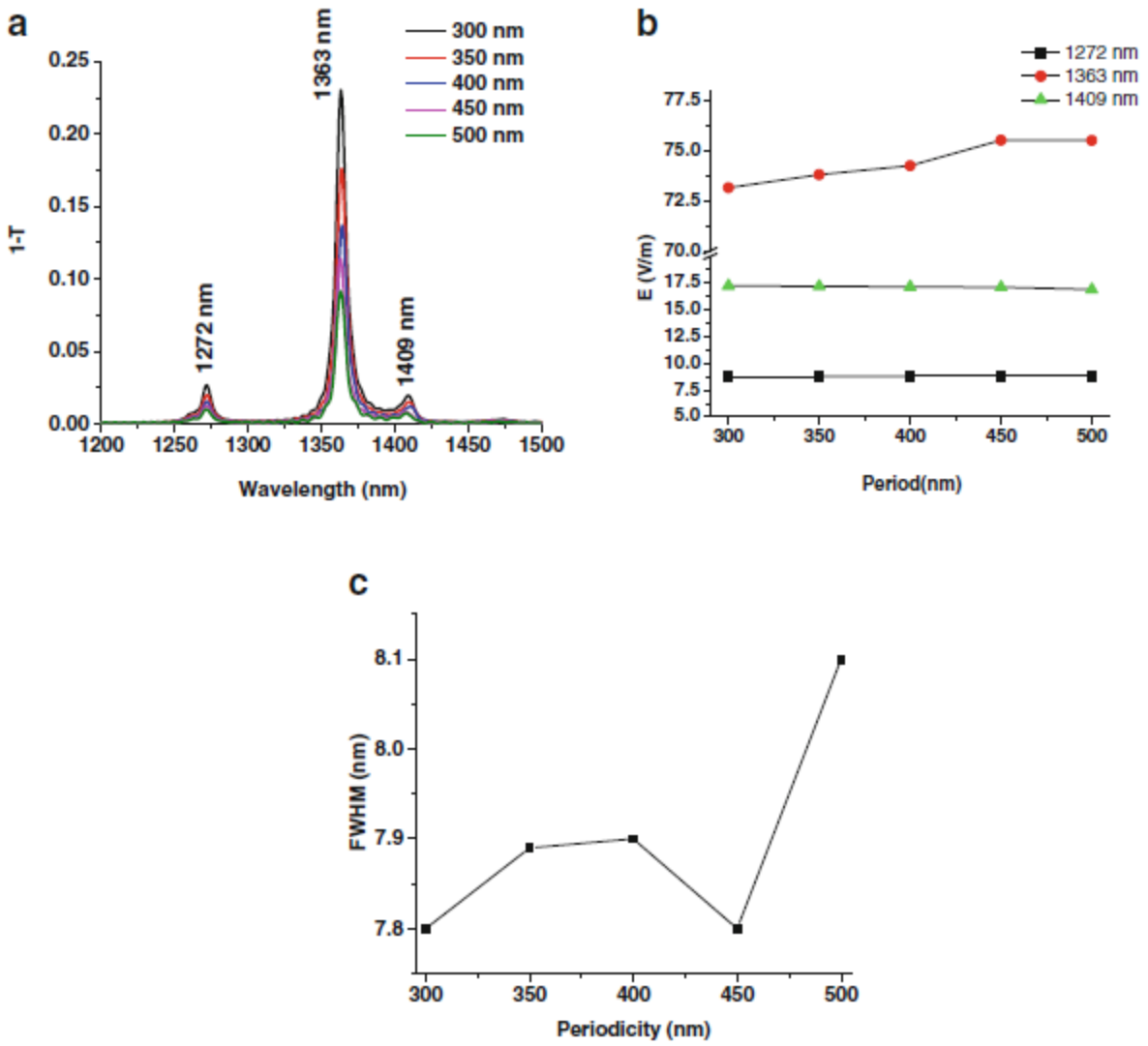

Figure 2.4 (a) Extinction spectrum of the Au-G nanostructure array at different periodicities. (b) Electric field value as a function of structural periodicity at resonances at wavelengths of 1272, 1363, and 1409 nm. (c) The FWHM of the resonance wavelength of 1363 nm as a function of structural periodicity. The Au nanoparticle diameter and graphene shell thickness were fixed at 34 and 3 nm, respectively.

The maximum electric field amplitude of the Au-G hybrid nanostructure at different resonance wavelengths of 1271, 1363, and 1409 nm, as a function of structural periodicity, is

shown in Fig. 2.4b. As can be seen from this figure, there are no significant changes in the recorded electric field amplitudes of each resonance wavelength at different periodicities, except at the bonding mode resonance, which is clearly observed as absorption enhancement. Due to a narrower band width and higher intensity compared to configurations with other structural periodicities, a structural periodicity of 300 nm was chosen for the further investigations carried out to study the effects of varying Au diameter and graphene thickness on the surface plasmon resonance properties of a refractive index sensor, which are discussed in the following sections.

2.3.3 Effects of Varying Au Nanoparticle Size and Graphene Shell Thickness

The effects of varying both the Au nanoparticle diameter and graphene shell thickness on the surface plasmon properties of the hybrid nanostructure at a fixed structural periodicity of 300 nm and hybrid nanoparticle (i.e., Au diameter and graphene shell thickness) sizes of 40, 50, and 60 nm were studied. For each hybrid NP size, e.g. 40 nm, graphene thicknesses in the range of 3 to 7 nm were studied and their extinction spectra are shown in Fig. 2.5a–c.

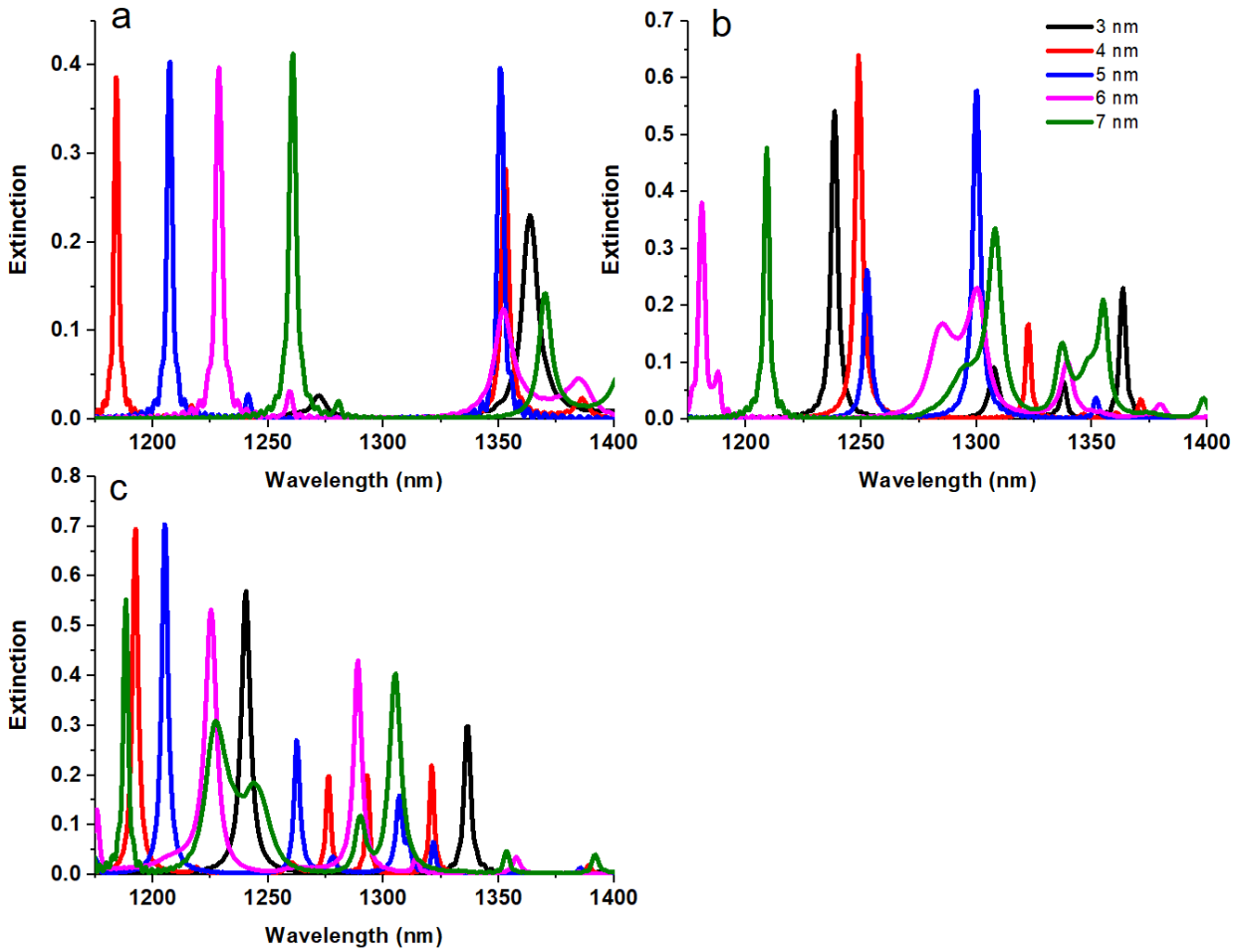

Figure 2.5 Extinction spectra of the Au-G hybrid nanostructure with a Au-G hybrid nanostructure diameter of (a) 40 nm,(b) 50 nm, and (c) 60 nm and different graphene thickness in the range of 3 to 7 nm. The structural periodicity was fixed at 300 nm.

The resonance wavelength, extinction, and FWHM of the bonding mode (i.e., resonance with maximum intensity) of the Au-G hybrid nanostructure with different Au diameters, different graphene thicknesses, and using water (n = 1.333) as a superstrate medium are summarized in Table 2.1 and compared in Fig. 2.6a–c. As demonstrated by this table and Fig. 2.6a–c, both Au diameter and graphene thickness significantly affected the resonance position and its intensity.

Table 2.1: Resonance wavelength, extinction intensity, and FWHM of the bonding mode in the Au G hybrid nanostructure with different Au diameter and graphene thicknesses.

Total hybrid size (nm)	Graphene thickness (nm)	Resonance position (nm)	Extinction intensity	FWHM (nm)
40	3	1363	0.23	8.47
	4	1184	0.39	2.3
	5	1351	0.40	3.55
	6	1228	0.39	3.5
	7	1261	0.41	3.73
50	3	1239	0.54	3.13
	4	1248	0.64	2.1
	5	1300	0.58	3.63
	6	1180	0.38	3.13
	7	1209	0.48	2.61
60	3	1240	0.57	4.24
	4	1129	0.7	2.89
	5	1205	0.7	2.89
	6	1225	0.53	6
	7	1188	0.55	2.5

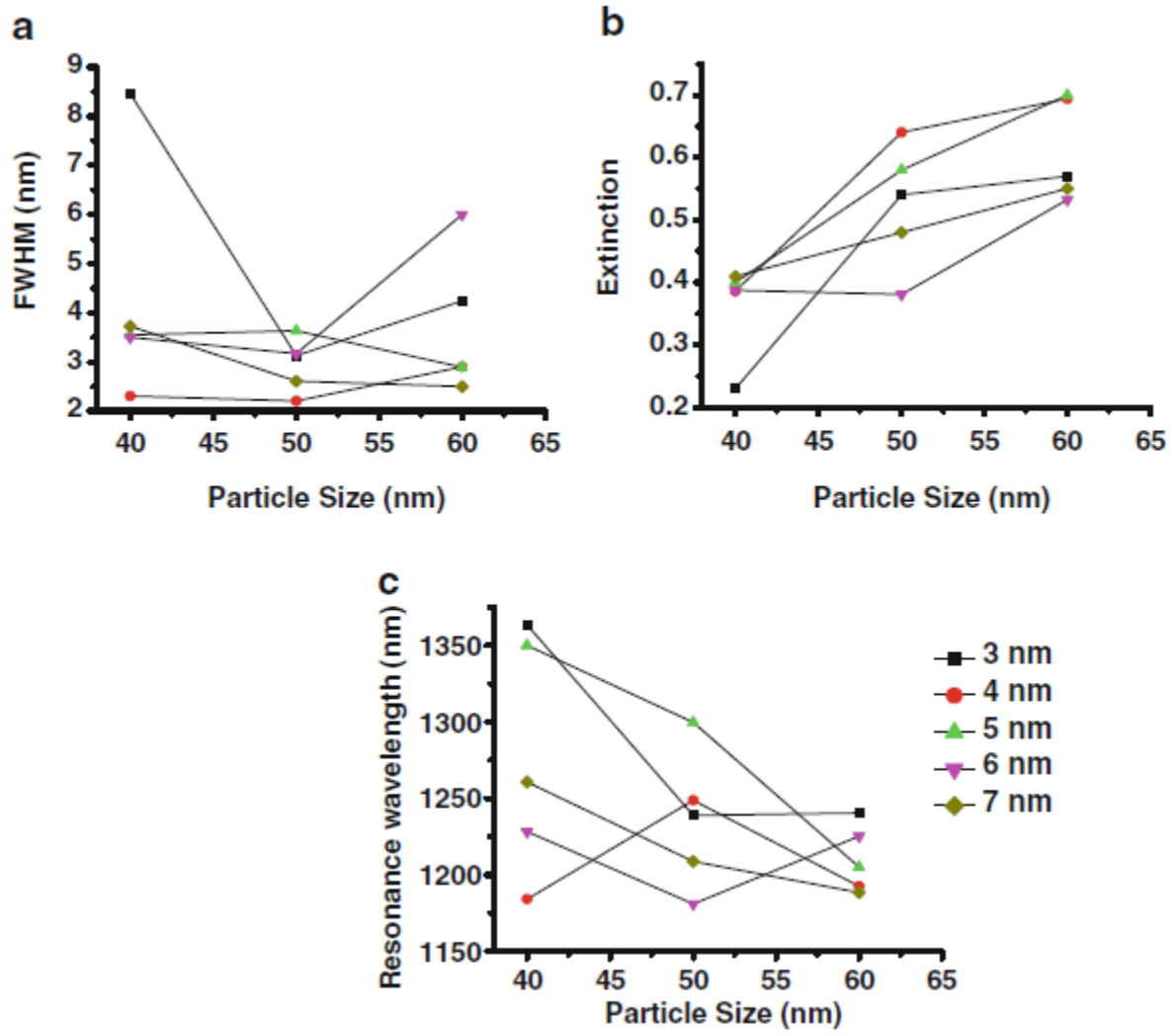

Figure 2.6 (a) FWHM, (b) extinction intensity, and (c) the resonance wavelength of the bonding resonance mode of the Au-G hybrid nanostructure as a function of hybrid nanostructure diameter at different graphene thicknesses.

As can be seen from Fig. 2.6a, the resonance wavelengths of encapsulated hybrid nanostructures with different graphene shell thicknesses were shifted toward a smaller wavelength by increasing the Au diameter while extinction intensity was increased. Increasing the electron density in the hybrid nanostructure could be a reason for this blueshift in the resonance

wavelengths. Increasing Au nanoparticle diameters results in higher electron density in the periodic array. Electron density and resonance wavelength can be related by [77]

$$\lambda_b = \frac{c\sqrt{m_e \varepsilon_0}}{n_e e^2} \qquad 2.1$$

where n_e is the electron density, e is the electric charge, m_e is the effective mass of the electron, ε_0 is the permittivity of free space, and c is the speed of light. As evident from this equation, by increasing electron density the resonance wavelength decreases, which results in a blueshift in the resonance wavelength of the hybrid nanostructure.

The resonance peak intensity and its FWHM strongly depend on the nanoparticle sizes [78]. Thus, it was expected that both FWHM and the intensity of the resonance peaks were affected by increasing the Au-G hybrid nanoparticle diameters from 40 to 60 nm, as confirmed in Fig. 2.6a, b. As can be seen from Fig. 2.6b, the extinction intensity was recorded as ~ 0.7 in the hybrid nanostructures with a diameter of 60 nm and graphene thicknesses of 4 and 5 nm, respectively, which represents the maximum extinction recorded. Moreover, as shown in Fig. 2.6a, the resonance mode at maximum extinction intensity offers a narrow width in the hybrid nanostructure with larger diameter in some graphene shell thicknesses such as 4, 5, & 7 nm, which indicates that increasing graphene shell thickness could improve the FWHM. The FWHM of the hybrid nanostructure with nanoparticle size of 60 nm and graphene thicknesses of 5 and 7 nm was calculated as 2.9 and 2.5 nm, respectively, and the minimum FWHM observed here is 2.1 nm for Au-G NP with size of 50 nm and graphene shell of 4 nm.

Although a hybrid NP with a size of 50 nm results in the lowest FWHM, a hybrid NP with size of 60 nm and a graphene shell of 7 nm has been chosen for sensitivity analysis due to the highest extinction value (~ 0.7) being recorded, and its FWHM (FWHM = 2.5 nm) is very close to the FWHM of the hybrid NP with size 50 nm (FHHM = 2.1 nm).

2.3.4 Measurement Sensitivity as a Liquid Sensor

Periodic Au-G hybrid nanostructure arrays with structural parameters: nanoparticle size (D) of 60 nm, graphene thickness of 7 nm as encapsulating layer, and structural period of 300 nm, were employed as a refractive index sensor. Water, with a refractive index of 1.333, was chosen as the reference liquid, and target liquid refractive indices were in the range of 1.333 to 1.373. The sensing performance of the proposed periodic nanostructure was investigated by using water as a reference liquid, and two different properties of resonance peaks were used: resonance wavelength shift ($\Delta\lambda$) and resonance intensity shift (ΔI) at different refractive indices of the target liquids.

Fig. 2.7 shows the recorded extinction spectra of the hybrid nanostructure with optimum structural parameters at different refractive indices in the range of 1.333 to 1.373. As can be seen from this figure, there are two major resonance wavelengths, which are labeled A (λ = 1188 nm) and B (λ = 1305 nm). These two resonance modes were used for wavelength sensitivity (S_λ) and intensity sensitivity (S_I) calculations.

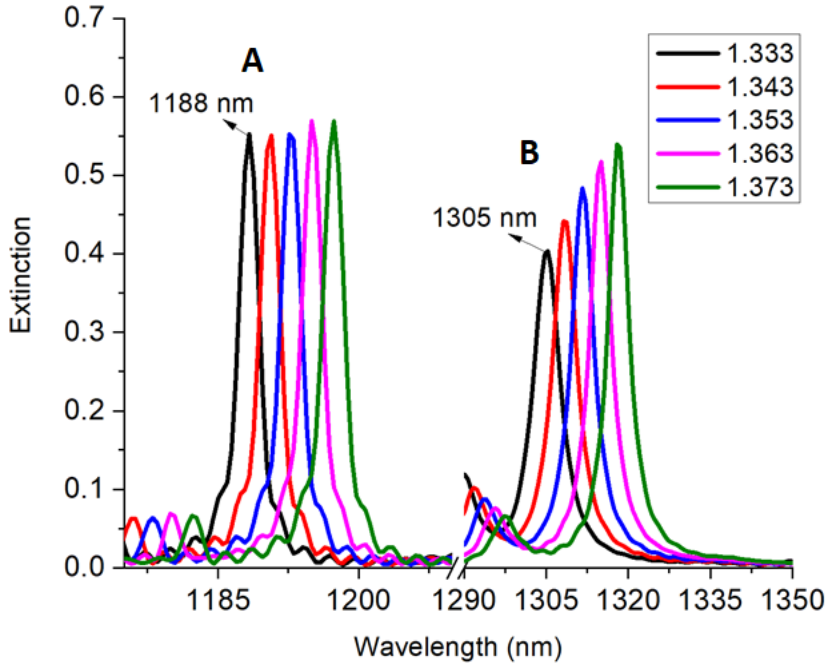

Figure 2.7 The recorded extinction spectra of the Au-G hybrid nanostructure of 60-nm nanoparticle diameter, 7 nm thick graphene shell, and 300 nm structural periodicity.

From Fig. 2.7, the shifts in resonance wavelength and resonance intensity were clearly observed, as the refractive index of the sensing medium changed for both A and B modes. For example, resonance mode A was shifted from 1188 nm to 1197 nm, and the resonance intensity of mode B was shifted from 1305 nm to 1318 nm as the refractive index of the sensing medium changed from 1.333 to 1.373. Using the following equations, the sensitivity and FOM of the Au-G hybrid nanostructure for modes A and B, based on the resonance wavelength and intensity shift, were calculated and summarized in Table 2.2.

$$S_\lambda = \frac{\Delta\lambda}{\Delta n} \ (nm/RIU) \qquad (2.2)$$

$$S_I = \frac{\Delta I}{\Delta n} \ (RIU^{-1}) \qquad (2.3)$$

$$FOM_{\lambda} = \frac{S_{\lambda}}{\text{FWHM}} \quad (2.4)$$

$$FOM_{I} = \frac{S_{I}}{I_{ref.}} \quad (2.5)$$

In equations 2.2 – 2.5, $\Delta\lambda$ is the change in resonance wavelength (nm), ΔI is the change in intensity, and S_{λ}, FOM_{λ} , S_{I} , FOM_{I} are sensitivity and figure of merit based on wavelength and intensity shift, respectively. Therefore, by obtaining the resonance intensity and resonance wavelength from Fig. 2.7 at each refractive index, and using equations 2.2 – 2.5, the sensitivity and FOM based on intensity shift and wavelength shift, respectively, were calculated.

As detailed in table 2.2, the calculated FOM from the S_{λ} was increased in the range of 57.69 to 102.64, which shows a significant improvement in the sensor performance of Au-G hybrid nanostructure compared to the previous one reported by Maurer et al., in which they obtained a FOM of 2.8 by inserting graphene film between a Au film and Au NP array [79]. Furthermore, the FOM obtained here shows a large improvement compared to the Ag-G hybrid nanostructure studied by Pan et al., where the maximum FOM obtained was 20 [80], in addition to other nanostructures studied in the literature and reported in the review paper published by Mayer and Hafner [11], where values for FOM were lower than 10.

Table 2.2 Resonance wavelength, bulk resonance, intensity sensitivity, FWHM, and FOM of resonance modes in a Au-G hybrid nanostructure with a Au diameter of 60 nm, graphene thickness of 7 nm, and structural periodicity of 300 nm.

Resonance Peak	λ_{res} (nm)	S_λ(nm/RIU)	S_I(RIU^{-1})	FWHM (nm)	FOM_λ	FOM_I
A	1190	200	0.3	2.64	75.75	0.11
	1193	250	0.2	2.69	92.94	0.07
	1195	233	1.7	2.27	102.64	0.75
	1197	225	-	2.69	83.64	-
B	1308	300	3.9	5.20	57.69	0.75
	1312	350	4.2	4.80	72.91	0.47
	1315	333	3.3	4.61	72.23	0.72
	1318	325	2.2	4.55	71.43	0.48

On the other hand, improvements in the FOM obtained from S_I sensitivity, such as the increase from 0.07 to 0.75 at resonance mode A, show the capability of improving the sensing performance of the sensor via intensity shift, not only from wavelength shift. A somewhat larger variation was noticed in the sensitivity based on intensity shift, such as 1.7 compared to 0.3 & 0.2, which was due to a larger intensity shift in mode A as shown in Fig. 2.7 when the refractive index changed from 1.353 to 1.356. Furthermore, the obtained sensitivity, based on the wavelength shift,

shows no improvement compared to the literature [11]. However, the sharp resonance obtained here of 2.5 nm (FWHM), indicates that this sensor is competitive in terms of the high FOM achieved with a value of 102.64.

The proposed sensor can be fabricated by using the following steps: deposition of graphene film on top of a quartz substrate and then growth of a Au NP array on top of graphene film, followed by graphene deposition and removal of the unwanted area. Fig. 2.8 shows the details of the suggested fabrication process. Electron beam lithography is required twice with a high level of controllability. However, for an easier approach, another fabrication plan could be applied that neglects the lower portion of graphene. The Au nanoparticle arrays with particle diameter (d) in the range of 40 to 60 nm can be fabricated on a quartz substrate using electron-beam lithography technique, as discussed in detail elsewhere [81]. The fabricated nanostructure is then covered with a multilayer (less than 10 layers) of graphene nanopowder, followed by thermal annealing under a controlled environment, as discussed in detail by [82]. In the last step, lithography and reactive ion etching were employed to remove graphene nanopowders from the area between the hybrid nanostructures [83]. Fig. 2.8 shows the detailed steps of fabrication, which involve steps that require a high level of controllability.

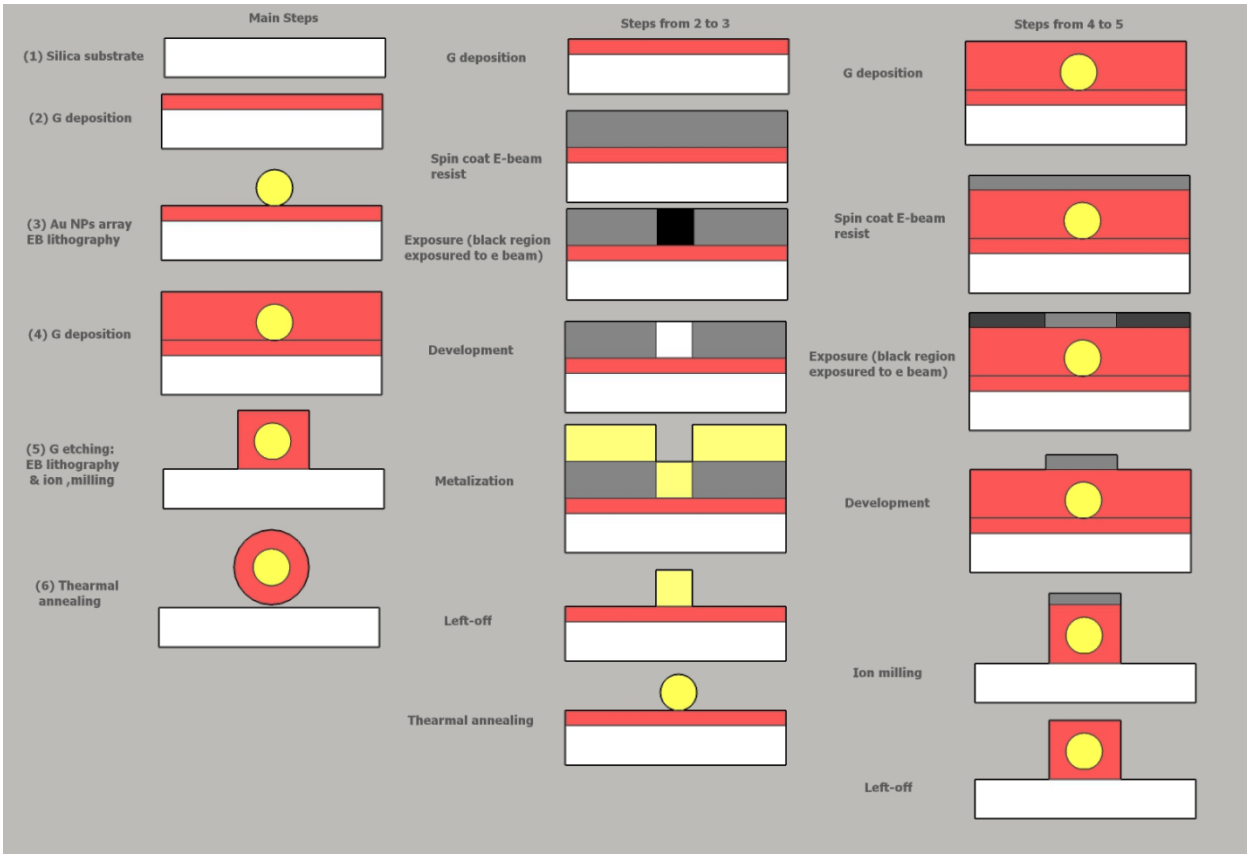

Figure 2.8: Schematic illustration of fabrication process for core-shell NP array nanostructure.

2.4 Conclusion

The effects of periodicity, metallic nanoparticle size, and graphene shell thickness of the Au graphene hybrid nanostructure on the optical properties, sensitivity, and FOM of a Au-graphene hybrid nano-sensor were studied numerically. Encapsulating the Au nanoparticles with a multilayer of graphene enhanced the extinction intensity (absorption) at the NIR region followed by a narrow resonance mode with a FWHM as low as 2.5 nm that increased the FOM of the proposed sensor as high as 102.6. This shows a significant improvement in Au nanoparticle-based sensors by incorporation of a thin layer of graphene. The results shown here confirm that

resonance properties strongly depend on hybrid nanostructure size and graphene shell thickness. It was also shown that the proposed sensor can measure two different types of sensitivities based on resonance wavelength shift and resonance intensity shift, which gives this sensor a unique applicability for a variety of purposes. The obtained results provide evidence of the effective role of hybrid graphene with gold on the LSPR sensor's performance. However, having a sensor with competitive sensing performance that can be created with a minimum number of fabrication steps and a high level of controllability and reproducibility is the optimum engineering goal, which is considered in forthcoming chapters by the design and study of the plasmonic properties of different Au-G hybrid nanostructures.

Chapter 3 Au NP-Graphene Film Hybrid Nanostructure for Localized Surface Plasmonic Resonance Sensor[2]

In this chapter, a multilayer graphene film decorated with a Au nanostructure was proposed as a liquid sensor. The results showed a significant improvement in the figure of merit compared with other reported localized surface plasmon resonance sensors. The maximum figure of merit values of 240 and 390 were achieved based on intensity shift and wavelength shift, respectively, at a refractive index change of 0.001, which indicates the capability of the proposed sensor to detect a small change in concentration of liquids, which is helpful in early-stage cancer disease detection.

[2] This is an Accepted Manuscript of an article published by Alharbi, R., Irannejad, M., & Yavuz, M. in Sensors on 19 January 2017, available online https://link.springer.com/article/10.1007%2Fs11468-016-0325-z [Article DOI : 10.3390/s17010191]. "Au-Graphene Hybrid Plasmonic Nanostructure Sensor Based on Intensity Shift"

3.1 Introduction

In Chapter 2, it has been shown that gold-graphene core-shell hybrid nanoparticle arrays offer significant improvement in LSPR sensor performance, and a lower periodicity results in a superior plasmonic resonance band in terms of FWHM. As graphene was the shell material of the studied hybrid NP (Chapter 2) and decreasing the periodicity gives better plasmonic properties, the idea arises to fill the area between gold NPs in the array with graphene and explore the plasmonic property of the new gold-graphene hybrid nanostructure. For simplicity, this hybrid nanostructure is considered in a 2D scheme as shown in Fig. 3.1. In this chapter, therefore, a 2D periodic structure of embedded Au NPs with different shapes in a multilayer graphene film is studied as a plasmonic sensor. A two-dimensional array of Au NPs with different shapes (i.e., cubic, cylindrical, and prism) were placed on a quartz substrate and the gap between them was filled with multilayer graphene film, as shown in Fig. 3.1. A series of nanostructure arrays were systematically studied to simultaneously obtain a sensor device with higher FOM and bulk sensitivity. According to the previous study (Chapter 2), the center-to-center distance between two consecutive particles was chosen as 300 nm, and here reduced by increasing the Au NP dimension from 50 nm to 300 nm. The size-to-separation distance ratio (L/P) was varied from 0.17 to 1 and the thickness of the nanostructure was fixed at 20 nm. L and P indicate the NPs lateral size and structural periodicity, respectively.

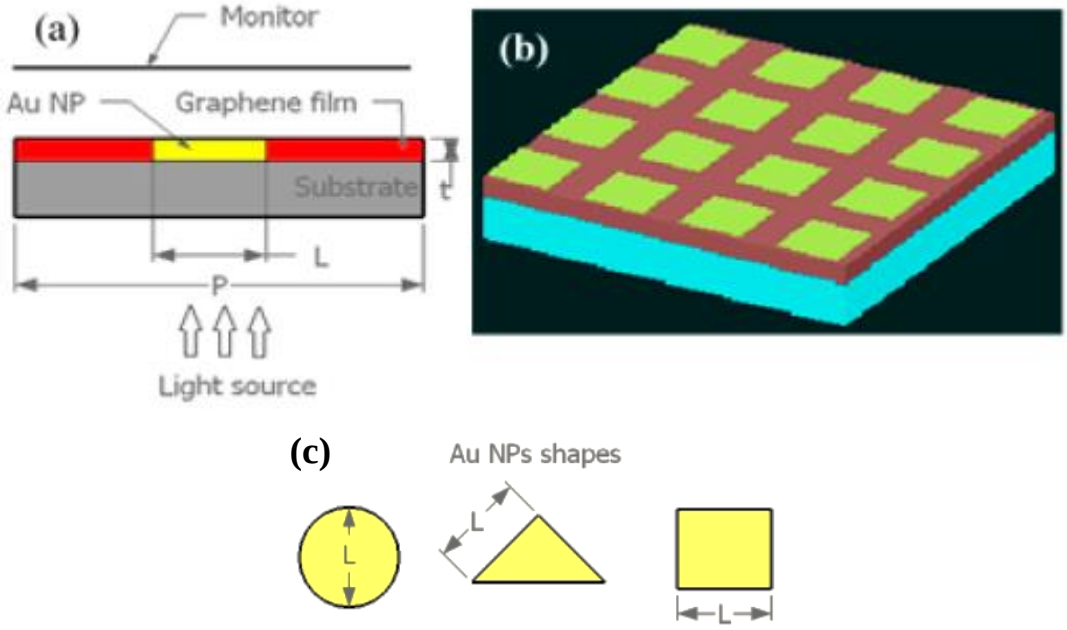

Figure 3.1 (a) 2D schematic diagram of the proposed sensor used in this study. L is the side length of cubic and prism NPs and the diameter of the cylindrical NPs, t is the thickness of NPs, and P is the periodicity of the NPs; (b) is the perspective view of the Au-graphene hybrid sensor; (c) top view of three shapes (cylinder, prism, & cube) used for NPs in this chapter.

The extinction spectrum was calculated at the near-infrared (NIR) region (λ = 1.5 to 2 μm), which is a desired region for detection of biomarkers (e.g., breast cancer biomarkers) using blood serum [73]. The refractive index of the sensing medium was varied from 1.333 to 1.341, with a step of 0.001 to measure the ability of the proposed nanostructure sensor to detect small variations in concentration. The sensor can be fabricated by depositing graphene film, and subsequently, by direct milling using a focused ion beam (FIB) [84], nano holes can be fabricated. Next, using focused ion beam (FIB), the gold NP can be deposited on specified holes.

3.2 Methodology

In this study, the FDTD method was employed to examine the extinction properties and sensitivity of a series of nanostructures with different geometrical parameters fabricated on a quartz substrate. The refractive index of the substrate was considered to be 1.45, and the refractive index of the superstrate (i.e., target materials for sensing application) was varied from 1.333 to 1.341 with a 0.001 step. In this device, smaller refractive index changes than those stated in Chp 2 were considered, where detecting a smaller amount of refractive index change increases the capability of the sensor to detect a smaller amount of analyte concentration change.

The numerical analysis was carried out using the FDTD package from Lumerical FDTD Inc. The Au-G hybrid nanostructure, plane wave source, and transmission (T) monitor were co-planar with the boundary conditions that made them infinite in the x- and y-directions, as shown in Fig. 3.1a. A non-polarized plane wave source, emitting wavelengths in the range of 1.5 μm to 2 μm with electric field amplitude of 1 V/m, was propagated along the z-axis as incident light source at normal incidence. Anti-symmetric and symmetric boundary conditions were applied in the x- and y-directions respectively, and the perfect matching layer (PML) boundary condition was chosen in the z-axis. The mesh cell size (point-to-point distance) was 5 nm in the x and y directions and 2 nm in the z-direction, and the calculation time was set as 3000 fs. The transmission spectra were calculated using an x-y monitor 150 nm away from the Au-G/superstrate (liquid) interface. The plane wave source was placed 150 nm below the structure. Air (n = 1) was chosen as the background and water (n = 1.333) was used as a reference medium in the sensitivity and FOM measurements.

3.3 Results and Discussion

3.3.1 Contribution of the Hybrid Au-Graphene (Au-G) Nanostructure

The Au-G hybrid optical spectrum was compared with the optical spectra of two different nanostructures. The first is a square nanohole array perforated in a multilayer graphene film on a silica substrate, and the second is a 2D array of Au NPs placed on a silica substrate. In the first structure, a series of square nanoholes with side length of L = 50 nm, thickness of 20 nm, and periodicity of 300 nm was perforated in multilayer graphene sheets on the silica substrate. In the second case, a Au NP array with dimensions equal to the size of the nanohole array (first structure) and the same structural parameters were studied. The extinction spectrum of each structure was calculated using 1-T. Fig. 3.2a shows the extinction spectra of a 2D nanohole array perforated in the multilayer graphene film (green curve), cubic Au NPs array (red curve), and cubic Au NPs/graphene film hybrid structure (blue curve) over a wavelength range of 1500 nm to 2000 nm. As can be seen from this figure, no significant resonance modes were observed in the Au cubic NP square array, while a number of resonance modes were recorded in the nanohole array structure. The first three resonance mode wavelengths of 1532 nm, 1632 nm, and 1793 nm are labeled as resonance modes I, II, and III, respectively. These modes are used for further analysis due to better band sharpness such as resonance mode III and due to longer wavelength resonance, as longer wavelength resonance exhibits superior sensitivity to the surrounding refractive index

change [85]. A maximum extinction of 0.3 was obtained at the resonance wavelength of 1793 nm. It was found that by filling the graphene nanohole with Au NPs, the resonance wavelengths were shifted by 19 nm, 24 nm, and 67 nm, respectively, for resonance modes I, II, and III, as shown in Fig. 3.2a. The recorded redshift in the resonance modes can be attributed to an increase in the refractive index of the surrounding medium (hole + sensing medium) by adding the Au NP in the nanohole, as confirmed by equation 3.1, where it represents the plasmonic resonance wavelength of the nanohole array and shows that increasing n_a (refractive index of the surrounding medium) redshifts the plasmonic resonance wavelength [86].

$$\lambda = \left[\left(\frac{m}{a_x}\right) + \left(\frac{n}{a_y}\right)\right]^{-\frac{1}{2}} \sqrt{\frac{\varepsilon_m n_a^2}{\varepsilon_m + n_a^2}} \qquad (3.1)$$

Where ε_m is the permittivity of dispersive material (graphene and Au-G hybrid), n_a is the refractive index of the dielectric medium, m and n are integer resonance orders, and $a_x = a_y = P$ represent the structural period of the array.

Fig. 3.2a also shows that the extinction intensity of resonance mode III was reduced (from 0.3 to 0.2) on filling the nanoholes in the graphene film with Au NPs, while the extinction intensity of resonance modes I and II were increased. The resonance modes in the perforated holes in the graphene sheets were excited due to the extraordinary optical transmission (EOT) effect [86]. By using a nanohole array, two different types of resonance modes are expected: a resonance mode from the nanohole/substrate interface (bottom of the structure) and another one from the nanohole/superstrate interface (top of the structure) [47]. Therefore, it is expected that resonance mode III belonged to the mode created at the hole/superstrate interface, while modes I and II were recorded due to the surface plasmon resonance at the hole/substrate interface [87]. Fig. 3.2b–d show the electric field profiles at the resonance wavelengths of 1532 nm, 1632 nm, and 1793 nm

respectively, for a square nanohole array of a multilayer graphene film with 50 nm width and 20 nm thickness. The effects of filling the nanoholes with Au on the electric field profile at the resonance wavelengths in the Au-G hybrid structure (Fig. 3.1b) are compared in Fig. 3.2e–g. From these figures, a quadrupole resonance is mainly responsible for resonance mode excitation in the Au-G hybrid structure. It was found that the electric field was localized at the edges of the nanoholes in the y-direction (Fig. 4.2b–d) while it was propagated along the x-direction in the hybrid structure (Fig. 3.2e–g).

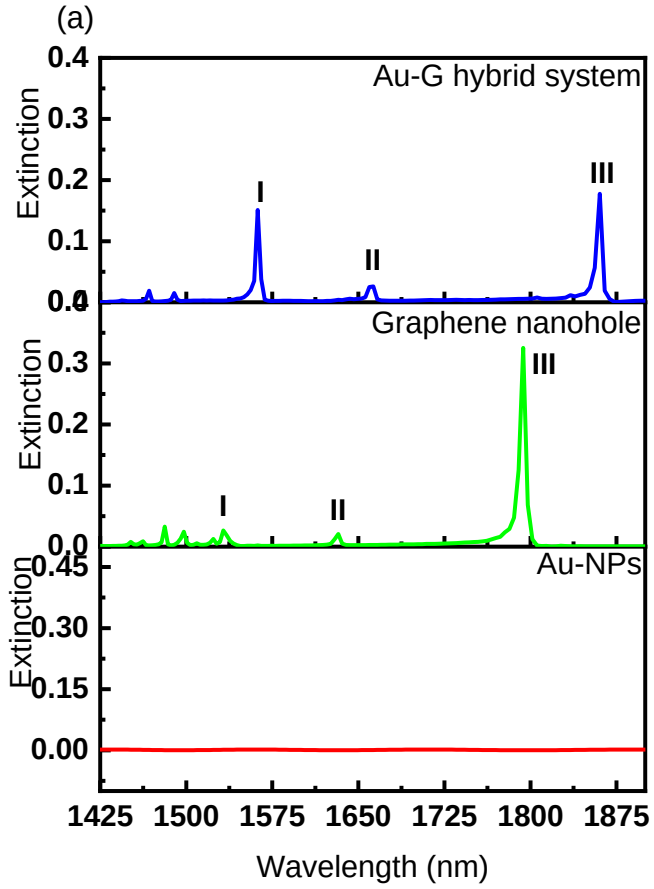

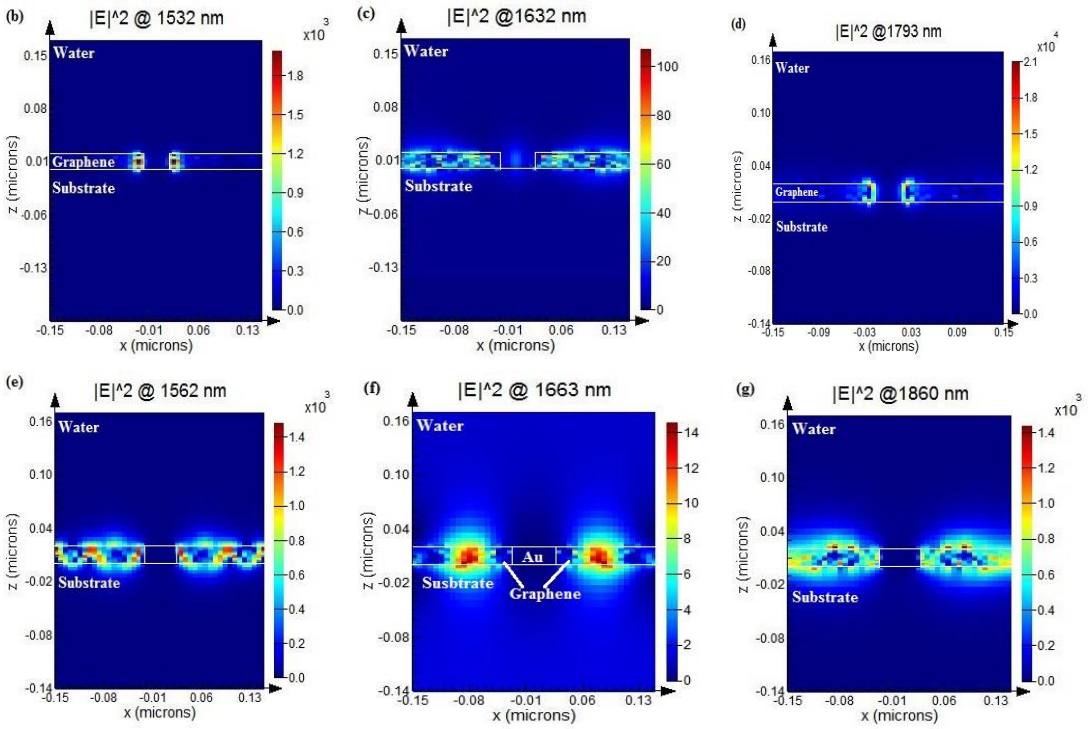

Figure 3.2 Top row : (a) extinction spectrum for three different nanostructures; Au NP square array, nanohole array perforated in 20 nm thick graphene film, and Au NPs/G hybrid structure. Middle row: electric field profiles at the resonance wavelengths of (b) 1532 nm (mode I), (c) 1632 nm (mode II), and (d) 1793 nm (mode III) of the graphene nanohole structure. Bottom row: Au-graphene hybrid structure at resonance wavelengths of (e) 1562 nm (mode I); (f) 1663 nm (mode II), and (g) 1860 nm (mode III), respectively.

3.3.2 Effects of Au NP Size, Shape, and Structural Periodicity on Extinction

The effects of Au NPs' size, shape, and separation distance (P) on the extinction spectrum were systematically studied using numerical analysis. A series of Au NPs with different shapes (cubic, cylindrical, and prism), different particle sizes, L, in the range of 50 nm to 300 nm (L/P ratio in

the range of 0.17 to 1), and a fixed height of 20 nm were investigated. Fig. 3.3 shows the extinction of the resonance modes of the hybrid Au-G nanostructure with prism, cubic, and cylindrical NPs at different L/P ratios. The effects of increasing the L/P ratio and using prism Au NPs on the extinction of the Au-G hybrid nanostructure are compared in Fig. 3.3a. As can be seen from this figure, increasing the L/P ratio from 0.17 to 1 resulted in a blueshift as large as 363 nm in the resonance wavelength of resonance mode III, and a similar trend was also observed by using the cylindrical and cubic NPs, as is evident in Fig. 3.3b, c, respectively. Blueshift in the resonance mode after increasing the L/P ratio is due to decreasing the distance between the NPs, and from equation 3.1, it is clear that decreasing the periodicity results in blueshift of the resonance [86].

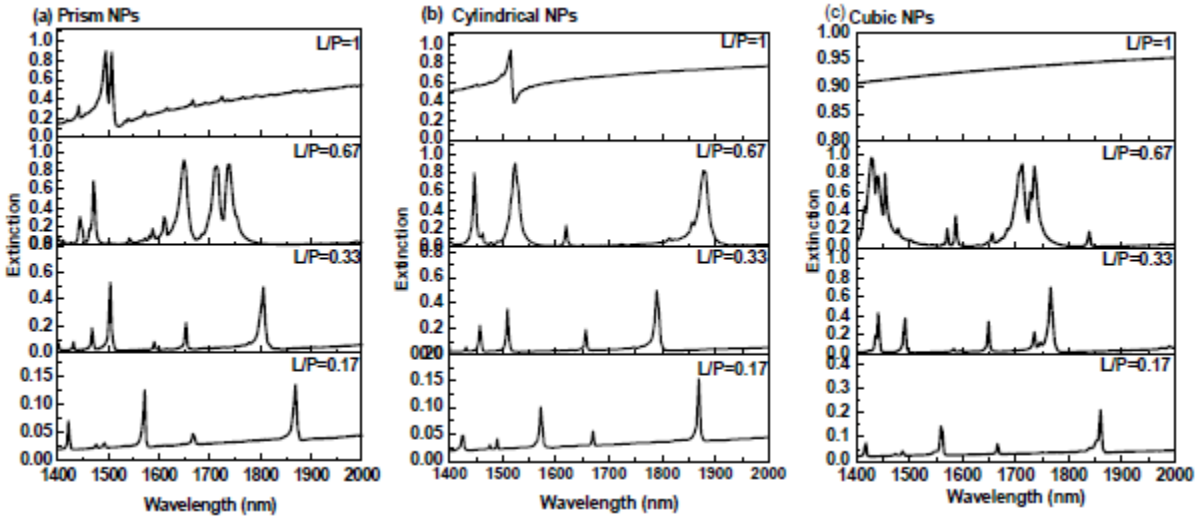

Figure 3.3 Extinction spectra of hybrid nanostructure with (a) prism; (b) cylindrical; and (c) cubic NPs at different L/P ratios and thickness of 20 nm.

It was also found that on increasing the L/P ratio, the extinction intensity of resonance mode III was increased in all three Au-G hybrid structures, as clearly shown in Figure 3.4a. It is

known that graphene has a constant absorption coefficient in the visible-to-NIR range [88]; therefore, it can be concluded that increasing the extinction intensity on increasing the L/P ratio could be attributable to the Au NP absorption, where larger NPs resulted in more extinction, as reported by Zuber et al. [89] as they found that the absorption of gold NPs is higher for larger sizes than for smaller sizes.

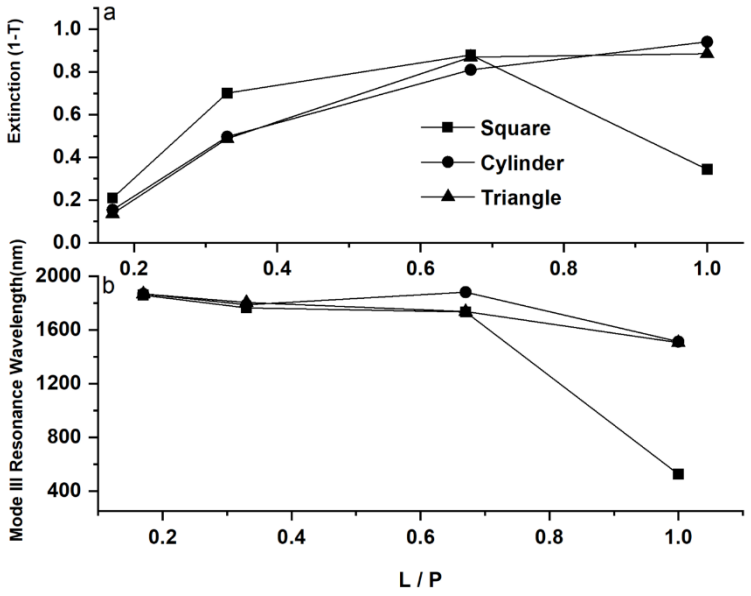

Figure 3.4 (a) Extinction and (b) resonance wavelength (mode III) as a function of the L/P ratio. L is the side length and P is the periodicity of the nanostructure.

A maximum extinction peak intensity of 0.94 was achieved at L/P = 1 in the hybrid nanostructure with cylindrical NPs at a resonance wavelength of 1514 nm while there are no extinction peaks in the recorded spectrum for a nanostructure at L/P = 1 with cubic NPs. The explanation is that at L/P = 1, the cubic NPs become a continuous gold thin film. Fig. 3.4b shows the mode III resonance wavelength positions of all hybrid systems as a function of the L/P ratio.

It is expected that increasing the L/P ratio resulted in a blueshift in the recorded resonance wavelength in the hybrid nanostructures [86] as shown in Fig. 3.4b.

3.3.3 Sensitivity Measurement

The plasmonic resonance wavelength, and hence the sensitivity of a plasmonic sensor, strongly depends on the refractive index variation of the surrounding environment. The optical response of a Au-G hybrid structure with cubic NPs to the refractive index variations in the range of 1.333 to 1.337 is shown in Fig. 3.5. It is clear from this figure that no comparable shift in the resonance wavelength on increasing the refractive index at all three resonance modes was observed. However, the extinction intensity of the resonance modes was changed. Therefore, the intensity shift can be used to measure the sensitivity of the proposed sensor. The intensity sensitivity is calculated by dividing the change in the extinction intensity by the change in refractive index ($S_I = \Delta I/\Delta n$) [90]. As shown in Fig. 3.5, the intensity sensitivity at a longer resonance wavelength is larger than at the shorter one, which agrees with the literature [32] where longer wavelength resonance presents better sensitivity. The intensity sensitivity at $\lambda = 1860$ nm was measured as 17 RIU^{-1}, while at shorter resonance wavelength ($\lambda = 1562$ nm) it was decreased to 12 RIU^{-1}. Thus, the resonance mode at 1860 nm was chosen to study the effect of using different geometrical structures on the sensitivity and FOM of the Au-G hybrid refractive index sensor.

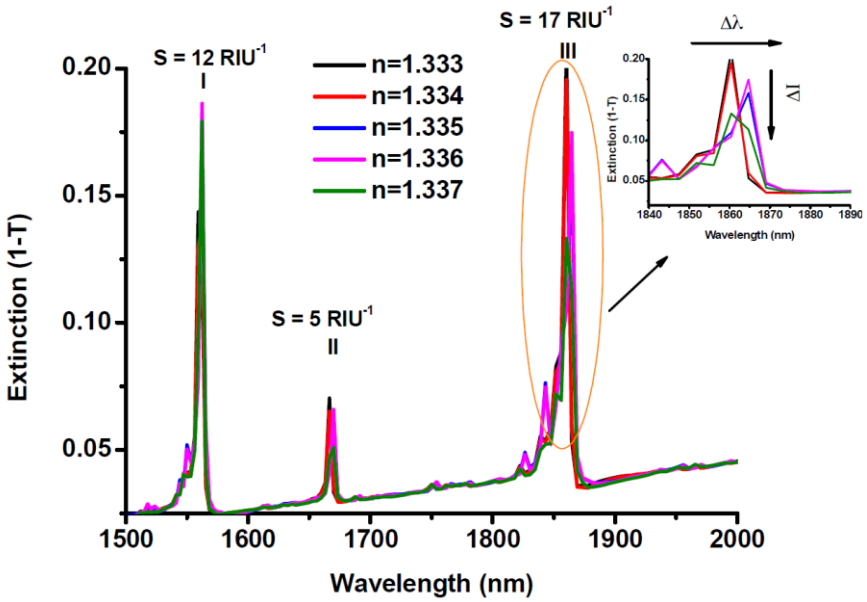

Figure 3.5 Extinction spectrum of a hybrid nanostructure with cubic NPs at L/P = 0.17.

The intensity sensitivity and FOM of different sensors with three different NP shapes (cubic, cylindrical, and prism), with different L/P ratios in the range of 0.17 to 1 (side-length, L, was varied in the range of 50 to 300 nm), and a fixed thickness of 20 nm, were studied using the third resonance mode (λ = 1860). The extinction, sensitivity, and FOM of all sensors were calculated on increasing the refractive index from 1.333 to 1.341 with an increment step of 0.001. In the case of using intensity shift of the resonance peak, the FOM was calculated by dividing the sensitivity of the resonance mode of the target liquid by the resonance intensity at the reference point (FOM = $S_I/I_{resonance}$).

It was found that increasing the L/P ratio resulted in an increase in the extinction intensity in all different NP shapes (except cubic shape at L/P = 1) as shown in Fig. 3.6, which could be attributed to stronger absorption of the incident light by Au NPs at larger L/P values that in turn are attributed to higher absorption in larger Au NP sizes, as reported by Zuber et al. and Shen et

al. [89,91]. In the case of a cubic shape with L/P = 1, no resonance was observed (Fig. 3c) because the nanostructure becomes a continuous film where the resonance between the NPs array is diminished. As can be seen from Fig. 3.6b, the maximum extinction intensity of 0.95 was recorded on using the cylindrical NPs with a diameter of 300 nm and 20 nm height and as it is evident from Fig. 3.6a, the lowest extinction intensity of 0.102 was recorded in the Au-G hybrid structure using prism NPs with a side-length of 50 nm. From these figures, it is also clear that there were no monotonic increases in the extinction as the L/P increases. In a Au-G hybrid structure with cubic NPs, the maximum extinction was recorded as large as 0.7 at L/P = 0.33 (Fig. 3.6c), while by using the prism NPs, it was increased to 0.9 at L/P = 0.67 (Fig. 3.6a).

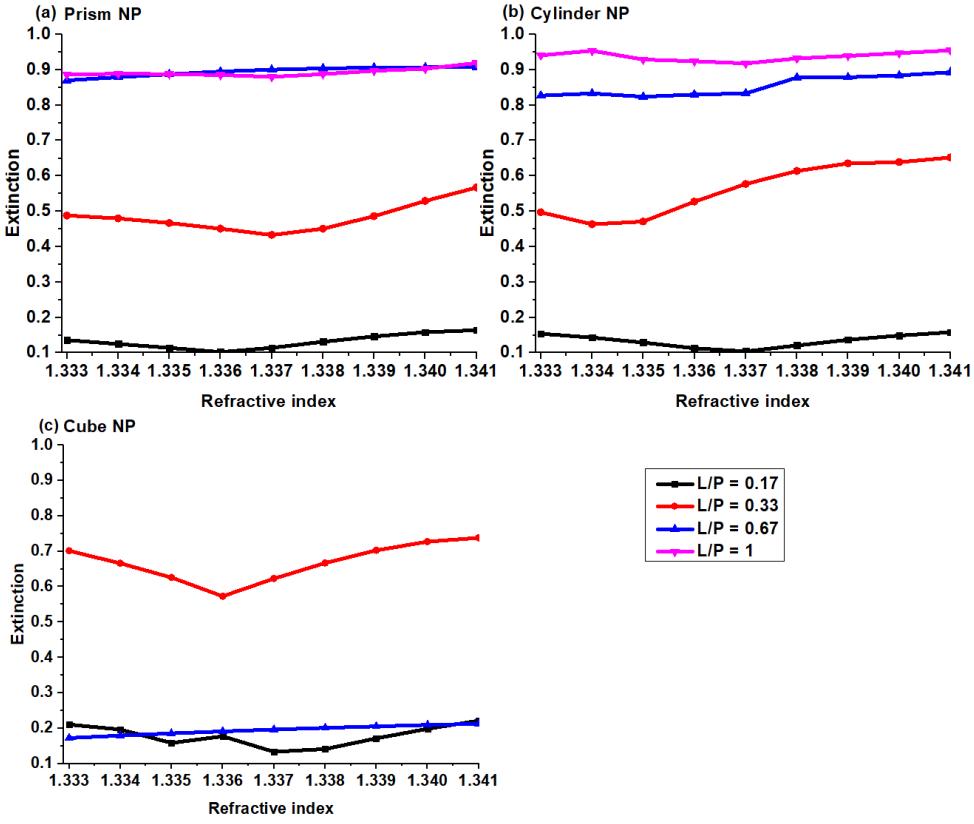

Figure 3.6 Extinction intensity of the hybrid Au-G nanostructure with (a) prism; (b) cylindrical; and (c) cubic NPs at different L/P ratios as a function of refractive index

The variation of sensitivity (S_I) of the Au-G hybrid sensor on increasing the refractive index change at different L/P ratios in all three types of Au-G hybrid sensors was compared in Fig. 3.7. As can be seen, maximum sensitivities of 43 RIU $^{-1}$, 56 RIU $^{-1}$, and 53 RIU $^{-1}$ were obtained for L/P = 0.33 in the Au-G hybrid sensors with prism (Fig. 3.7a), cylindrical (Fig. 3.7b), and cubic (Fig. 3.7c) NPs, respectively. By comparing the sensitivity of Au-G hybrid sensors with different NP shapes, there is no clear relation between the sensitivity and L/P ratio and NP shapes, which shows the complexity of response of a plasmonic nanostructure when different parameters are considered. For instance, at some refractive index changes, such as 1.333 to 1.334 for prism NPs, L/P = 0.17 presents greater sensitivity, which is the opposite case when the refractive index changes from 1.34 to 1.341. The maximum sensitivity recorded was ~56 RIU^{-1} for cylindrical NPs at L/P = 0.33 at a refractive index change from 1.335 to 1.336. Like sensitivity, there is no clear relation observed between the FOM and L/P ratio and NP shapes, as shown in Fig. 3.8. This is expected where the FOM depends on the sensitivity, resulting in similar behavior. The maximum FOM, as large as 240, was achieved at L/P = 0.17 (NP size = 50 nm) (Fig. 3.8c) in a hybrid sensor with cubic NPs.

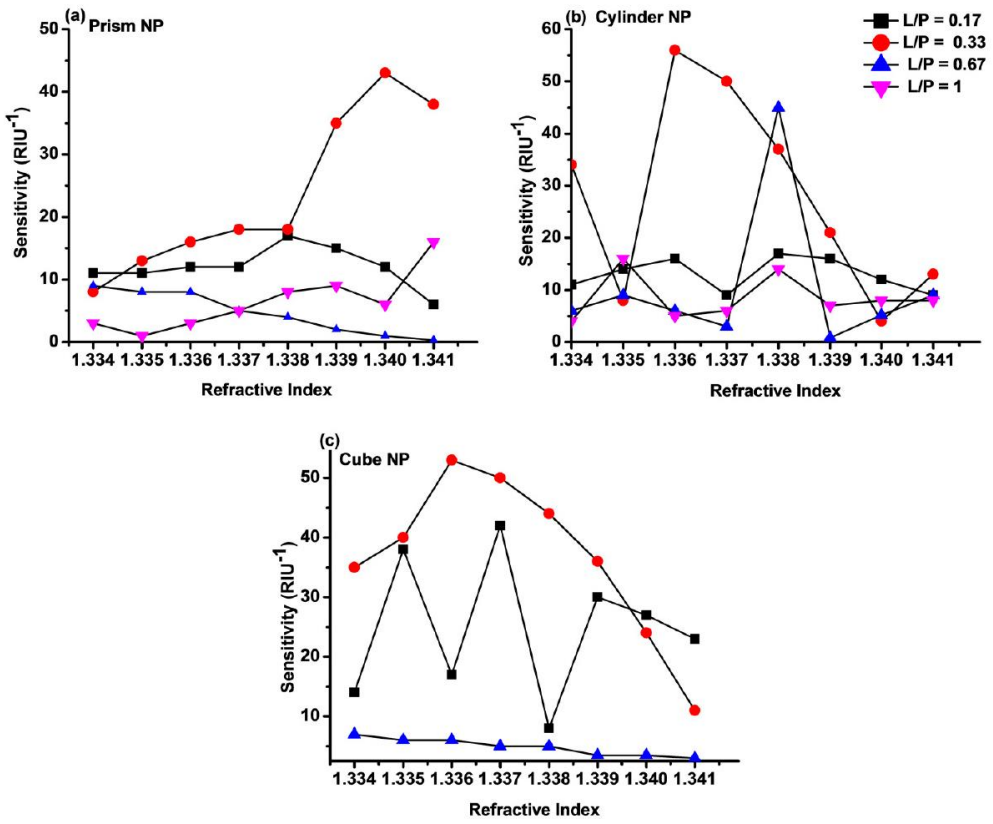

Figure 3.7 Sensitivity of the hybrid Au-G nanostructure with (a) prism; (b) cylindrical, and (c) cubic NPs at different L/P ratios as a function of the refractive index.

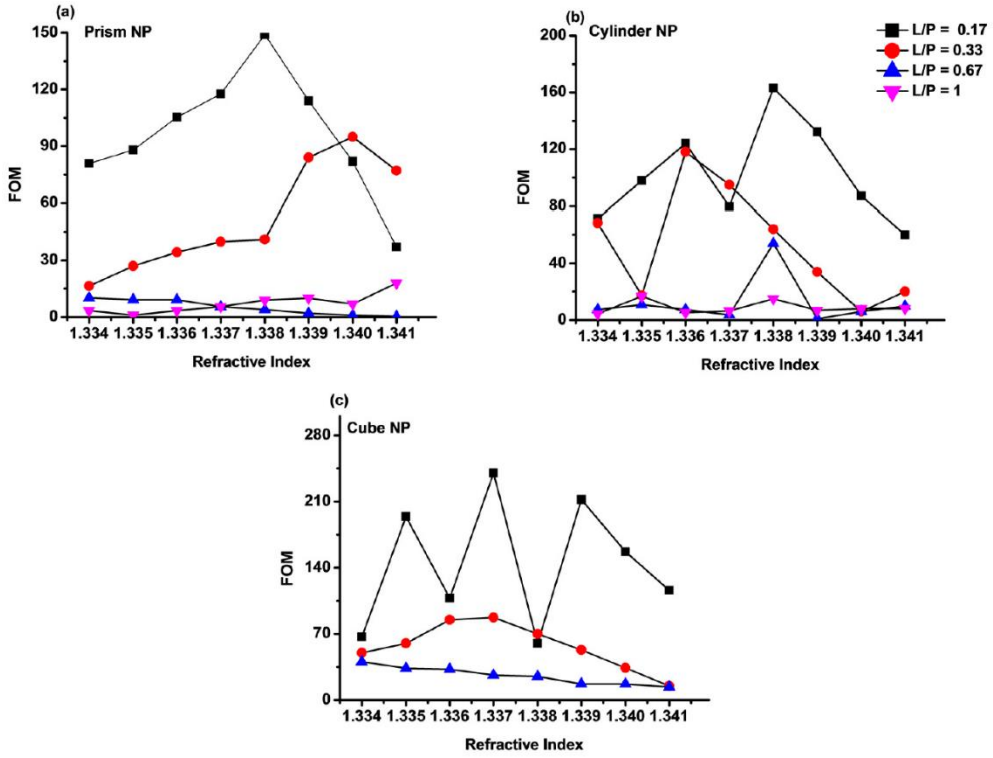

Figure 3.8 FOM of the hybrid Au-G nanostructure with (a) prism; (b) cylindrical; and (c) cubic NPs at different L/P ratios as a function of the refractive index.

Furthermore, at some L/Ps, a resonance wavelength shift up to 4.4 nm was also recorded in the hybrid sensors by using different NPs shapes at different L/P ratios and refractive index changes as summarized in Table 3.1. From this table, it is clear that the maximum FOM of 390 was obtained in a Au-G hybrid sensor with cylindrical NPs at L/P = 0.33 by increasing the refractive index from 1.334 to 1.335; whereas the maximum sensitivity, as large as 4380 nm/RIU, was obtained in a hybrid sensor with prism NPs at L/P = 0.33, which resulted in a FOM of 273 as the refractive index increased from 1.336 to 1.337.

Table 3.1 Maximum sensitivity and FOM values based on wavelength shift in different Au-G hybrid structures with prism, cylindrical, and cubic NPs at specific changes in the refractive index and at L/P = 0.33.

NP	$\lambda_{resonance}$(nm)	Shift (nm)	n_1	n_2	S_λ(nm/RIU)	FOM
Prism	1805	4.38	1.336	1.337	**4380**	273
Cylindrical	1789	4.02	1.334	1.335	4020	**390**
Cubic	1765	4.34	1.334	1.335	4340	307

In addition to the better sensing performance obtained here, this studied hybrid nanostructure can be fabricated, as shown in Fig. 3.9, with a smaller number of and more controllable fabrication steps than in the spherical core-shell nanostructure studied in chapter 2.

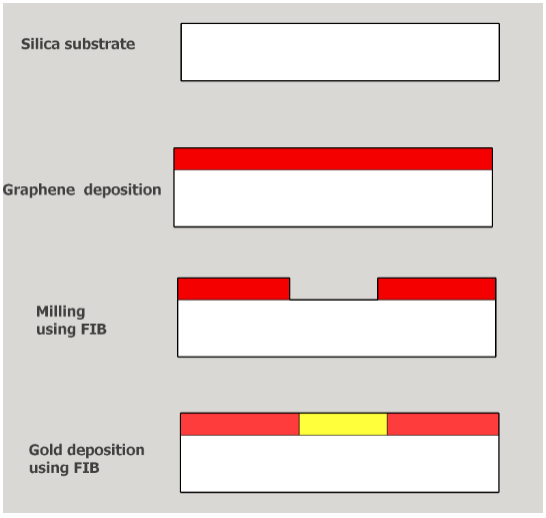

Figure 3.9: schematic illustration of the main fabrication steps of the Au NP- G film hybrid nanostructure.

Here, the hybrid nanostructure can be fabricated using only three main steps: graphene deposition, perforating of nanoholes, and finally, gold deposition. Graphene film deposition can be performed using the CVD method followed by direct milling using a focused ion beam (FIB) [84] to produce nanoholes. After that, the SEM system is equipped with a focused ion beam (FIB), so that the electron beam induced deposition (EBID) technique can be used to deposit the gold locally in the hole via focusing an electron beam. As shown schematically in Fig. 3.10, irradiating a localized region on the substrate using an electron beam generates secondary electrons which cause a chemical decomposition of the organometallic gas precursor and, as a result, deposition of metal nanostructure in the irradiated region. Therefore, by focusing the e-beam into the hole (as in the proposed nanostructure here) the gold material can be deposited inside the hole [92]. By applying EBID technique, Dhawan et al. deposited gold nanopillars on top of ITO-coated glass, showing the high controllability of local deposition of metal nanostructures [92].

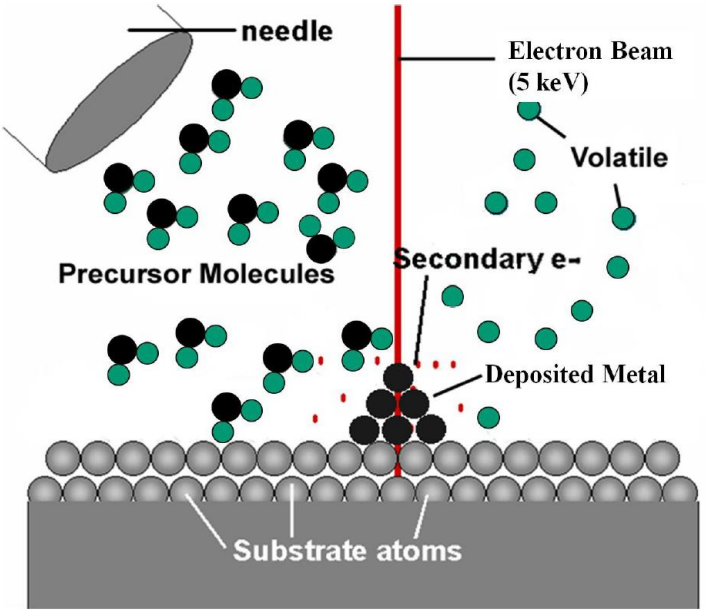

Figure 3.10: Schematic representation of how electron-beam induced deposition is used in the deposition of metal nanostructures [92]

3.4 Conclusion

Extinction properties, sensitivity, and FOM of the hybrid Au-G plasmonic sensors with different NP shapes were numerically studied. The optical spectroscopy of the proposed sensors shows that the resonance phenomena were observed at a near-infrared region due to the presence of graphene layers. Intensity, sensitivity, and FOM of all hybrid sensors were also studied for $\Delta n = 0.001$. A significant improvement in the FOM and sensitivity of the hybrid sensors was achieved. The maximum FOM, as large as 390, and a high sensitivity, as large as 4380 nm/RIU, were recorded, which enhance the capability of the LSPR sensors in sensing and detecting low-concentration analyte levels. The current results increase the capability of LSPR sensors to compete with PSPR sensors. The 2D hybrid scheme of gold and graphene studied in this chapter showed better performance results compared to the 3D scheme studied in Chapter 2; however, it is suitable for sensing applications that require single or few NP sensors, only due to the long time required for the milling process using FIB. Therefore, in the next chapter, a somewhat similar hybrid scheme is studied, although it can be fabricated with a few and controllable fabrication steps and can be produced on a large scale.

Chapter 4 Direct Deposition of Graphene Sheets on Top of Gold Nanodisk Array for Enhancement of Localized Surface Plasmon Resonance Sensor Performance[3]

In this chapter, a new graphene-gold hybrid nanostructure is proposed and its plasmonic properties (sensitivity and FOM) are studied as dielectric properties of the medium around the nanostructure change. To ensure applicability of the proposed nano-device, it has been designed in a way to make certain its fabrication employs conventional nanofabrication techniques via well-known fabrication steps. The results show that there is a significant improvement in LSPR sensor performance, in which a sensitivity of 2460 nm/RIU and a FOM of 857.8 are achieved. Furthermore, these promising sensitivity and FOM values are observed at a very low dielectric property change (refractive index change = 0.001), indicating the proposed sensor's ability to detect low-concentration change of bio analyte, which is very helpful in applications such as early cancer disease diagnosis.

[3] This is a planned for publication manuscript of an article by Alharbi, R. & Yavuz, M. "Direct Deposition of Graphene Sheets on Top of Gold Nano-Disks Array for Enhancing Localized Surface Plasmon Resonance Sensor Performance"

4.1 Introduction

According to the results obtained, as stated in Chapters 2 & 3, hybridizing gold with graphene, either in 3D or 2D schemes, showed a significant improvement in LSPR sensor performance. However, fabrication of 2D materials presents a challenge, especially in non-planar geometry, or when these hybridize with other materials such as gold. A metal-2D hybrid nanostructure therefore, with a competitive sensing-performance, and a few, controlled, well-known fabrication steps represents the optimal target. For this reason, in this chapter, the effects of direct deposition of graphene film on top of a Au nano-disk (ND) array on localized plasmonic sensor performance (S and FOM) have been studied numerically using the finite difference time domain (FDTD) method. The effects of graphene film thickness on plasmonic resonance properties are considered, followed by sensitivity measurement of the hybrid nano-device. After illustrating the research methodology, the results are presented and discussed, followed by a discussion of fabrication applicability and uses.

4.2 Methodology

The plasmonic sensing properties of a gold-graphene hybrid nanostructure were studied numerically using the FDTD method. FDTD analysis is used here to calculate the optical spectrum of a gold-graphene hybrid nanostructure in the Vis-NIR region. Fig. 4.1 shows the nature and details of a simulation model and geometry of the hybrid nanostructure under study. For each simulation, light is shined below the hybrid nanostructure to resonate the nanostructure, and then the spectrum (Extinction, Ext. = 1-(T+R)) is calculated using monitors at the top, the transmission (T), and at the bottom, reflection (R), of the device, Fig. 4.1a. A reflection monitor has been added

due to a significant amount of reflection, which is not the case in the Chp 2 and Chp 3 devices, and the extinction here is calculated as 1- (T+R). The transmission monitor is placed on top of the nanostructure 150 nm from the nanostructure-substrate interface, and coplanar with the source and reflection monitor, which are placed 150 nm and 250 nm below the nanostructure-substrate interface, respectively, as shown in Fig. 4.1a.

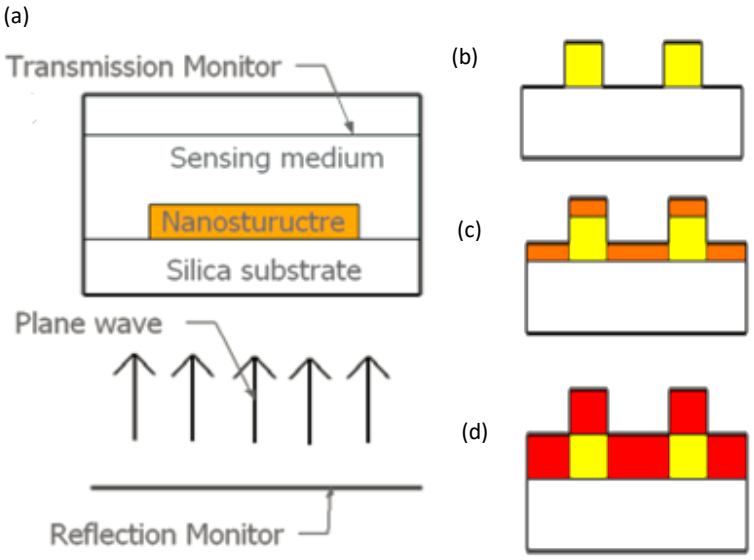

Figure 4.1: (a) Schematic illustration of numerical model. (b), (c), and (d) are the cross-section of Au NP array, gold-graphene hybrid nanostructure when graphene thickness is not equal and equal to Au ND heights, respectively.

The nano-device, source, and transmission/reflection monitors were co-planar with the boundary conditions. This made the device, source, and monitors infinite in the x and y directions. A non-polarized plane wave source (λ = 0.4 – 2 μm, electric field, E = 1V/m) was propagated along the z-axis normal to the device. In the x- and y- directions, anti-symmetric and symmetric boundary conditions respectively were chosen. In the z-axis, the perfect matching layer (PML)

boundary condition was applied. The point-to-point distance (mesh cell size) was 5 nm in the x and y directions, 0.3 nm in the z-direction. Air (n = 1) was chosen as the background.

In this work, three stages of simulation work take place: contribution of the hybrid nanostructure on plasmonic properties of the sensor, optimization, and finally performance evaluation. First, the effect of adding a graphene component to the gold nanostructure is studied by comparing the optical spectrum of a Au NP array with the gold-graphene nanostructure and monitoring the change in the plasmonic peak in terms of resonance position, intensity, and resonance bandwidth (FWHM). Two nanostructures are studied here: first is only Au NPs array and the second is the Au-G hybrid nanotecture. As shown in Fig. 4.1b, the first nanostructure is solely a Au nano-disk array with a fixed diameter (D) of 100 nm, fixed periodicity (P) of 300 nm, and height (H). The Au-G hybrid nanostructure, as shown in Fig. 4.1c, was formed by depositing graphene layers with thickness (t) on top of a Au NP array and between the NPs where the graphene thickness is not equal to gold ND height and, as in Fig. 4.1d, when graphene thickness is equal to ND height. The effect of graphene thickness (t) on plasmonic resonance intensity and FWHM of the resonance band were investigated. Finally, the nano hybrid structure that gives stronger resonance and sharper bandwidth (FWHM) was used to study sensor sensitivity and FOM. The sensing medium refractive index was changed from 1.333 to 1.349, with an index change of 0.001, 0.003, and 0.004.

4.3 Results and Discussion

The effect of hybrid graphene with metal NP on plasmonic sensor performance has been investigated in this work. At first, direct deposition of ~ three layers of graphene (t = 1 nm) on top

of Au ND arrays shows an apparent enhancement in the resonance extinction and FWHM of the resonance band in the NIR, as shown in Fig. 4.2a.

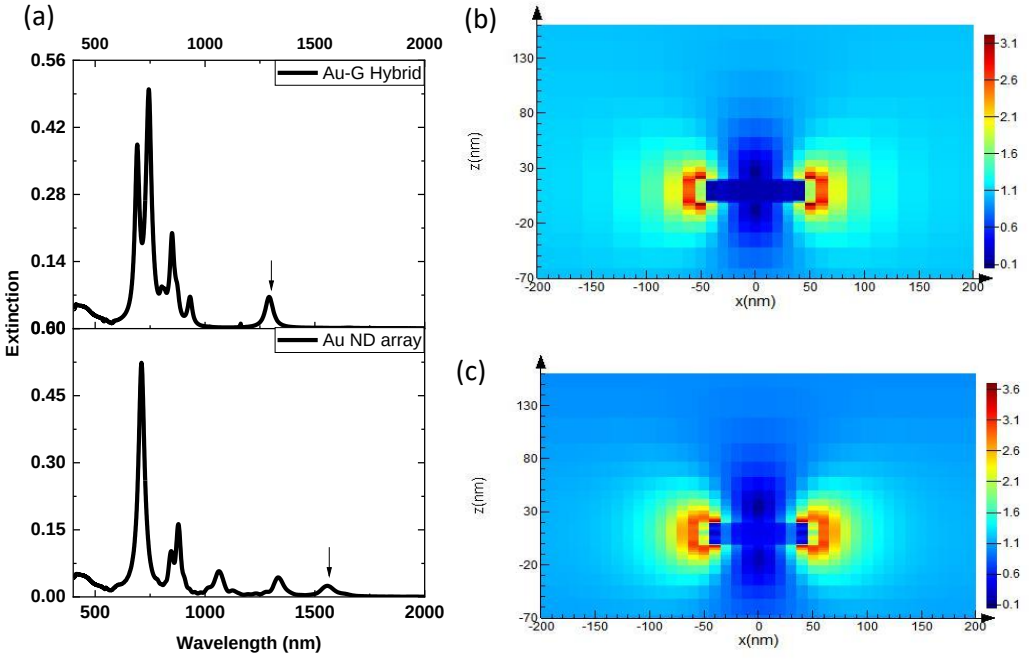

Figure 4.2: (a) Extinction spectrum of Au NPs array Au-G hybrid & electric field profile for the first resonance of (b) Au NP array (λ = 1557.8 nm), (c) Au-G hybrid nanostructure (λ = 1291.8 nm).

Considering the first resonance in a Au NP array (λ = 1557.8 nm) and Au-G hybrid nanostructure (λ = 1291.8 nm), there is a very significant enhancement in the extinction value of the first resonance by ~ 250 % after depositing graphene layers on top of and between the Au NDs in an array, where the value increased from 0.02 to 0.07. As reported by Sreejith and coworkers [70], an enhancement of >200% was observed in the absorption of Au-SiO_2 core-shell plasmonic resonance after GO coating. Using finite difference time domain (FDTD) analysis, they found through electric field distribution that enhancement is attributed to a combined absorption by Au and GO components. In addition, FDTD analysis as shown in Fig. 4.2b & c indicates an

enhancement in the electric field distribution after adding a graphene component into the gold nanostructure. The electric field in a hybrid nanostructure is enhanced by approximately 16 % compared to a Au ND array, which shows stronger localization of the plasmonic field. Additionally, there is a significant reduction in the FWHM of the resonances of the hybrid nanostructure compared to the Au ND array. The FWHM of the resonance at λ = 1557.8 nm reduced from 79.12 nm in the case of the Au ND array to 38.65 nm after adding the graphene component, which represents ~ 51% reduction in the FWHM and could be attributed to strong enhancement in the absorption band, as recorded in Chp. 2 for the core-shell structure. In addition to the effect of extinction on enhancing sensor performance, the FWHM of the resonance also has an apparent effect on sensor performance. According to equation 2.4 of the sensor's FOM based on the wavelength shift, as the FWHM decreases, the FOM of the sensor increases. Therefore, a reduction in the FWHM of these hybrid systems promises an enhancement in overall performance. A further optimization step has been taken by depositing a graphene film with a thickness equal to the Au ND height. Starting with depositing 20 nm thickness of graphene film on a Au ND array, Fig. 4.3 shows the extinction spectrum of the new hybrid scheme (i.e. graphene thickness = Au ND height) where a number of sharp (low FWHM) resonances in the NIR were obtained. For example, the resonance at λ = 1744 nm has a FWHM value of 8.29 nm. This is an indication of an immense improvement in sensor performance in terms of the FOM of the plasmonic sensor. Moreover, as reported [93], smaller nanoparticle size provides superior sensor performance; therefore, smaller hybrid nanostructure heights have been studied, which include 15, 10, 5 & 3 nm as shown in Fig. 4.3. In table 4.1, for each nanostructure height, the resonance with minimum FWHM is chosen and their values are tabulated. Data suggests that the hybrid nanostructure with

a height of 5 nm achieves the sharpest resonance, with a value of 1.9 nm. Therefore, this hybrid nano-device is chosen for sensitivity measurement.

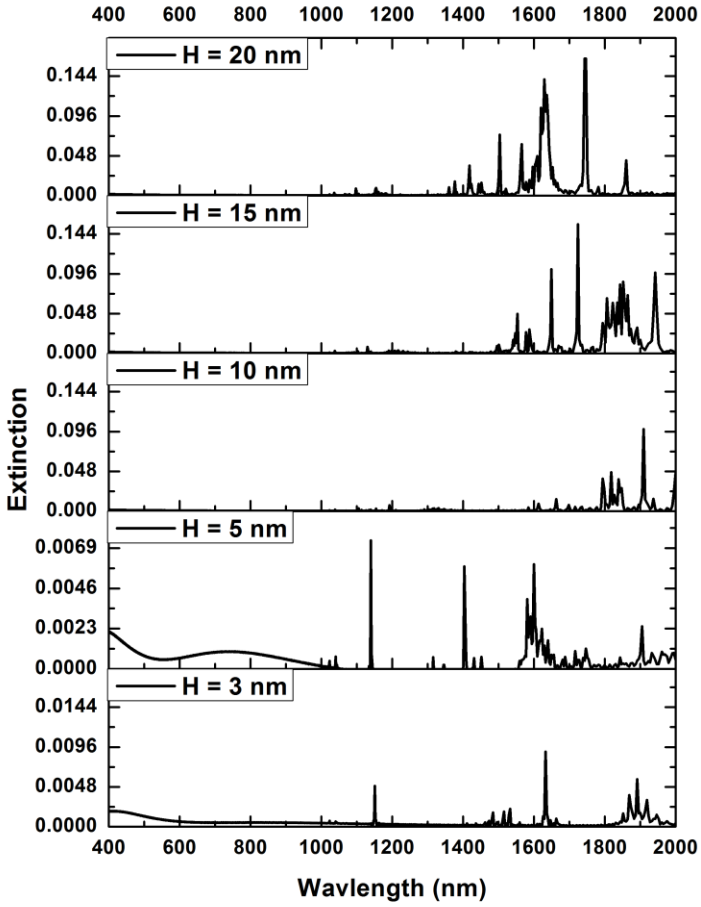

Figure 4.3: Extinction spectrum for Au-G hybrid nanostructure at different heights (H) where height of Au ND is equal to graphene film thickness.

Table 4.1: Resonances with highest value of extinction and their FWHM at different heights of Au-G hybrid nanostructure. Here, the height of Au ND is equal to graphene thickness.

Au-G NP height (h)	**Resonance wavelength (nm)**	**FWHM (nm)**
3	1632	4.79
5	1139	1.9
10	1909	6.31
15	1724	4.62
20	1744	8.29

To characterize sensor performance, the extinction spectrums of the new hybrid nanostructure with a Au ND height of 5 nm at a different refractive index of a sensing medium is calculated, and the shift in intensity and wavelength resonance peaks are monitored. The refractive indices used here are: 1.333, 1.334, 1.335, 1.336, 1.337, 1.338, 1.339, 1.34, 1.341, 1.342, 1.345, and 1.349, which involve refractive index changes (Δn) of 0.001, 0.003 and 0.004. As shown in Fig. 4.4, an intensity shift is present for each change in the refractive index, which illustrates the ability of the device to detect changes in the dielectric properties of the surrounding medium. The last two changes in the refractive index (1.342 to 1.345 and 1.345 to 1.349) show a higher intensity shift, attributed to a higher refractive index change (Δn) of 0.004. The FOM of the sensor depends on the sensitivity and reference intensity, and the sensitivity depends on the intensity shift and

refractive index change of the surrounding medium. Due to the complexity of the dependence of the sensor performance parameters, both sensitivity and FOM are calculated at every change in the refractive index. Three resonances, and all of these in the NIR region, are used to characterize the sensor's performance; $\lambda = 1139$ nm, $\lambda = 1403$ nm, and $\lambda = 1904$ nm. Equation 1.7 (Chp 1) is used here to calculate the sensitivity of the sensor based on an intensity-shift for each change in the sensing medium's refractive index. The results are plotted in Fig. 4.5. Though the last two refractive index changes show the highest intensity shift, the resonance at $\lambda = 1403$ nm results in the highest sensitivity when the refractive index changes from 1.333 to 1.334. This is because sensitivity depends on two factors: the shift extent and the degree of change in the refractive index. The high value of sensitivity of ~ 103 RIU^{-1} at $\lambda = 1403$ nm resonance is due to a lower refractive index change ($\Delta n = 0.001$). Furthermore, the FOM of the sensor, based on the intensity shift, is calculated using Eq. 1.9, and the results are shown in Fig. 4.6. The maximum FOM observed here is 232.6 at $\lambda = 1139$ nm when the refractive index changes from 1.336 to 1.337. As noted, the highest FOM is not observed in the case of highest sensitivity. This is possible where the FOM depends on reference intensity in addition to the sensitivity. This means that not all high sensitivity values should lead to high FOM values.

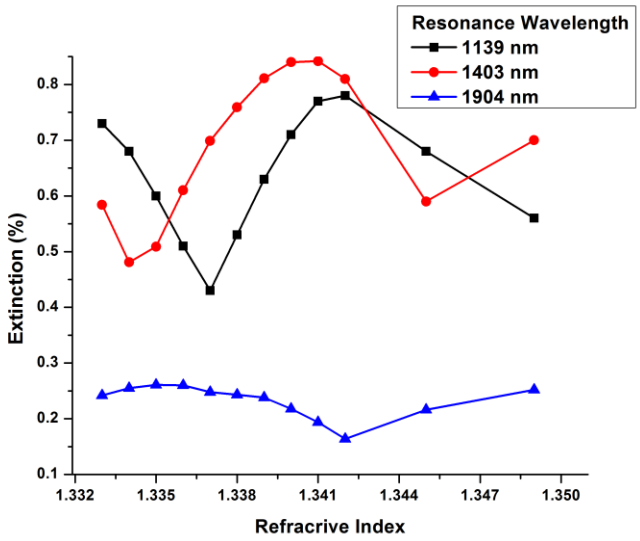

Figure 4.4: Intensity shift as the refractive index of the sensing medium changes at different resonances of Au-G hybrid nanostructure where the height of Au ND (H = 5 nm) is equal to graphene thickness.

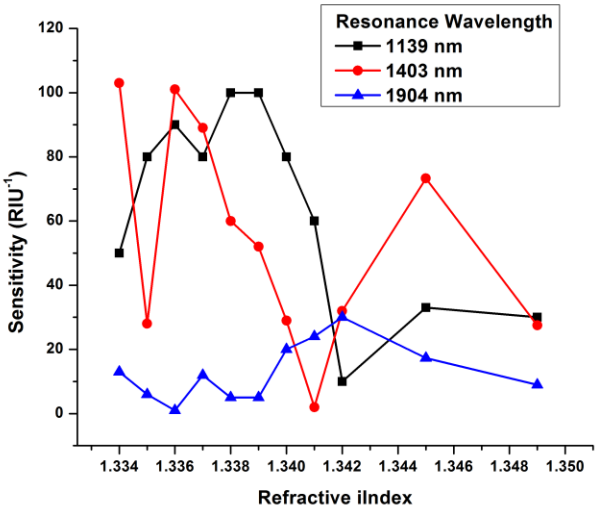

Figure 4.5: Sensitivity of Au-G hybrid nanostructure based on intensity shift at different resonances where the height of Au ND (H = 5 nm) is equal to graphene thickness.

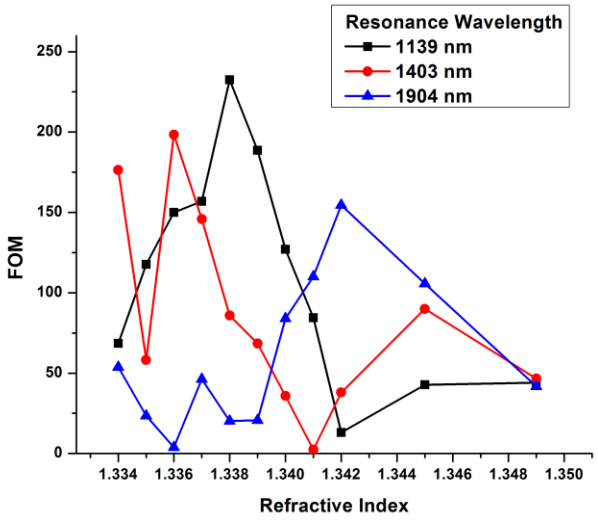

Figure 4.6: FOM of Au-G hybrid nanostructure based on intensity shift at different resonances where the height of Au ND (H = 5 nm) is equal to graphene thickness.

On the other hand, wavelength resonance peak shifts are observed, but only at some refractive index changes, as summarized in Table 4.2. A maximum sensitivity of 2460 nm/RIU is observed at, λ = 1403 nm when the refractive index changes from 1.334 to 1.335, and a maximum FOM of 857.9 is observed at λ = 1139 nm when the refractive index changes from 1.336 to 1.337. In the case of calculating sensor performance based on wavelength shift, both the amount of resonance shift and FWHM affect the sensitivity and FOM of the sensor. Thus, a similar scenario to the sensitivity and FOM based on intensity shift is observed here as well, where a maximum FOM condition is not observed for the same case of maximum sensitivity. The high sensitivity at λ = 1403 nm is due to a higher wavelength shift ($\Delta\lambda$ = 2.46 nm) compared to resonance at λ = 1139 nm ($\Delta\lambda$ = 1.63). In addition, the high FOM observed in resonance at λ = 1139 nm is due to lower FWHM (1.63 nm) compared to resonance at λ = 1403 nm (4.4 nm).

Table 4.2: Sensitivity and FOM of Au-G hybrid nanostructure, based on resonance wavelength shift, where the height of Au ND (H = 5 nm) is equal to graphene thickness.

	λ (nm)	FWHM (nm)	RI range (Δn)	λ shift (nm)	S (nm/RIU)	FOM
Res1	1139	1.9	1.336 – 1.337 (0.001)	1.63	1630	857.9
			1.345 – 1.349 (0.004)	1.63	407.5	214.5
Res 2	1403	4.4	1.334 – 1.335 (0.001)	2.46	2460	559.1
			1.345 – 1.349 (0.004)	2.48	620	140
Res 3	1904	7.8	1.341 – 1.342 (0.001)	2.09	2090	267.9
			1.342 – 1.345 (0.003)	2.5	833.3	106.8

Results of the LSPR sensor performance studied here, using gold-graphene hybrid nanostructure, showed outstanding values in the field of the localized surface plasmonic sensor. In addition, the highest sensitivity and FOM, either based on intensity or wavelength shift, are observed at a very low refractive index change, $\Delta n = 0.001$, which demonstrates an ability of the sensor to detect low liquid concentration changes. This is helpful, for example, in early cancer detection diagnosis in bio-applications.

According to Yang et al., a gold mushroom NP array plasmonic device registered a detection limit of 10 ng/ml of Alpha-fetoprotein (AFP) protein, which is a biomarker for hepatocellular carcinoma cancer, and detecting smaller concentrations helps to diagnosis this cancer at an early stage [91]. In the work of Yang et al., the refractive index change was in the range of 0.01, while in this study it was 0.001. Detecting a smaller change in the refractive index indicates the sensor's capability to detect smaller concentration change and thus the proposed sensor in this study, as demonstrated by its competitive performance, can achieve a low-detection limit and be a promising platform in bio-sensing technology.

Furthermore, gold and graphene deposition (using E-beam evaporator and chemical vapor deposition techniques), and metal milling using focused ion beam (FIB), are extensively published in the literature, and these are the main steps required to fabricate the hybrid nano-devices studied here. Growing a Au ND array on top of a quartz substrate can be performed by depositing gold film using an E-beam evaporator, and then direct milling of Au film using FIB method that is preferred to E-beam lithography due to the fewer fabrication steps required for patterning a Au NP array, maskless and high resolution nanofabrication technique [76,84]. The hybrid nanostructure

is then fabricated by direct deposition of a graphene film on a Au NP array using the CVD method. However, using a conventional CVD process can cause damage to Au NPs due to a high deposition temperature that may reach 1000 ^{o}C. For this reason, low temperature graphene deposition is essential to avoid Au NP diffusion into the substrate. Recently, Fujita et al. developed a new CVD graphene growth method at low temperature, as low as 50 -100 ^{o}C [94]. Using their method, graphene nuclei can build up between Au NPs and on top of Au NPs; however, the portion on top of Au NPs may result in slightly rounded edges, not exactly sharp as in the simulated model studied here. Generally, the overall simplicity and few fabrication steps required for fabricating the proposed nanostructure makes it a very competitive platform for an upcoming plasmonic sensor based on localized plasmons.

4.4 Conclusion

In this chapter, plasmonic properties of gold-graphene hybrid nanostructure grown by direct deposition of graphene film on top of a Au ND array have been investigated numerically using the FDTD method. It was observed here that adding graphene layers to the metal component in a plasmonic device enhances absorption of the gold nanostructure, which is a preferred property in designing a plasmonic sensor. Optimizing graphene film thickness shows outstanding improvement in plasmonic resonance in terms of a sharper band obtained, where FWHM reaches as low as 1.9 nm. This immense reduction in the FWHM yields a FOM equal to 857.9, which so far has never been cited in the literature, to the best of the author's knowledge. Furthermore, this high FOM value is observed at a refractive index change on the order of 0.001, which represents a very low change of concentration of analyte in bio-applications. Moreover, the hybrid

nanostructure studied here can be fabricated in three well known steps: deposition of gold film, milling with use of FIB to produce a Au ND array, and finally, deposition of graphene using, for example, the CVD method. The simplicity and feasibility of this gold-graphene hybrid nanostructure and its significant improvement in sensitivity and FOM make it a promising platform nanostructure for most plasmonic sensor applications in addition to enhancing its commerciality.

Chapter 5 Promoting Localized Surface Plasmonic Resonance Sensor Performance via Spin-Coating Graphene Flakes over Au Nanodisk Array[4]

In this chapter, a new and simple gold-graphene hybrid scheme is proposed, and its plasmonic sensing performance is numerically evaluated using the finite different time domain (FDTD) method. The proposed sensor can be developed by growing a Au nano-disk (ND) array on a quartz substrate and then spin-coating graphene flakes of different sizes and shapes randomly on top of and between the Au NDs. A very high sensitivity value is achieved: 2262 nm/RIU. The obtained sensitivity value is very competitive in the field of LSPR sensors using a metal-2D hybrid nanostructure. This proposed sensor can be utilized in different biosensing applications such as in immunosensors, DNA hybridization sensing, and early disease detection, as discussed at the end of this chapter.

[4] This is an Accepted Manuscript of an article published by Alharbi, R. & Yavuz, M. in Photonics on 25 May 2019, available online https://www.mdpi.com/2304-6732/6/2/57 [Article DOI : 10.3390/photonics6020057]. "Promote Localized Surface Plasmonic Sensor Performance via Spin-Coating Graphene Flakes over Au Nano-Disk Array"

5.1 Introduction

From an engineering point of view, the optimum choice is to design a device with high performance, low cost, and good reproducibility. As known, the main issue with the LSPR sensor is its performance, and higher performances are achievable either in a simple or complex hybrid scheme. In addition to a continuous sheet of graphene, as studied in Chapters 2, 3, and 4, graphene also is available in flake form in solution with a broad range of sizes and different anisotropic shapes. Thus, hybrid gold nanostructure with graphene flakes is another possible way to improve LSPR sensor performance. By studying the effect of randomly spin-coating graphene flakes on top of and between the gold NDs array on the sensing performance, the question of whether LSPR sensor performance can be improved using graphene flakes could be answered. This proposed hybrid scheme can be fabricated through only three main fabrication steps: starting with gold film deposition, followed by direct metal milling using a focused ion beam technique to grow a Au ND array, and lastly spin-coating graphene solution using a spin coater. These fabrication steps are well studied in the literature and provide good controllability, as reported elsewhere [95,96]. Having few and controllable fabrication steps is the advantage of this proposed sensor and its high-sensing performance is the goal of this work. In the following sections, the method used to conduct this research, the obtained results, and applications of the sensors are discussed. Finally, some considerations for further optimization work are discussed, followed by the conclusion.

5.2 Methodology

This study was performed using the finite difference time domain (FDTD) method to calculate the light absorption spectra of the Au-G hybrid nanostructure placed on top of quartz substrate, as shown in Fig. 5.1a. Fig. 5.1b shows a 3D view with only three graphene flakes, Fig. 5.1c shows a 3D view with the entire number of graphene flakes (10 flakes) and Fig. 5.1c shows a cross-section of one unit of the Au-G hybrid nanostructure that is repeated periodically in the x and y directions. The hybrid nanostructure involves a Au ND (diameter = 100 nm, height = 20 nm) array with periodicity of 300 nm placed on the substrate, and then graphene flakes of different shapes and sizes (rod (50 × 300 nm), square (100 × 100 nm), and rectangle (100 × 300 nm)) are placed randomly on top and between Au NDs as shown in Fig. 5.1b & c. The thickness of the graphene flakes is assumed as 1 nm. The assumption is that graphene flakes in solution do not come in similar shapes or sizes. In fact, graphene flakes are available in a very wide range of shapes and sizes; however, assumptions of the shapes and sizes of graphene flakes here are simplified, and the study is merely to explore the possibility of enhancing LSPR sensor performance through spin-coating graphene flakes of different shapes and sizes randomly around the Au ND array.

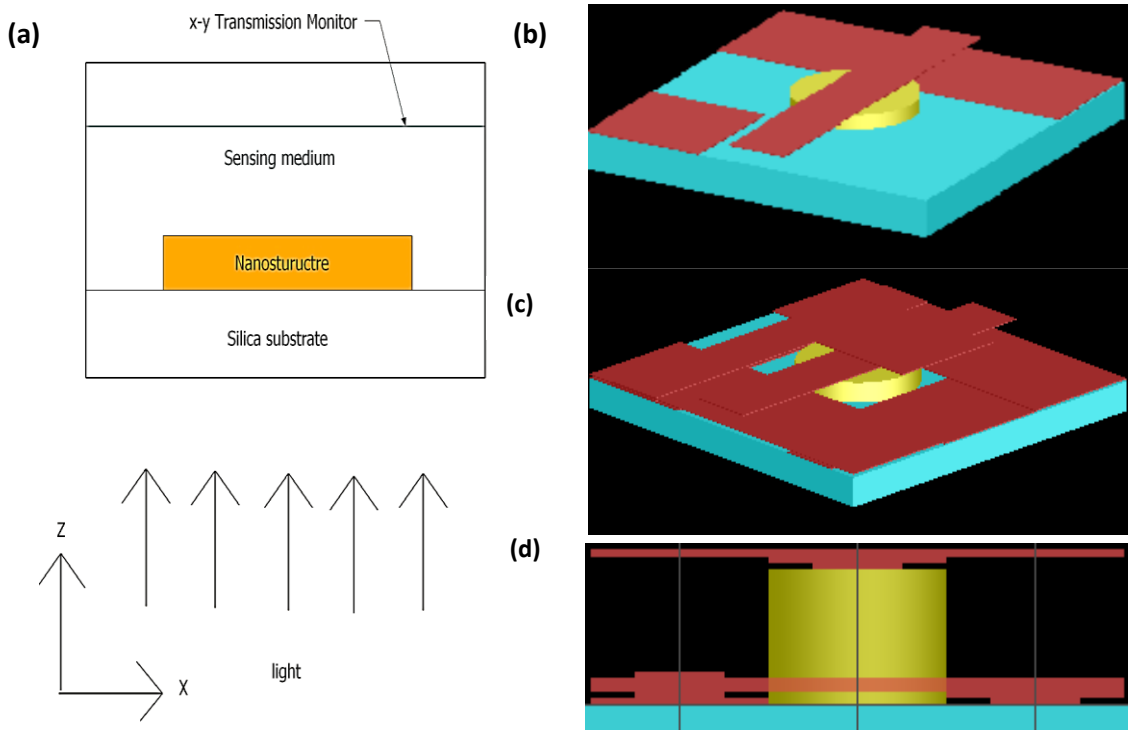

Figure 5.1: Schematic representation of the simulation model (a), 3D view (3 G flakes) (b), 3D view (10 G flakes) (c), and cross-section view (d) of the Au nano-disk (ND)- graphene (G) flakes hybrid nanostructure.

A commercial software package (Lumerical FDTD Solutions) is used to conduct the numerical analysis. All Au ND-G flake hybrid nanostructures, transmission monitor, and plane wave source are co-planned with boundary conditions that make them infinite in the x- and y directions. Herein, as shown in Fig. 5.1a, the nanostructure is illuminated from the bottom by an unpolarized plane electromagnetic wave that is used as a light source. The electromagnetic wave propagates in the z-axis (as labeled by arrows in Fig. 5.1a) in the wavelength range of 0.4 to 2 μm, with electric field amplitude of 1 V/m. Anti-symmetric and symmetric boundary conditions are used on the x- and y-axes, respectively, and a perfectly matched layer boundary condition is used on the z-axis. The mesh cell-size is very small (0.035 nm point-to-point distance) in the z direction,

to ensure that adequate resolution is achieved due to the presence of graphene flakes with a thickness of 1 nm. On the x- and y-axes, the mesh cell size is 5 nm. The source is placed 150 nm below the substrate-Au ND interface, and to calculate absorption spectra, an x-y monitor is placed 150 nm above the Au ND-substrate interface. Another x-z monitor is used to calculate the cross-section electric field profile of the nanodevice. Air (n = 1) is chosen as the sensing medium for sensing measurement[5].

In this work, the effect of graphene flakes placed randomly on top of and between Au NDs in an array is studied by comparing the absorption spectra of Au ND arrays with Au ND-G flakes hybrid nanostructures, where all the size and shape parameters of both Au ND and G flakes are fixed. The sensitivity of the hybrid device is then measured by monitoring the shift in resonance wavelength, as the refractive index of the sensing medium changed from 1 to 1.04 with 0.01 steps. The sensitivity of the sensor is assessed by measuring the ratio of wavelength resonance shift to refractive index change. Further optimization suggestions and pertinent applications for the proposed sensor are discussed below.

5.3 Results and Discussion

The absorption spectra of Au ND arrays placed on top of quartz substrate are calculated in the wavelength range of 400–2000 nm (Fig. 5.2a). Then a number of graphene flakes with different shapes and sizes are distributed around the Au NDs to a total thickness of 5 nm (each flake thickness = 1 nm), and only three flakes (total thickness of flakes = 3 nm) are placed on top of the

[5] Air was chosen here due to the lab availability during simulation work of this sensor as presented in Chp 6. Near field spectroscopy system use air as background medium not liquid. However, the sensing mechanism is the same, measuring the shift in the plasmon resonance upon change in surrounding's refractive index.

Au ND as shown in Fig. 5.1b. The absorption spectra for the Au ND-G flake's hybrid nanostructure is then calculated and compared with spectra of Au NDs only, as shown in Fig. 5.2a.

Absorption spectra of Au ND arrays show strong resonances in the visible region (at $\lambda = 642.4$ nm) which could be attributed to the intrinsic absorption property of gold, and the redshift is due to the geometrical dependence of the Au ND [97]; other resonances may be attributed to different LSPR modes [98]. After the addition of G flakes, changes occur in resonance intensity and wavelength, and other new resonances are created. In the visible region, no enhancement in absorption is recorded, while it is present in longer wavelength resonances (resonances between 750–1100 nm). In addition, no apparent shift in the resonance's wavelength is present after spin-coating graphene flakes, while it is clearly observed in longer wavelength resonances. The more interesting observation is the finding of new resonances in the region of ~1100–2000 nm where there are no resonances recorded for Au ND arrays. The two resonances observed here are: a sharp one at 1203.81 nm and a broad one at 1882.28 nm. These two resonances result from the coupling of Au and graphene flake resonances as shown in the electric field profile, Fig. 5.2b, c at $\lambda =$ 1203.81 nm. Fig. 5.2b illustrates the cross-sectional electric field profile for Au ND while Fig. 5.2c shows the profile for Au ND-G flakes hybrid nanostructure. There is ~200% enhancement in the electric field after addition of graphene flakes on top of Au NDs at $\lambda = 1203.81$ nm. The observed enhancement is due to strong localization of the field, which is clearly observed at the bottom side (right and left) of the Au ND. Enhancement in the electric field after adding the graphene component agrees with what is reported by Sreejith and coworkers [70]. Using FDTD, they observed an enhancement in the electric field around Au NPs after coating with graphene, which is attributed to a combined absorption by gold and graphene at the same resonance

wavelength, which is explained in their experimental results, where after coating gold NPs with graphene, apparent absorption enhancement was recorded.

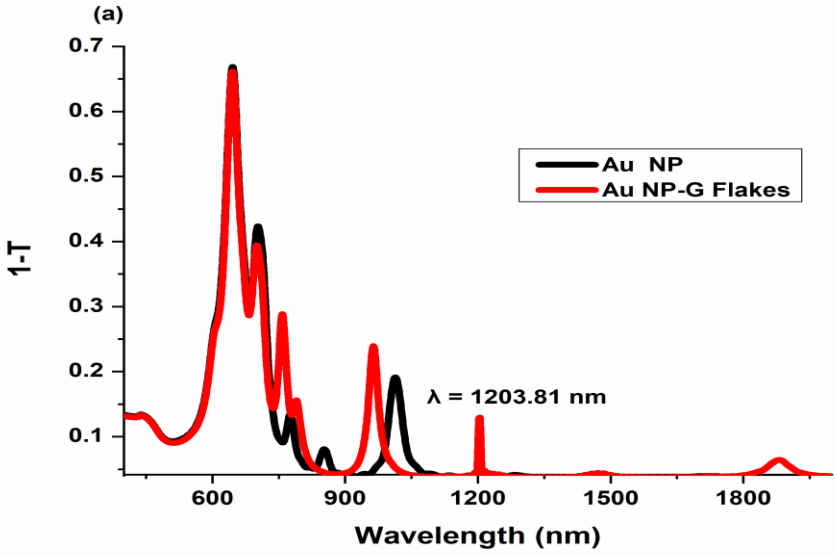

(**a**)

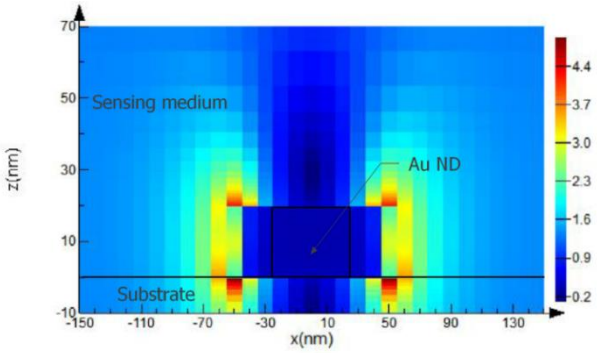

(**b**)

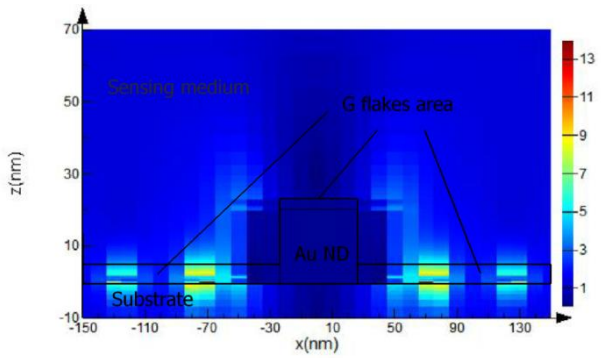

(**c**)

Figure 5.2: Absorption spectra of Au ND array and Au-G flakes hybrid nanostructure (a), and the cross section (x-z axis) electric field profile of Au ND array (b) and Au-G hybrid nanostructure (c) at λ = 1203.81 nm.

Sensor performance (sensitivity and FOM) was measured by changing the refractive index of the sensing medium and monitoring the shift in resonance modes A and B, Fig. 5.3. The sensitivity of the sensor is calculated using Equation (1.1). The refractive index of the sensing medium increased from 1 to 1.04 with 0.01 steps. Fig. 5.3 represents the spectra of the gold-graphene flakes hybrid nanostructure at different refractive indices, and clearly shows a resonance shift in wavelength for all resonances in the spectrum. The shift in the resonance can be explained by Mie scattering, where as permittivity of the medium of NP proximity changes, the resonance changes linearly [99]. Equation 5.1 below shows the relation between the resonance wavelength and permittivity of the sensing medium, and explains the reason why the resonance is redshifted upon increasing permittivity of the surrounding medium.

$$\omega_{LSP} = \frac{\omega_p}{\sqrt{1+2\varepsilon_d}} \qquad 5.1$$

In equation 5.1, ω_p is the plasma frequency of the gold and ε_d is the permittivity of surrounding medium.

As shown in Fig. 5.3, mode A redshifted from 1203.81 nm to 1217.35 nm when the refractive index of the sensing medium increased from 1 to 1.04.

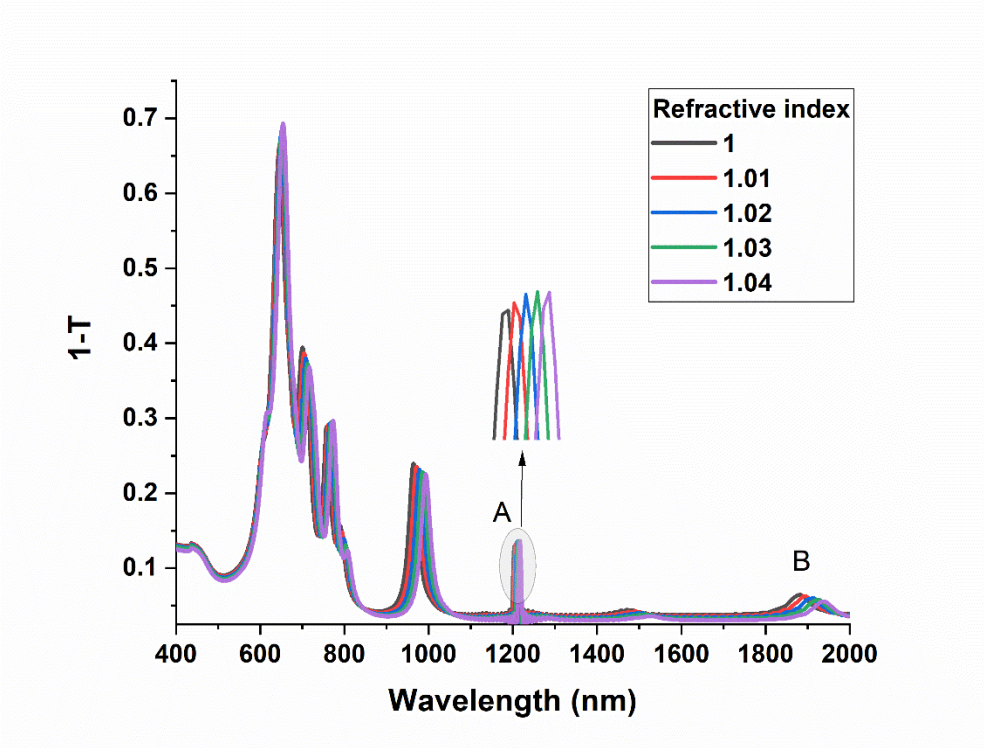

Figure 5.3: Absorption spectra of Au ND-G flakes hybrid nanostructure at different values of refractive index of sensing medium.

Multispectral properties (different plasmonic modes) of this proposed sensor, as shown in Fig. 5.3, can improve the sensor's performance compared to devices with only one resonance mode. From Fig. 5.4, it is clearly shown how the plasmonic resonance modes A and B shift when the refractive index of the sensing medium increases from 1 to 1.04 at the same refractive index change. Resonance mode B exhibits a larger shift by an amount of ~ 8.9 nm compared to lower resonance mode A, that shifted by an amount of ~2.6 nm. This leads to different sensitivities for

different plasmonic resonance modes of the same sensor. Therefore, a multispectral sensor can provide different levels of sensitivity at the same refractive index changes.

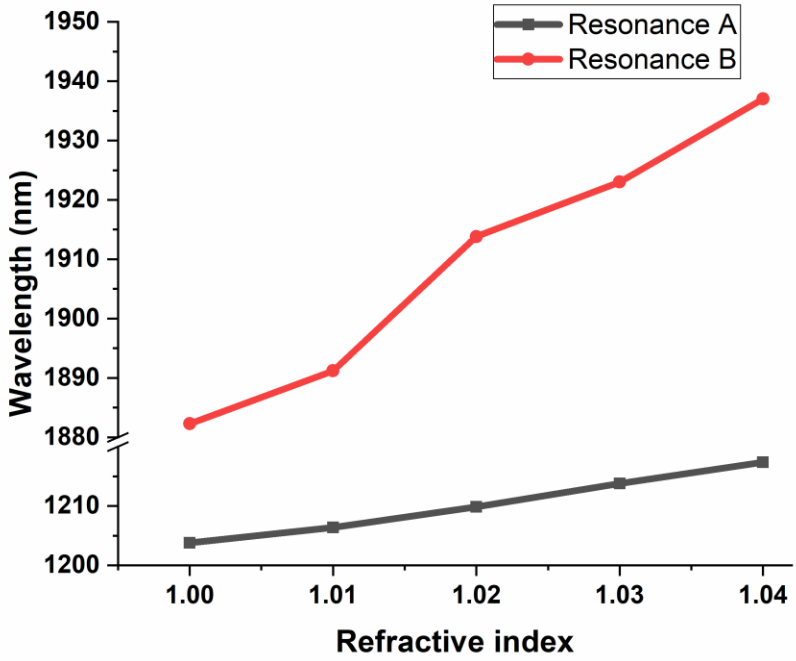

Figure 5.4: Resonances A and B shifts vs. refractive index change.

As mentioned, longer wavelengths exhibit greater resonance shift, and thus higher sensitivity results as shown in Fig. 5.5. The resonance mode A at λ = 1203.81 nm demonstrates a shift of approximately 3 nm for each change in the refractive index, and maximum sensitivity of 457 nm/RIU results when the refractive index of the sensing medium is changed from 1.03 to 1.04. However, resonance B at λ = 1882.28 shows larger shifts for refractive index changes, and maximum sensitivity is recorded for resonance B at 2262 nm/RIU when the refractive index is changed from 1.01 to 1.02, where the resonance shift is approximately 21 nm. Larger shifts in the longer wavelength resonance modes agree with what is reported in the literature, such as Bukasov et al. [85].

The figures of merit for both resonances A and B were calculated. The FWHM for resonance A is 6.5 nm and results in a FOM of 70.3 while for resonance B, the wide resonance peak width with a FWHM of 54.9 nm yields a FOM of 41.2. As reported by Paramelle et al. [22], the broadening in resonance B could be attributed to an increase in the scattering and thus negatively affect the FOM of the sensor. Though resonance B is associated with higher sensitivity, an increase in the FWHM of the resonance band results in ~40 % reduction in the FOM compared to resonance mode A. Thus, mode A shows a better detection limit than mode B due to higher FOM; moreover, in terms of sensitivity, mode B is more enhanced, and further optimization in the structure aimed at reducing linewidth of resonance B could enhance its FOM. The gold-graphene core-shell hybrid NP array studied earlier (Chapter 2), shows 350 nm/RIU sensitivity and 102.6 FOM. The sensor undertaken in this nanostructure shows more than a 6-fold enhancement in sensitivity and ~ 40% reduction in the FOM using mode B compared to core-shell structure. Thus, enhancing resonance B by reducing its FWHM by further optimization, gives this sensor another advantage in addition to simplicity in fabrication, compared to core-shell structures.

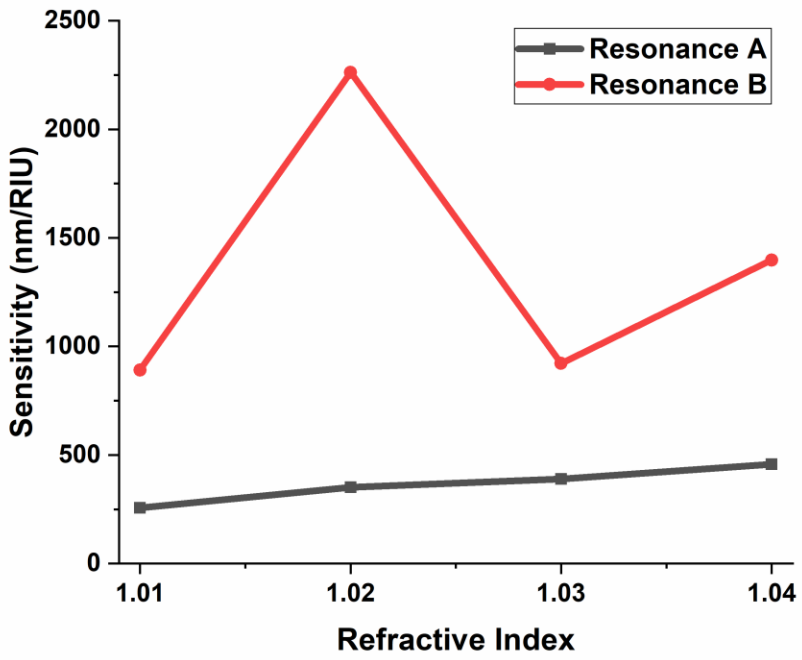

Figure 5.5: Sensitivity of resonance modes A and B as the refractive index changes.

The proposed gold-graphene hybrid nano-device shows competitive sensing performance in the LSPR sensor field, in addition to its ease of fabrication and controllability in comparison to those sensors that include continuous graphene film. The sensor discussed in this research can be manufactured through three main steps using commercially manufactured graphene solutions [100,101]. The first step is gold film deposition, followed by direct-milling, using well-known and widely used focused ion beam (FIB) technology [84]. Finally, graphene solution is spin-coated using a spin-coater on top of the fabricated Au ND array. Significant improvement in sensing performance is observed numerically here; the simplicity and controllability of the proposed nanostructure make this sensor superior for a number of applications, and thus enhance the commerciality of LSPR sensors.

The sensing mechanism in SPR sensors is based on resonance angle shift due to refractive index change in the sensing medium. There is a similar scenario in LSPR sensors, but instead of shift in resonance angle, there will be a shift in resonance wavelength or resonance intensity. Therefore, any application using SPR sensors could be performed using LSPR sensors with different sensing mechanisms. LSPR sensors can be used as immunosensors that are able to detect human growth hormone (hGH) in real serum samples. Makaraviciute et al. studied the application of SPR immunosensors using the protein G based site-directed antibody capture technique (where protein G is a commonly used affinity capture reagent [102]). Addressing direct repeated real sample measurements [103], Makaraviciute et al. performed an immobilization technique on top of gold film. This can also be performed on top of the Au ND-G flakes hybrid nanostructure studied here, and the shift in resonance wavelength or intensity can be monitored after capturing monitored hGH. Furthermore, the SPR sensors show fairly good applicability in detecting DNA hybridization [104] and in early cancer detection [105]. Thus, immobilization and functionalization of Au ND-G flakes nanostructure instead of Au film as in SPR sensors, make the proposed LSPR sensor studied here a good platform for biomolecular interaction detection that is helpful in detecting cancer diseases in early stages. However, one point to be considered during application is the adhering of graphene flakes onto substrate and Au NP. Enhancing adherence through thermal annealing as reported [106], could be applied and may prevent washing away of graphene flakes during application of fluids in sensing experiments.

So far, the results of the proposed device are merely to prove that by spin-coating graphene flakes randomly on top of and between Au NDs in an array, the sensing performance of the LSPR sensors can be improved. However, there are several points that need to be considered for further

optimization of these sensors at the fabrication stage. The size, shape, and periodicity of Au NPs are effective parameters used to optimize sensing performance. Furthermore, the size, shape, and thickness of graphene flakes are also effective optimization parameters that can be included in an apparent rule of optimization. For example, according to a previous study (Chp 3) of gold graphene core-shell hybrid NPs, increased thickness of graphene could enhance the resonance intensity and thus sensor performance. Therefore, increasing graphene flake thickness is one of the further optimization steps for the proposed sensor. Moreover, at the fabrication stage, both the periodicity of the Au NPs and dimensions of graphene flakes should be carefully considered. In this work, the graphene flake dimensions are in the range of 100s nm, and periodicity of the gold NP array is 300 nm. It is, therefore, possible that graphene flakes can be inserted between gold NPs, and this insertion will enhance interaction with light through increasing absorption. If the graphene flakes are larger than their periodicity, the effect of hybridizing may not give the expected results shown here. Therefore, optimizing periodicity according to the dimensions of the produced graphene flakes is important to ensure better results in sensor sensitivity. In this study, the total size of graphene flakes is kept constant (fixed number of flakes) and incorporating more graphene flakes could enhance the absorption of the sensors and may result in better sensing performance.

5.4 Conclusion

The production of highly sensitive LSPR sensors via simple and more controllable nanostructure manufacturing is the goal of this study. This work explores the effect of spin-coated graphene flakes on a periodic gold ND array on LSPR sensing performance. This research is conducted numerically using the FDTD method. By calculating the absorption spectra of the hybrid

nanostructure at different refractive indices of the sensing medium, the resonance shift is clearly observed (mode A: λ = 1203.81 nm & mode B: λ = 1882.28) and are used to assess the sensor's performance. The maximum sensitivity achieved is 2262 nm/RIU at mode B when the refractive index is changed from 1.01 to 1.03. This proposed gold-graphene hybrid sensor proves that an LSPR sensor can be optimized to a competitive performance value through a simple and readily controllable fabrication method. The proposed sensor can be fabricated through three simple and well-known techniques: Au film deposition, metal milling using FIB technology, and spin-coating graphene flakes. Further optimization for this hybrid nanostructure could be performed based on the geometrical properties of both Au NPs and graphene flakes, Au NP array periodicity, and the total size of graphene flakes.

Chapter 6 Optical Near Field Characterization of Au NP Array for Localized Surface Plasmon Resonance (LSPR) Sensing[6]

In this chapter, optical near-field characterization for the fabricated Au NP array grown on quartz substrate was performed using scanning near-field optical microscopy. The light-gold NP interaction was studied, and the intensity profile of the excited NPs was measured. Then, finite difference time domain (FDTD) method was applied for a fabricated device to study the applicability of the device in LSPR sensing. The results showed that the intensity profile of the excited gold NPs can be used for sensing purposes, as confirmed numerically via simulation work.

[6] This is a submitted Manuscript of an article by Raed Alharbi, Victor Wong, Abdullah H. Alshehri, Giovanni Fanchini, and Mustafa Yavuz in [Ann Phys, Wiley-VCH,.] on [Oct. 2019] "Scanning near-field optical microscopy assisted design of sensing enhancement devices based on localized surface plasmon resonance"

6.1 Introduction

As demonstrated in Chapters 2 to 5, hybrid Au NPs with graphene presented significant enhancement in the localized plasmon field and resulted in significant improvement in LSPR sensor performance. However, this localized field enhancement is recorded in the nanoparticle proximity (~ few 10s nm), and therefore, super-resolution microscopies, such as scanning near-field optical microscopy (SNOM), are required to probe the optical response of nanoscale objects in the near field regime. With SNOM, the light-matter interaction in the near-field regime can be characterized. Using SNOM, aluminum bowtie nano antennas, Au nanoparticles with sizes lower than 100 nm, were imaged as reported [107]. Furthermore, as reported by Dhara & Sivadsive, Au NPs with sizes ranging from 10 – 150 nm are imaged using the SNOM technique [107]. At 532 nm excitation, they observed strong resonance of Au NPs (which is spectrally located at 535 nm) and their results were consistent with the visible transmission spectra of this system [107]. Ezugwu et al. performed a 3D-SNOM image of random arrays of Cu NPs and measured the intensity of the wave that resulted from constructive and destructive interference between the Cu NPs, which represents the intensity profile at a selected region of Cu NPs [108]. This intensity profile is the key tool that can be used for sensing purposes.

Here, Au NP arrays have been fabricated using focused ion beam (FIB) technology, and their light-scattering response has been characterized using the SNOM technique that enables the reconstruction in 3D of the near-field on top of specific plasmonic nanostructures. The intensity profile of Au NP arrays in air as the surrounding medium is experimentally measured, and their intensity profiles as the refractive index changes from 1 to 1.005, with 0.001 steps, were

theoretically calculated using the FDTD method. Studying the intensity profile of the nanostructure at different refractive index values of the surrounding medium shows the ability of the 3D-SNOM technique to be used for plasmonic sensing applications. In this chapter, details of fabrication and characterization are followed by discussion of obtained results, and then conclusions and further work are presented.

6.2 Methodology

The gold NP array was fabricated via direct milling using focused ion beam (FIB) technology. At first, the silica (quartz) wafer (25.4 mm in diameter, 1.6 mm thick) was cleaned by washing it with IPA, acetone, and DI water, and finally dried with nitrogen gas. The Intlvac Nanochrome E-beam evaporation system (EBV) was used to deposit 3 nm Cr as an adhesion layer between the 20 nm of gold film and silica substrate. The deposition was performed in a vacuum chamber with a base pressure of 4×10^{-6} Torr and deposition temperature of 42 ^{o}C at a rate of 0.5 A/s. Next, a FILMETRICS F40-UV thin film analyzer was used to measure the film thickness. For patterning the Au NP array, a Zeiss Auriga FIB-SEM system was used to direct mill the gold film. Basically, the FIB system sent Ga ions to a selected area and removed sputtered Au ions where 20 x 20 Au NPs with a periodicity of 200 nm had been fabricated. Immediately after the milling process, the fabricated nanostructure images were taken using the SEM system equipped with an FIB system. Next, the D3500 Nanoman atomic force microscope (AFM) was used to measure the NPs' height or depth of milling. A Witec Alpha 300S SNOM microscope was then used to study the optical interaction of excited Au NPs with plane waves at 532 nm, using the collection-transmission mode configuration shown in Fig. 6.1a. The 532 nm excitation wavelength corresponds to the reported SPR resonance of gold, which is in the range of 500 – 550 nm [107]. SNOM experimental details, including the description of the experimental setup, are available elsewhere [108]. In brief, a 532

nm laser beam is launched, and light is scattered by the sample collected in the near-field region. A contact-mode x-y SNOM scan is performed at z = 0, along with an AFM image. Then, Y-Z scans are performed above the sample, which enables the collection in the near-field of light scattered at z > 0.

To examine how to utilize the SNOM technique for plasmonic sensing, the intensity profiles of Au NP arrays at different refractive index values of surrounding medium were calculated by applying the finite difference time domain (FDTD) method using the Lumerical FDTD package. Fig. 6.1b shows the schematic illustration of the model used for simulation work in which the laser excited the region below the nanostructure, and two monitors were used. The first one is an x-y monitor to obtain the electric field profile and relative intensity profile of the whole Au NP array, while the x-z monitor is used to obtain the electric field profile of the cross-section of Au NPs. The optical constants of gold are calculated using the Drude-Lorentz model [66] over a specified wavelength, and are n = 0.39 and k = 2.11 at 532 nm. A non-polarized plane wave source (λ = 532 nm, electric field, E = 1V/m) was propagated along the z-axis normal to the nanostructure. The perfect matching layer (PML) boundary condition was applied in x, y, & z-axes. The point-to-point distance (mesh cell size) was 5 nm in the x- and y-directions, 1 nm in the z-direction. Air (n = 1) was chosen as the background.

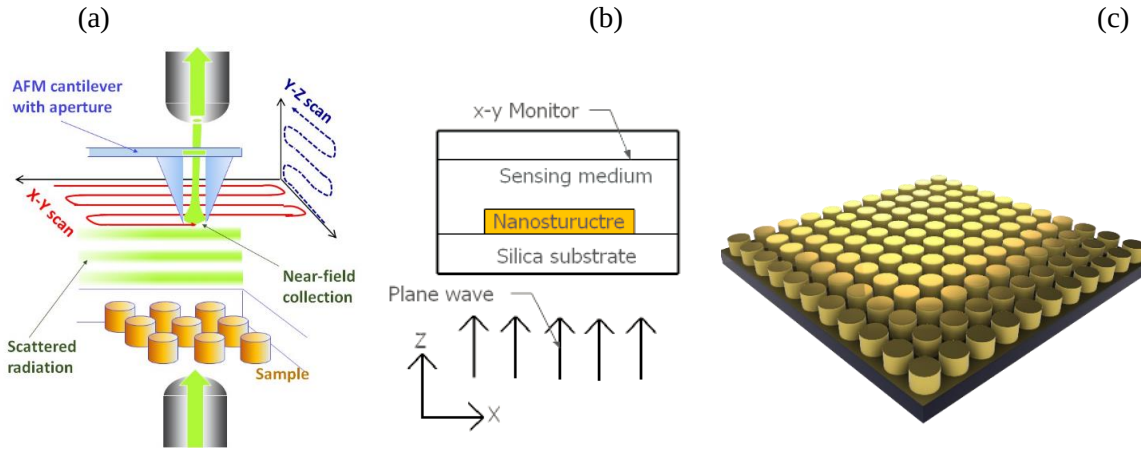

Figure 6.1: Schematic illustration of the transmission-collection 3D-SNOM configuration used to acquire the experimental data (a), model used in the simulation work (b) corresponding to the experimental configuration used in panel (a), and schematic illustration of Au ND array (c).

6.3 Results and Discussion

In this work, Au nano-disc arrays using focused ion beam technique were fabricated. The fabrication of this device was performed using two main steps: deposition followed by direct milling. Using a FILMETRICS F40-UV thin film analyzer, the measurement was performed once in the middle of the wafer (region where the device is patterned). Results of the analyzer showed that the thickness of Au and Cr films are 202.9 A (~ 20 nm) and 30.4 A (~ 3 nm), respectively. According to the Filmetrics Appnote-NIST Traceable Standards [109] and FILMETRICS F40-UV datasheet [110], the total uncertainty of the measurement is ~ $\pm$3 nm. So, the film thickness of Au and Cr can be reported as ~20$\pm$3 nm, and ~3$\pm$3 nm, respectively. For patterning the Au NP array, the Zeiss Auriga FIB-SEM system is used where direct-milling is performed. Fig. 6.2 shows the SEM image of the device with overall dimension of ~ 4 x 4 μm that includes ~ 20 x 20 Au

nano-disc array with the periodicity of ~215 nm, which is close to the desired periodicity (200 nm).

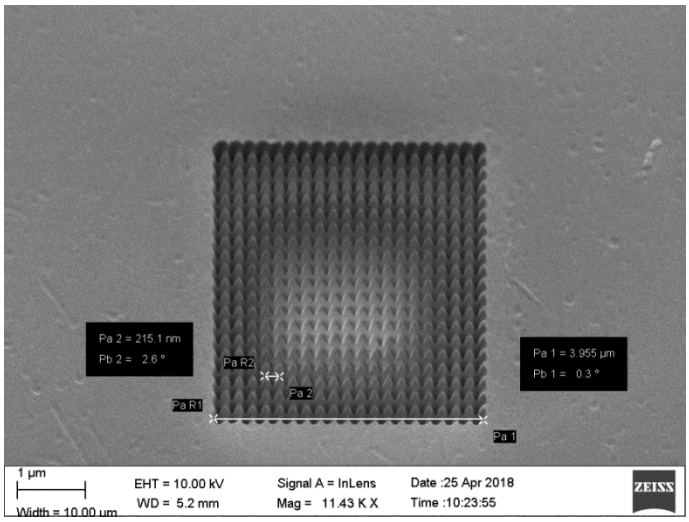

Figure 6.2: SEM image of Au NP array showing the device dimension and periodicity of Au NPs.

For measuring the Au NPs' height (milling depth), the AFM system is used. The average height (milling depth) of the device is ~ 37 nm. From Fig. 6.3, the nano-discs are in good order and well-spaced, and depth of milling between them is very comparable. A slight difference in the height of NPs may be attributed to a higher dose of gallium ions or a longer time in the milling process. In addition, from the depth of the milling results, it is evident that the resulting NPs are constructed from three materials: silica (bottom), chromium (middle), and gold (top).

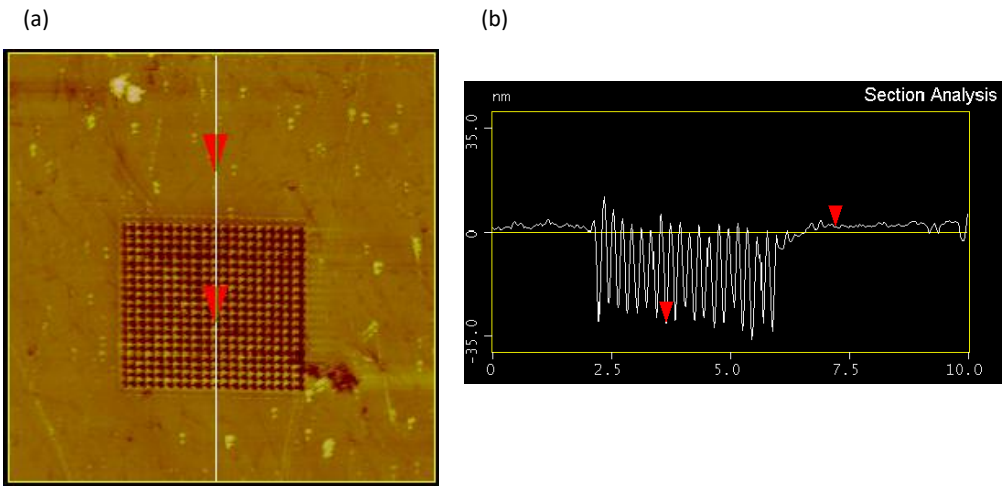

Figure 6.3: AFM image of Au NP array device (a) and cross section profile of Au NPs (b) for indicated white line in (a) where section analysis is performed.

Imaging using collection-transmission SNOM and AFM modes as in Fig. 6.4, shows the interaction of Au NPs with incident laser light of 532 nm wavelength. Fig. 6.4a shows the topography of the device and Fig. 6.4b is the SNOM image, which emphasizes the capability of the SNOM system in imaging the nanostructure. The number of photons scattered for Au nano-discs is counted using a SNOM photomultiplier, which recorded values in the range of 294.1 to 352.7 kHz, as shown in Fig. 6.4b. The interaction of the Au-NP array with an incident plane wave at 532 nm produces the light-scattering enhancement at the top of each NP and destructive interference at the top of each valley. Fig. 6.4c is the relative intensity of the scattered photon across the diagonal of the device (black line) which clearly shows minima and maxima and patterns due to interaction of radiation scattered in the near-field from neighbouring NPs. Each NP tip scatters light and locally produces strong field enhancement in a process equivalent to Mie scattering for spherical nanoparticles [111] and with an electric field distribution determined by a series of multipoles, as reported, for example, by Bohren and Huffman.[112]. The near-field contribution, strongly localized in the proximity of each NP apex, corresponds to the lowest term

of such a series, and is normally associated with the strongest field enhancement. The higher order terms of the series are less intense, more delocalized in space and, therefore less suited to localized surface plasmon resonance sensors. In order to assess the suitability of this device for sensing purposes, it is essential to study the near-field response at different tip-sample distances.

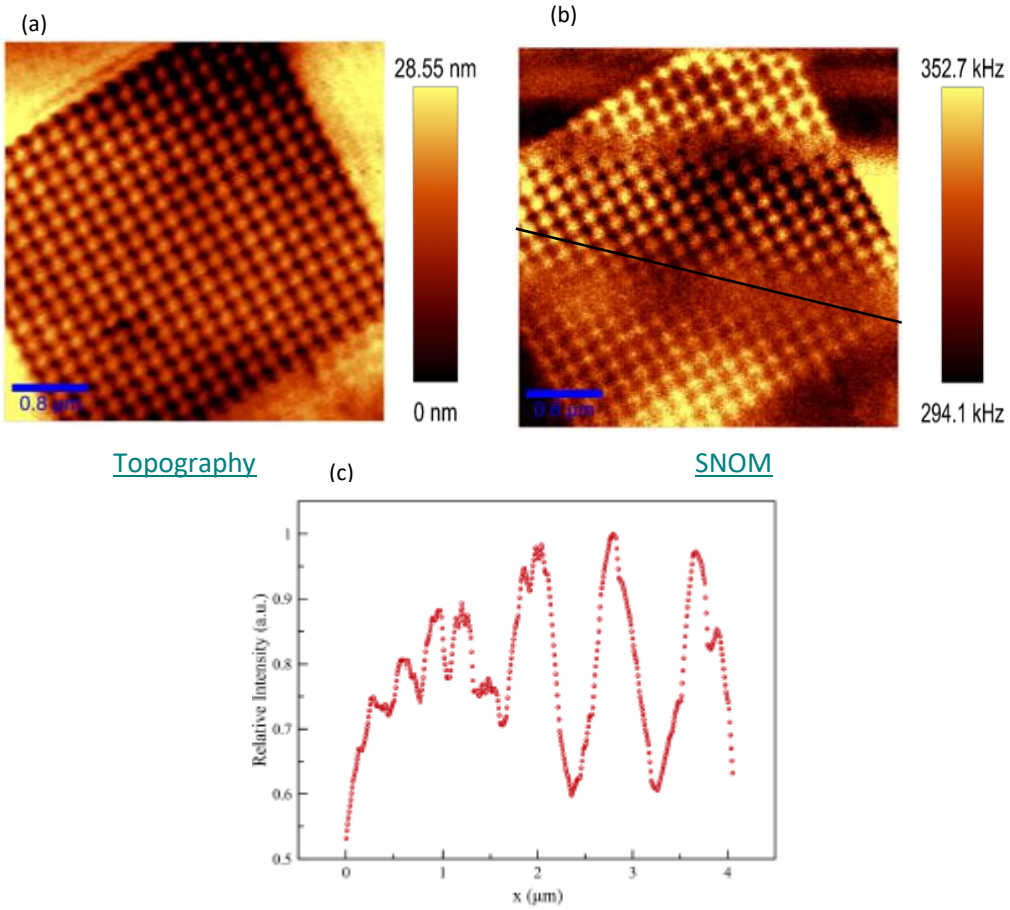

Figure 6.4: Topography (a) and SNOM image (b) of Au nano-disc array device. In the SNOM image, the scale bar represents the number of photons detected.

The refractive index of the medium affects the intensity of the constructive (or destructive) wave. When the wave travels in mediums of varying refractive indices, the intensity could change. Based on this point, the intensity of these constructive and destructive interferences can be used as a tool for the LSPR sensor. For instance, when the refractive index of the surrounding medium of NP changes, the intensity of the scattered photons changes, and from the shift in intensity, the change in analyte concentration can be detected. Simulation results as shown in Fig. 6.5, also show the maxima and minima intensity profile of scattered photons resulted from the interaction of Au NPs array with incident light, as reported experimentally. Fig. 6.5a shows the ability of imaging the nano-discs using an electric field profile that resulted from the scattering process after excitation, and Fig. 6.5b is the relative intensity of the scattered wave at different heights from the nanostructure (40, 100, & 500 nm), which shows the maxima and minima peaks resulting from constructive and destructive interference between Au NPs in the array. It is clear from Fig. 6.5b that as the monitor goes further from the NPs, the relative intensity and number of peaks decreases. A decrease in the level of intensity could be attributed to the transition from near-field to far-field, where localized plasmons modes are strongly localized in the NP proximity. A decrease in the number of peaks as the monitor is moved further from the nano-device can be illustrated from Fig. 6.5c. At a height of 40 nm, the monitor can detect the two fields' enhancement at the edges of each nano-disc, and that is the reason we first observed ~ 40 peaks (double the number of nano-discs in each row), and then a decreased number of peaks to 6 peaks at a monitor height equal to 500 nm. A decrease in the number of peaks as the monitor moves further from the nanostructure provides evidence of the reason the experimental intensity profile (Fig. 6.4c) shows the number of peaks being lower than the number of nano-discs, where the tip height was 500 nm. Differences between experimental and simulation results may be attributed to differences in the accuracy of

the fabricated Au NPs compared to the simulated case, as well as the capability of the SNOM instruments. However, both simulation and experiments show a similar trend in the intensity profile.

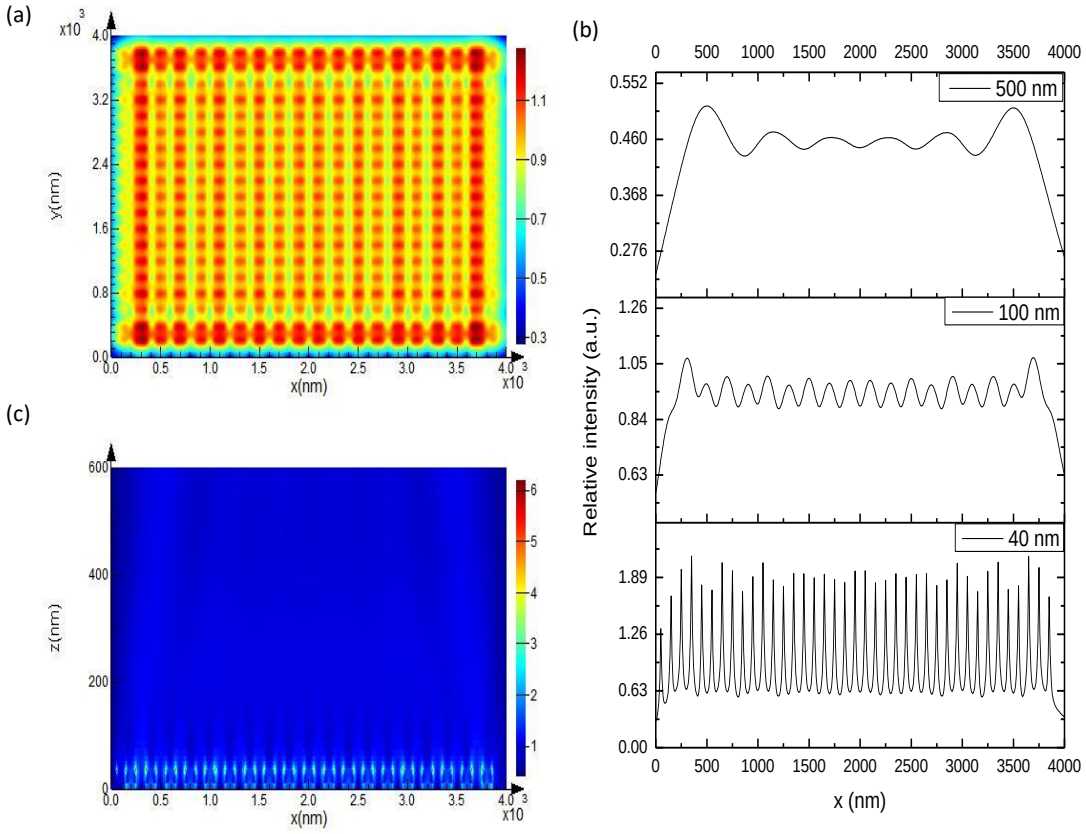

Figure 6.5: Top view of electric field profile of all Au nano-disc arrays (a), relative intensity profile of the x-y monitor at different heights (40, 100, & 500 nm) (b), and cross-section (x-z) electric field profile (c).

According to the Mie scattering theory, scattering intensity depends on different parameters and one of these is the NP's surrounding the refractive index (or permittivity) [111]. The results in Figure 6.5 were obtained in air. To study the device's capability for LSPR sensing, the intensity profile at a different refractive index of the NP's surrounding medium is calculated

using the FDTD method, as shown in Fig. 6.6. Relative intensity profiles were calculated at refractive index changes from 1 to 1.005 with 0.001 steps. This very small step examines the detection limit of the device in which detecting very small variations in the refractive index indicates the ability to detect a very small change in solution concentration. For instance, as reported by Belay and Assefa [113], the refractive index of sugar solution linearly increases with sugar concentration, and thus, a very small change in sugar concentration also yields a very small change in the refractive index. From Fig. 6.6a, it clearly shows the shift (decrease) in the scattering intensity (maxima), as the refractive index of the surrounding medium increases. A decrease in the scattering intensity in a higher refractive index medium agrees with the Mie scattering equation for metal NP, as reported by Ghosh and Pal [114]; as the refractive index of the surrounding medium increases, the scattering intensity decreases. The amount of shift in the peak labeled A versus refractive index change is plotted as shown in Fig. 6.6b, which illustrates the linear response of peak intensity to the refractive index change. A linear response of peak intensity to the refractive index variation shows the possibility of using SNOM technique to detect the local refractive index change in the NP's proximity, which enhances the chance for a nano-device to be utilized for localized surface plasmonic sensor applications, such as bio and gas sensors. However, the amount of change in peak intensity is very small, which is due to the tiny change of refractive index used here ($\Delta n = 0.001$) and this may be challenging in practical applications. Working with a higher refractive index change, for example $\Delta n = 0.01$, may result in a detectable intensity peak shift.

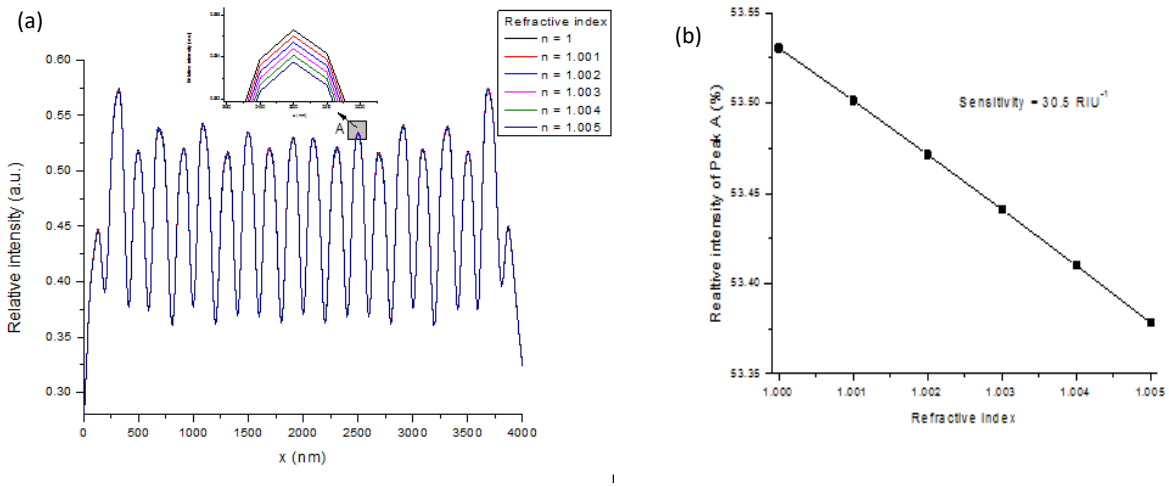

Figure 6.6: Intensity profile of Au NP array at different refractive index of surrounding medium (a) and the peak A intensity shift as the refractive index changes (b).

6.4 Conclusion

In this work, the interaction of sub-wavelength Au NP arrays with incident laser light is studied using the scanning near-field optical microscope (SNOM) technique. The nano-device was fabricated by direct milling process of Au thin film using FIB technology. The relative intensity profile obtained through imaging using SNOM clearly shows the scattering resulted from Au NPs through maxima and minima in the intensity profile, which is attributed to constructive and destructive interference between NPs. When the refractive index of the NPs' surrounding medium is changed, the intensity of the peak in the intensity profile is shifted linearly, which indicates that the amount of scattering intensity depends on the dielectric property of the surrounding medium as obtained numerically. The shift in the intensity value is obtained at a very low refractive index variation ($\Delta n = 0.001$), which highlights the achievable low-detection limit of the sensor and capability of the SNOM instrument for plasmonic sensing applications such as chemical/bio or gas sensors.

Chapter 7 Research Conclusions and Future Work

7.1 Research Conclusions

The following list is a summary of accomplished work included in this thesis:

1- A localized surface plasmonic resonance sensor with a high-figure of merit based on a gold-graphene spherical core-shell hybrid NP array placed on a quartz substrate was proposed, and its sensing performance was studied and analyzed numerically using the FDTD method. Sharp plasmonic resonance with full-width at half maximum of 7.8 nm was obtained, yielding a high figure of merit: 102.6. (Chapter 2)

2- Effects of the imbedding area between Au NP array with graphene on optical absorption of gold nanostructure were studied and presented. Enhancement in absorption was observed following addition of a graphene component. This hybrid nanostructure was then proposed as a localized surface plasmonic resonance sensor. High competitive sensitivity and figure of merit values were obtained as 4380 nm/RIU and 390, respectively. (Chapter 3)

3- A localized surface plasmonic resonance sensor with outstanding efficiency and good fabrication controllability based on gold-graphene hybrid nanostructure was proposed, and

its sensing performance was studied and analyzed numerically using the FDTD method. In this hybrid nanostructure, graphene is deposited directly on Au NP arrays, using for example, the chemical vapor deposition method. A figure of merit of 876 resulted, which is a very competitive value in the field of plasmonic sensors. (Chapter 4)

4- Effects of hybrid gold nanoparticles with graphene flakes on localized surface plasmonic resonance sensor performance were studied and analyzed numerically using the FDTD method. It has been demonstrated that randomly spin-coating graphene flakes of different shapes and sizes on top of a Au NP array device enhances plasmonic resonance and high sensor sensitivity, with 2242 nm/RIU being achieved. (Chapter 5)

Figure 7.1 shows the results of sensor performance (figure of merit) obtained in this work, which presents significant improvement compared to the literature.

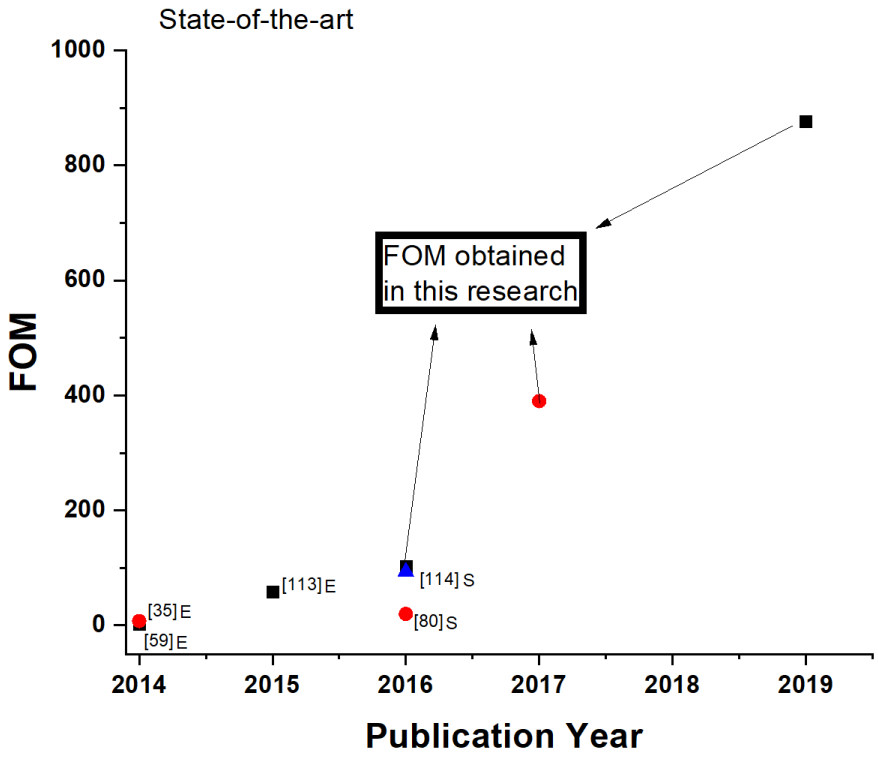

Figure 7.1: FOM results obtained in this research and compared to recent state of the art [35,59,80,115,116] (E & S refer to experimental and simulated reports, respectively)

5- Gold nanoparticle arrays have been fabricated on top of quartz substrates using focused ion beam technology, and their near-field light-NP interaction has been characterized using near-field optical microscopy. An intensity profile of scattered photons from Au NPs was measured, which showed constructive (maxima) and destructive (minima) interferences, and the capability for using intensity profile peaks for sensing purposes was demonstrated numerically using FDTD method. (Chapter 6)

Upon fixing substrate type and periodicity, there is still a large space of geometrical parameter effects on the plasmonic properties of the nanostructure, which may further improve sensing performance. For example, in Chapter 2, spherical core shell configuration has been studied and there are still other different configurations which require exploring, such as cubic

core shell and nano-rod core shell configurations, where better sensing performance could be obtained with nanoparticle shapes that have sharper corners [117] or higher aspect ratios [36], respectively. Furthermore, as reported [22], smaller NP size exhibits stronger plasmonic resonance and thus it is preferred for a superior sensing device; however, as mentioned for periodicity, challenges in fabrication also should be considered, where at smaller NP sizes, the fabrication challenges increase [76]. Regarding a graphene component, as reported in the literature [56] and also shown in chapter 2 in the core shell configuration, as thickness of graphene increases, better plasmonic properties and sensing performance are obtained. However, continuous increase of graphene thickness should be carefully considered, since at some point graphene changes to graphite and its good plasmonic properties may no longer be available. As reported by Li et al., it has been verified experimentally that graphene film thickness could reach up to ~ 23 nm thickness [118].

7.2 Sensitivity of the Sensor Performance Results to the Simulation Input Parameters

The results of the research so far confirm two focus points of this research study. The first is that hybrid graphene (in non-continuous film configuration) with Au NPs overcomes a performance issue of the LSPR sensor, which is clear from the obtained sensitivity and FOM values. The second point is that graphene can be hybridized with gold nanostructures in different configurations, and here just four cases are presented, all of which exhibit enhanced sensing performance compared to the literature, and more than these four configurations can be developed.

However, some of the input parameters values used in the simulation may have slightly different values during experimental implementation and may affect the output (sensing performance), accordingly. Therefore, the sensitivity of the sensor performance (sensitivity and FOM) to the slight change in the input parameters is analyzed and discussed in this section. The position of the source and detector applied in the simulation model will be examined first. Fig. 6.5b clearly shows that changing the position of the detector by a large value (40, 100, & 500 nm) results in significant changes in the intensity profile and intensity value. However, Fig. 6.5c shows that the field profile and intensity change gradually, and thus a slight change in the detector position (a few nanometers, for example) will not result in apparent or significant changes in the field profile and intensity values, while there is a significant change in the field profile if the detector change by 100 nm. As the detector goes further form the nanostructure, the peak intensity decreases. Based on that, the intensity value of the 1-T peaks used in Chps 2-5 (Au-G hybrid nanostructures) may change if the detector position changes significantly. However, the sensitivity of the sensor depends on how much the peak shifts (resonance wavelength or intensity) when the

refractive index of the sensing medium is changed, and it does not depend on the value of the peak intensity. As a result, no significant effect on the sensor sensitivity is expected when the position of the detector is changed slightly. Regarding the position of the source, as mentioned, the sensor performance is merely dependent on the shift in the plasmonic resonance after changes in the sensing medium refractive index; it doesn't depend on the energy of the incident light. Therefore, slight changes in the source position will not cause a significant change in the results as also reported here [68].

Another input parameter that may affect the sensing performance results is the refractive index of the substrate. In the simulation work conducted in this research, silica (quartz) with n = 1.45 is used. As reported by Emilie et al., the plasmonic resonance of Ag cube NPs could occur at either the NP– substrate (proximal) interface or the NP – sensing medium (distal) interface, as shown schematically in Fig. 7.2 [119]. In a proximal situation, any change in the refractive index of the substrate affects plasmonic resonance properties, and accordingly, sensor performance. However, according to the Au-G core-shell hybrid nanostructures studied here, the electric field profile shows that there is no significant proximal plasmonic resonance, and the distal case is dominant. Therefore, for any change in the refractive index of the substrate, there is no significant effect on plasmonic properties of the studied device, and thus no effect is expected on sensing performance, which is the opposite case for the other three hybrid nanostructures, where both distal and proximal plasmonic resonances occur (Fig. 7.2). In the case of proximal resonances, an increase in the refractive index of the substrate results in redshift of the plasmonic resonance [119] and could change and at the same time improve sensing performance [37] and vice versa.

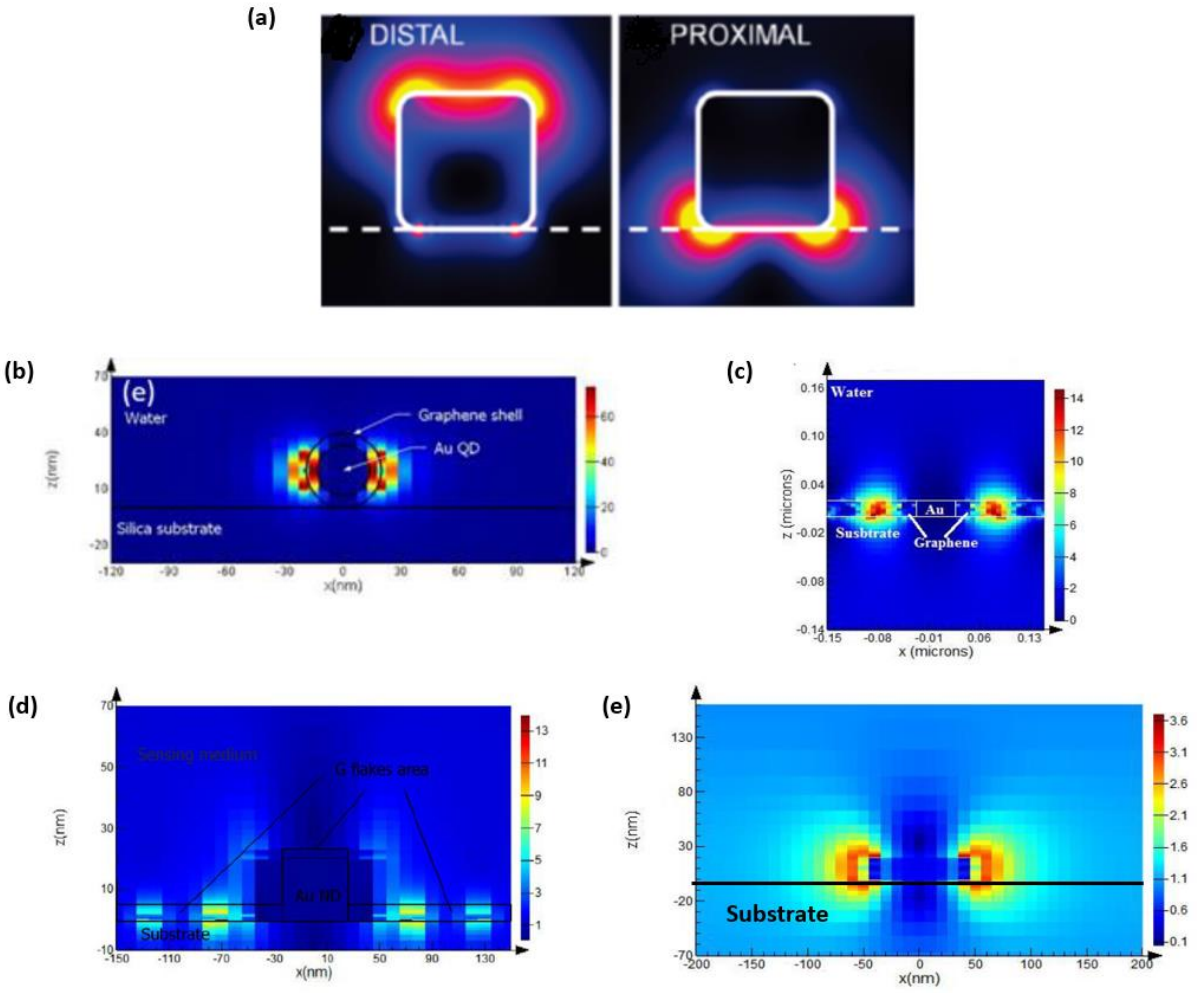

Figure 7.2: Schematic representation of distal and proximal plasmonic coupling of cubic NPs grown on a substrate [119] (a) and cross section electric profile of Au-G core-shell hybrid nanostructure (b), Au NP- G film hybrid nanostructure (c), Au NP- direct deposited G film hybrid nanostructure (d), and Au NP – G flakes hybrid nanostructure (e). All hybrid nanostructures show both distal and proximal plasmonic coupling resonances except for the core-shell structure that only presents distal resonance.

Above the substrate, nanostructures with gold and graphene material are used for developing a plasmonic sensor, and their dielectric property (refractive index or permittivity) plays an essential role in studying optical response to the incident light through solving Maxwell's equations. Equation 7.1below shows the dependency of NP extinction, according to Mie scattering theory [111], on the permittivity (also, refractive index) of the NP material (gold and graphene in this research).

$$\sigma_{ext}(\lambda) = \frac{24\pi^2 r^3 \varepsilon_d^{3/2} N}{\lambda \ln(10)} \frac{\varepsilon_i(\lambda)}{(\varepsilon_r(\lambda)+2\varepsilon_d)^2+\varepsilon_i(\lambda)^2} \qquad 7.1$$

where N is the electron density, λ is the incident wavelength, ε_d is the permittivity of the dielectric medium, ε_r and ε_i are the real and imaginary parts of the dielectric constant of metal NP, respectively. Therefore, change in the refractive index of the material will affect the amount of extinction; however, to the best of the author's knowledge, no study exists on the effect of slight changes of refractive index of material (gold and graphene) on the extinction. Nevertheless, by examining the equations of sensor sensitivity and FOM (Eq. 7.2 – 7.5), the sensing performance is mainly dependent on the amount of shift of resonance wavelength and intensity, not the amount of extinction, (see equations below). One exception here is for the FOM based on intensity shift (Eq. 7.5) where a significant change in the intensity value, if recorded, will affect the FOM of the sensor.

$$S_\lambda = \frac{\Delta\lambda}{\Delta n} \ (nm/RIU) \qquad (7.2)$$

$$S_I = \frac{\Delta I}{\Delta n} \ (RIU^{-1}) \qquad (7.3)$$

$$FOM_\lambda = \frac{S_\lambda}{\mathrm{FWHM}} \qquad (7.4)$$

$$FOM_I = \frac{S_I}{I_{ref.}} \quad (7.5)$$

Where $\Delta\lambda$ is the change in the resonance wavelength (nm), ΔI is the change in intensity, and S_λ, FOM_λ , S_I , FOM_I are sensitivity and figure of merit based on wavelength and intensity shift, respectively

Another factor that affects plasmonic properties of the nanostructure is periodicity. As presented and discussed in Ch 2, decreasing the periodicity results in decreases in the FWHM of the plasmonic resonance of the Au-G core-shell hybrid nanostructure. According to Eq. 7.4, decreases in the FWHM of the resonance band improve the FOM of the sensor, and a periodicity of 300 nm was chosen for subsequent simulation work due to the lower value of FHWM obtained. Moreover, it is not expected that slight changes in the periodicity during experimental implementation will result in a significant effect on the sensitivity and FOM of the sensor. From Fig. 2.3, the FWHM of the plasmon resonance band decreased from 8.1 nm to 7.8 nm upon decreasing the periodicity from 500 nm to 300 nm. Even though the change in the periodicity is large, the reduction of 0.3 nm reported is not significant. To see why this small change has no significant effect on the sensor FOM, the sensor for two values of FWHM using a sensitivity of 350 nm/RIU were calculated. Using Eq. 7.4, the FOM increased from 43.2 to 44.9 when the periodicity decreased from 500 nm to 300 nm. Thus, a slight change in the periodicity has no apparent or significant effect on the results of the sensor performance.

Furthermore, slightly change in the size of the nanostructure may have an apparent effect on the property of plasmonic resonance. For example, going back to table 2.1, changing the graphene thickness by 1 nm results in a change of less than 1 nm in the FWHM of resonance band, and in some cases, a few nanometers. For example, in the case of 40 nm Au NP size, changing

the graphene thickness from 3 nm to 4 nm results in FWHM reduction of 6.17 nm where this value is the minimum reduction value recorded in tuning the plasmonic properties of the core-shell hybrid nanostructure via nanostructure size. In addition, a small change in the FWHM of 0.5 nm was recorded when the graphene thickness was changed from 4 nm to 5 nm. Therefore, slight changes in the size of the nanostructure could result in change in the sensitivity and FOM of the sensor; however, it is noted that all FWHM in all cases have very low values, < 6.5 nm, which indicate that the sensing performance is still competitive compared to other metal-graphene hybrid nanostructures in the literature. For instance, based on table 2.2, the FOM ranges between 57.65 and 102.61, which is a considerable improvement compared to 2.8, the work reported by Murer et al. [59] and 20, the work reported by Pan et al. [80].

7.3 Sensor Sensitivity in Parts per Million Scale

As stated in section 1.2, the performance of an LSPR sensor can be assessed through measurement of sensitivity (S) and figure of merit (FOM). Sensitivity is the measurement of the degree to which a resonance wavelength or intensity shift per unit changes in the refractive index of a sensing medium. In addition, as reported by Shawana et al., the sensitivity of an LSPR sensor can be measured by the degree to which the resonance wavelength shifts for part per million (PPM) changes in a sensing medium concentration [120]. Shawana et al. developed a plasmonic sensor based on metal/graphene hybrid nanostructure by placing a graphene oxide film on top of a Au nano-disc and nanohole array. Their sensor demonstrated a sensitivity of 449.63 nm/RIU after applying different mediums on top of the device with different refractive indices: air, water, acetone, ethanol, isopropyl alcohol, and chloroform. Subsequently, they assessed the sensor

performance in response to the change in the sensing medium concentration by applying ethylene gas with concentrations ranging between 500 and 750 ppm, and observed sensitivity with 0.6 pico m/ ppm that is equivalent to 600 nm/ppm, which means a 600 nm shift in the resonance wavelength per one ppm change in the sensing medium concentration. Therefore, a sensor with sensitivity of 449.63 nm/RIU capable of observation of sensitivity of 600 nm/ppm concentrations and higher refractive index sensitivity is expected to yield higher concentration sensitivity as well. In this research, sensitivity with a value of 4380 nm/RIU in Au NP-G film hybrid nanostructure (Chp 3) is 7-fold greater than what is observed in the work by Shawana et al. Consequently, much higher concentration sensitivity (nm/ppm) is expected for the Au NP-G film hybrid nanostructure sensor. Using the same gas type and concentration used in Shawana et al.'s work, concentration sensitivity of the Au NP-G film hybrid nanostructure sensor is estimated to be >> 600 nm/ppm, and further experimental work is required to obtain an exact value. On the other hand, the minimum concentration can be detected by the sensor, i.e., limit of detection, is an essential performance parameter, especially in bio-applications where low concentrations of analyte (either in ng/ml or ppm) is required to diagnose cancer at an early stage, for example [121]. A plasmonic sensor with sharper resonance FWHM yields a better FOM and is expected to detect lower concentrations because by monitoring sharper resonance, tiny shifts in the resonance for small changes in analyte concentration are observable. According to Yang et al., a gold mushroom NP array plasmonic device registers a FOM of 108 and can detect 10 ng/ml, which is equivalent to 0.015 ppm (1 ppm = 1000 ng/ml) of Alpha-fetoprotein (AFP) protein which is a biomarker for hepatocellular carcinoma cancer [91]. In this research, a FOM of 856.2 is obtained by direct deposition of graphene on top of a Au NP array (Chp 4) which represents ~ 8-fold greater value than that observed in Yang et al.'s work. Therefore, << 0.015 ppm (15 ng/ml) is estimated to be detected

(experimental work is required to obtain an exact value) which represents a significant improvement in diagnosis of hepatocellular carcinoma cancer at an early stage [121].

In summary, the current results of this research show that hybridizing graphene with gold NPs is a promising way to solve LSPR sensing performance issues, and additionally, graphene can be hybridized with Au NPs in a broad range of configurations. So far, very competitive sensing performance results compared to the current literature were obtained, and further research is recommended for additional exploration of plasmonic properties of graphene-gold hybrid nanostructures, considering different hybrid configurations, periodicity, and geometrical parameters.

7.4 Further Research

Fabricate and characterize the sensor introduced in Chapter 4 by direct deposition of graphene film on top of the fabricated gold nanostructure (Chapter 7). In addition, measure the sensitivity of the sensor to < 15 ng/ml concentration of APF to assess its limit of detection. After that, **incorporate** the tested device in an optical microscopy system and discuss reliability and the cost of the system by comparing it to commercialized systems in the present market.

Further optimization is still recommended for the gold-graphene hybrid nanostructure through considering different hybrid configurations such as cubic core-shell structure, various gold

NP shapes such as nano rods, different graphene thicknesses ranging from a few layers up to 23 nm, and periodicity smaller than 300 nm.

7.5 List of Publications during Doctoral Study

Raed, A., Mehrdad I., Mustafa Y. (2016, June 12-17). *Gold-Graphene core-shell quantum dot surface Plasmon sensors.* Poster presented at the 7th International Conference on Optical, Optoelectronic and Photonic Materials, ICOOPMA, Montreal. (**Conference**)

Alharbi, R., Irannejad, M., & Yavuz, M. (2017). Gold-graphene core-shell nanostructure surface plasmon sensors. *Plasmonics*, *12*(3), 783-794. (**Published**)

Alharbi, R., Irannejad, M., & Yavuz, M. (2017). Au-Graphene Hybrid Plasmonic Nanostructure Sensor Based on Intensity Shift. *Sensors*, *17*(1), 191. (**Published**)

Alharbi, R., Irannejad, M., & Yavuz, M. (2019). A Short Review on the Role of the Metal-Graphene Hybrid Nanostructure in Promoting the Localized Surface Plasmon Resonance Sensor Performance. *Sensors*, *19*(4), 862. (**Published**)

Alharbi, R., & Yavuz, M. (2019, June). Promote Localized Surface Plasmonic Sensor Performance via Spin-Coating Graphene Flakes over Au Nano-Disk Array. In *Photonics* (Vol. 6, No. 2, p. 57). Multidisciplinary Digital Publishing Institute. (**Published**)

Alharbi, R, & Yavuz, M. (2019) “Direct Deposition of Graphene Sheets over Gold Nano-Disks Array for Enhancing Localized Surface Plasmon Resonance Sensor Performance” (Superlattice and Microstructure, Elsevier**) (Planned for publication**)

Raed Alharbi1, Victor Wong, Abdullah H. Alshehri, Giovanni Fanchini, & Mustafa Yavuz “Scanning near-field optical microscopy assisted design of sensing enhancement devices based on localized surface plasmon resonance” Ann Phys. (**Submitted**)

7.6 List of Publications during Master Study

Raed, A., Mehrdad I., Mustafa Y. (2016, June 12-17). Optical, Morphology and Mechanical Properties of Aluminum Thin Films Micromirror. Poster presented at the 7th International Conference on Optical, Optoelectronic and Photonic Materials, ICOOPMA, Montreal. (**Conference**)

Bibliography

1. Feynman, R. There's Plenty of Room at the Bottom, Engineering and Science. *Engineering and Science* **1960**, 22-36.

2. Tjong, S.C. Carbon Nanotube Reinforced Composites. *NY: Wiley-VCH* **2009**.

3. Zeng, S.; Yu, X.; Law, W.; Zhang, Y.; Hu, R.; Dinh, X.; Ho, H.; Yong, K. Size Dependence of Au NP-Enhanced Surface Plasmon Resonance Based on Differential Phase Measurement. *Sensors Actuators B: Chem.* **2013**, *176*, 1128-1133.

4. Pluchery, O.; Vayron, R.; Van, K. Laboratory Experiments for Exploring the Surface Plasmon Resonance. *European Journal of Physics* **2011**, *32*, 585.

5. Wang, M.; Huo, Y.; Jiang, S.; Zhang, C.; Yang, C.; Ning, T.; Liu, X.; Li, C.; Zhang, W.; Man, B. Theoretical Design of a Surface Plasmon Resonance Sensor with High Sensitivity and High Resolution Based on graphene–WS 2 Hybrid Nanostructures and Au–Ag Bimetallic Film. *RSC Advances* **2017**, *7*, 47177-47182.

6. Mie, G. Articles on the Optical Characteristics of Turbid Tubes, especially Colloidal Metal Solutions. *Ann.Phys* **1908**, *25*, 377-445.

7. Dmitriev, A. *Nanoplasmonic Sensors*.; Springer Science & Business Media, 2012.

8. Hammond, J.L.; Bhalla, N.; Rafiee, S.D.; Estrela, P. Localized Surface Plasmon Resonance as a Biosensing Platform for Developing Countries. *Biosensors* **2014**, *4*, 172-188.

9. Martinsson, E.; Aili, D. Refractometric Sensing using Plasmonic Nanoparticles. *Encyclopedia of Nanotechnology* **2014**, 1-11.

10. Lopez, G.A.; Estevez, M.; Soler, M.; Lechuga, L.M. Recent Advances in Nanoplasmonic Biosensors: Applications and Lab-on-a-Chip Integration. *Nanophotonics* **2017**, *6*, 123.

11. Mayer, K.M.; Hafner, J.H. Localized Surface Plasmon Resonance Sensors. *Chem. Rev.* **2011**, *111*, 3828-3857.

12. Ge, C.; Tao, Y.; Guo, Z. Biosensors Based on Plasmonics. *Biosens J* **2015**, *4*, 2.

13. Haes, A.J.; Duyne, R.P.V. Preliminary Studies and Potential Applications of Localized Surface Plasmon Resonance Spectroscopy in Medical Diagnostics. *Expert Review of Molecular Diagnostics* **2004**, *4*, 527-537.

14. Malinsky, M.D.; Kelly, K.L.; Schatz, G.C.; Van Duyne, R.P. Chain Length Dependence and Sensing Capabilities of the Localized Surface Plasmon Resonance of Silver Nanoparticles

Chemically Modified with Alkanethiol Self-Assembled Monolayers. *J. Am. Chem. Soc.* **2001**, *123*, 1471-1482.

15. McFarland, A.D.; Van Duyne, R.P. Single Silver Nanoparticles as Real-Time Optical Sensors with Zeptomole Sensitivity. *Nano letters* **2003**, *3*, 1057-1062.

16. Ameen, A.; Gartia, M.R.; Hsiao, A.; Chang, T.; Xu, Z.; Liu, G.L. Ultra-Sensitive Colorimetric Plasmonic Sensing and Microfluidics for Biofluid Diagnostics using Nanohole Array. *Journal of Nanomaterials* **2015**, *16*, 35.

17. Farhang, A.; Abasahl, B.; Martin, O.J. Hybrid Nanoparticle and Thin Film SPR Biosensor with a High Figure of Merit. In Plasmonics in Biology and Medicine IX; pp. 82340P.

18. Haddada, M.B.; Hu, D.; Salmain, M.; Zhang, L.; Peng, C.; Wang, Y.; Liedberg, B.; Boujday, S. Gold Nanoparticle-Based Localized Surface Plasmon Immunosensor for Staphylococcal Enterotoxin A (SEA) Detection. *Analytical and bioanalytical chemistry* **2017**, *409*, 6227-6234.

19. Spadavecchia, J.; Perumal, R.; Barras, A.; Lyskawa, J.; Woisel, P.; Laure, W.; Pradier, C.; Boukherroub, R.; Szunerits, S. Amplified Plasmonic Detection of DNA Hybridization using Doxorubicin-Capped Gold Particles. *Analyst* **2014**, *139*, 157-164.

20. Lin, C.; Chang, C.; Cagle, P. Breast Cancer Detection using Surface Plasmon Resonance-Based Biosensors. *Biosensors and Cancer* **2012**, *17*.

21. Brolo, A.G. Plasmonics for Future Biosensors. *Nature Photonics* **2012**, *6*, 709.

22. Paramelle, D.; Sadovoy, A.; Gorelik, S.; Free, P.; Hobley, J.; Fernig, D.G. A Rapid Method to Estimate the Concentration of Citrate Capped Silver Nanoparticles from UV-Visible Light Spectra. *Analyst* **2014**, *139*, 4855-4861.

23. Johnson, P.B.; Christy, R. Optical Constants of the Noble Metals. *Physical review B* **1972**, *6*, 4370.

24. Mock, J.J.; Smith, D.R.; Schultz, S. Local Refractive Index Dependence of Plasmon Resonance Spectra from Individual Nanoparticles. *Nano Letters* **2003**, *3*, 485-491.

25. Sun, Y.; Xia, Y. Increased Sensitivity of Surface Plasmon Resonance of Gold Nanoshells Compared to that of Gold Solid Colloids in Response to Environmental Changes. *Anal. Chem.* **2002**, *74*, 5297-5305.

26. Sepúlveda, B.; Angelomé, P.C.; Lechuga, L.M.; Liz-Marzán, L.M. LSPR-Based Nanobiosensors. *Nano Today* **2009**, *4*, 244-251.

27. Guo, L.; Yin, Y.; Huang, R.; Qiu, B.; Lin, Z.; Yang, H.; Li, J.; Chen, G. Enantioselective Analysis of Melagatran Via an LSPR Biosensor Integrated with a Microfluidic Chip. *Lab on a Chip* **2012**, *12*, 3901-3906.

28. Sekhon, J.S.; Verma, S. Refractive Index Sensitivity Analysis of Ag, Au, and Cu Nanoparticles. *Plasmonics* **2011**, *6*, 311-317.

29. Chan, G.H.; Zhao, J.; Schatz, G.C.; Van Duyne, R.P. Localized Surface Plasmon Resonance Spectroscopy of Triangular Aluminum Nanoparticles. *The Journal of Physical Chemistry C* **2008**, *112*, 13958-13963.

30. Park, Y.R.; Liu, N.; Lee, C.J. Photoluminescence Enhancement from Hybrid Structures of Metallic Single-Walled Carbon Nanotube/ZnO Films. *Current Applied Physics* **2013**, *13*, 2026-2032.

31. Link, S.; El-Sayed, M.A. Size and Temperature Dependence of the Plasmon Absorption of Colloidal Gold Nanoparticles. *The Journal of Physical Chemistry B* **1999**, *103*, 4212-4217.

32. Bukasov, R.; Shumaker-Parry, J.S. Highly Tunable Infrared Extinction Properties of Gold Nanocrescents. *Nano letters* **2007**, *7*, 1113-1118.

33. Hammond, J.; Bhalla, N.; Rafiee, S.; Estrela, P. Localized Surface Plasmon Resonance as a Biosensing Platform for Developing Countries. *Biosensors* **2014**, *4*, 172-188.

34. Sherry, L.J.; Chang, S.; Schatz, G.C.; Van Duyne, R.P.; Wiley, B.J.; Xia, Y. Localized Surface Plasmon Resonance Spectroscopy of Single Silver Nanocubes. *Nano letters* **2005**, *5*, 2034-2038.

35. Toma, M.; Cho, K.; Wood, J.B.; Corn, R.M. Gold Nanoring Arrays for Near Infrared Plasmonic Biosensing. *Plasmonics* **2014**, *9*, 765-772.

36. Hanarp, P.; Käll, M.; Sutherland, D.S. Optical Properties of Short Range Ordered Arrays of Nanometer Gold Disks Prepared by Colloidal Lithography. *The Journal of Physical Chemistry B* **2003**, *107*, 5768-5772.

37. Ross, M.B.; Mirkin, C.A.; Schatz, G.C. Optical Properties of One-, Two-, and Three-Dimensional Arrays of Plasmonic Nanostructures. *The journal of physical chemistry C* **2016**, *120*, 816-830.

38. Martinsson, E.; Sepulveda, B.; Chen, P.; Elfwing, A.; Liedberg, B.; Aili, D. Optimizing the Refractive Index Sensitivity of Plasmonically Coupled Gold Nanoparticles. *Plasmonics* **2014**, *9*, 773-780.

39. Jain, P.K.; Lee, K.S.; El-Sayed, I.H.; El-Sayed, M.A. Calculated Absorption and Scattering Properties of Gold Nanoparticles of Different Size, Shape, and Composition: Applications in Biological Imaging and Biomedicine. *The journal of physical chemistry B* **2006**, *110*, 7238-7248.

40. Enoch, S.; Bonod, N. *Plasmonics: From Basics to Advanced Topics*.; Springer, 2012.

41. Chung, T.; Lee, S.; Song, E.Y.; Chun, H.; Lee, B. Plasmonic Nanostructures for Nano-Scale Bio-Sensing. *Sensors* **2011**, *11*, 10907-10929.

42. Prodan, E.; Radloff, C.; Halas, N.J.; Nordlander, P. A Hybridization Model for the Plasmon Response of Complex Nanostructures. *Science* **2003**, *302*, 419-422.

43. Teo, S.L.; Lin, V.K.; Marty, R.; Large, N.; Llado, E.A.; Arbouet, A.; Girard, C.; Aizpurua, J.; Tripathy, S.; Mlayah, A. Gold Nanoring Trimers: A Versatile Structure for Infrared Sensing. *Optics express* **2010**, *18*, 22271-22282.

44. Tam, F.; Moran, C.; Halas, N. Geometrical Parameters Controlling Sensitivity of Nanoshell Plasmon Resonances to Changes in Dielectric Environment. *The Journal of Physical Chemistry B* **2004**, *108*, 17290-17294.

45. McPhillips, J.; Murphy, A.; Jonsson, M.P.; Hendren, W.R.; Atkinson, R.; Höök, F.; Zayats, A.V.; Pollard, R.J. High-Performance Biosensing using Arrays of Plasmonic Nanotubes. *ACS nano* **2010**, *4*, 2210-2216.

46. McMahon, M.; Lopez, R.; Meyer, H.; Feldman, L.; Haglund, R. Rapid Tarnishing of Silver Nanoparticles in Ambient Laboratory Air. *Applied Physics B* **2005**, *80*, 915-921.

47. Nagpal, P.; Lindquist, N.C.; Oh, S.H.; Norris, D.J. Ultrasmooth Patterned Metals for Plasmonics and Metamaterials. *Science* **2009**, *325*, 594-597.

48. Park, Y.; Cha, S.; Saito, Y.; Prinz, F.B. Gas-Tight Alumina Films on Nanoporous Substrates through Oxidation of Sputtered Metal Films. *Thin Solid Films* **2005**, *476*, 168-173.

49. Reed, J.C.; Zhu, H.; Zhu, A.Y.; Li, C.; Cubukcu, E. Graphene-Enabled Silver Nanoantenna Sensors. *Nano letters* **2012**, *12*, 4090-4094.

50. Li, Y.; Dong, F.; Chen, Y.; Zhang, X.; Wang, L.; Bi, Y.; Tian, Z.; Liu, Y.; Feng, J.; Sun, H. As-Grown Graphene/Copper Nanoparticles Hybrid Nanostructures for Enhanced Intensity and Stability of Surface Plasmon Resonance. *Scientific reports* **2016**, *6*, 37190.

51. Chuang, C.; Aoh, J.; Din, R. Oxidation of Copper Pads and its Influence on the Quality of Au/Cu Bonds during Thermosonic Wire Bonding Process. *Microelectronics Reliability* **2006**, *46*, 449-458.

52. Kim, D.; Yoo, S.M.; Park, T.J.; Yoshikawa, H.; Tamiya, E.; Park, J.Y.; Lee, S.Y. Plasmonic Properties of the Multispot Copper-Capped Nanoparticle Array Chip and its Application to Optical Biosensors for Pathogen Detection of Multiplex DNAs. *Anal. Chem.* **2011**, *83*, 6215-6222.

53. Giovannetti, G.; Khomyakov, P.; Brocks, G.; Karpan, V.v.; Van den Brink, J.; Kelly, P.J. Doping Graphene with Metal Contacts. *Phys. Rev. Lett.* **2008**, *101*, 026803.

54. Xu, G.; Liu, J.; Wang, Q.; Hui, R.; Chen, Z.; Maroni, V.A.; Wu, J. Plasmonic Graphene Transparent Conductors. *Adv Mater* **2012**, *24*, OP71-OP76.

55. Liu, J.; Xu, G.; Rochford, C.; Lu, R.; Wu, J.; Edwards, C.M.; Berrie, C.L.; Chen, Z.; Maroni, V.A. Doped Graphene Nanohole Arrays for Flexible Transparent Conductors. *Appl. Phys. Lett.* **2011**, *99*, 023111.

56. Nan, H.; Chen, Z.; Jiang, J.; Li, J.; Zhao, W.; Ni, Z.; Gu, X.; Xiao, S. The Effect of Graphene on Surface Plasmon Resonance of Metal Nanoparticles. *Physical Chemistry Chemical Physics* **2018**, *20*, 25078-25084.

57. Chen, Z.; Li, X.; Wang, J.; Tao, L.; Long, M.; Liang, S.; Ang, L.K.; Shu, C.; Tsang, H.K.; Xu, J. Synergistic Effects of Plasmonics and Electron Trapping in Graphene Short-Wave Infrared Photodetectors with Ultrahigh Responsivity. *ACS nano* **2017**, *11*, 430-437.

58. Wu, Y.; Niu, J.; Danesh, M.; Liu, J.; Chen, Y.; Ke, L.; Qiu, C.; Yang, H. Localized Surface Plasmon Resonance in Graphene Nanomesh with Au Nanostructures. *Appl. Phys. Lett.* **2016**, *109*, 041106.

59. Maurer, T.; Nicolas, R.; Lévêque, G.; Subramanian, P.; Proust, J.; Béal, J.; Schuermans, S.; Vilcot, J.; Herro, Z.; Kazan, M. Enhancing LSPR Sensitivity of Au Gratings through Graphene Coupling to Au Film. *Plasmonics* **2014**, *9*, 507-512.

60. Ihrig, M. A New Research Architecture for the Simulation Era. In *Seminal Contributions to Modelling and Simulation*.; Anonymous .; Springer, 2016; pp. 47-55.

61. Li, Z. *Plasmonic nano apertures for molecular sensing and colour displays* **2015**.

62. Yee, K. Numerical Solution of Initial Boundary Value Problems Involving Maxwell's Equations in Isotropic Media. *IEEE Transactions on antennas and propagation* **1966**, *14*, 302-307.

63. Sullivan, D.M. *Electromagnetic Simulation using the FDTD Method*.; John Wiley & Sons, 2013.

64. Haynes, W.M. *CRC Handbook of Chemistry and Physics*.; CRC press, 2014.

65. Falkovsky, L.A. Optical Properties of Graphene and IV–VI Semiconductors. *Physics-Uspekhi* **2008**, *51*, 887.

66. Haynes, W.M. *CRC Handbook of Chemistry and Physics*.; CRC press, 2014.

67. Falkovsky, L.A. Optical Properties of Graphene and IV–VI Semiconductors. *Physics-Uspekhi* **2008**, *51*, 887.

68. Lumerical Solutions Inc. Mesh Refinement Options. , *2018*.

69. Berenger, J. A Perfectly Matched Layer for the Absorption of Electromagnetic Waves. *Journal of computational physics* **1994**, *114*, 185-200.

70. Sreejith, S.; Joseph, J.; Nguyen, K.T.; Murukeshan, V.M.; Lye, S.W.; Zhao, Y. Graphene Oxide Wrapping of Gold–silica Core–shell Nanohybrids for Photoacoustic Signal Generation and Bimodal Imaging. *ChemNanoMat* **2015**, *1*, 39-45.

71. Li, Q.; Zhang, Z. Bonding and Anti-Bonding Modes of Plasmon Coupling Effects in TiO2-Ag Core-Shell Dimers. *Sci. Rep.* **2016**, *6*, 19433.

72. Staudinger, C.; Borisov, S.M. Long-Wavelength Analyte-Sensitive Luminescent Probes and Optical (Bio) Sensors. *Methods and applications in fluorescence* **2015**, *3*, 042005.

73. Li, J.; Chen, K.; Liu, H.; Cheng, K.; Yang, M.; Zhang, J.; Cheng, J.D.; Zhang, Y.; Cheng, Z. Activatable Near-Infrared Fluorescent Probe for in Vivo Imaging of Fibroblast Activation Protein-Alpha. *Bioconjug. Chem.* **2012**, *23*, 1704-1711.

74. Irannejad, M.; Cui, B.; Yavuz, M. Optical Properties and Liquid Sensitivity of Au-SiO 2-Au Nanobelt Structure. *Plasmonics* **2016**, *11*, 1-9.

75. Martinsson, E. *Nanoplasmonic Sensing Using Metal Nanoparticles* **2014**.

76. Lindquist, N.C.; Nagpal, P.; McPeak, K.M.; Norris, D.J.; Oh, S. Engineering Metallic Nanostructures for Plasmonics and Nanophotonics. *Reports on Progress in Physics* **2012**, *75*, 036501.

77. Maier, S.A. *Plasmonics: Fundamentals and Applications*.; Springer Science & Business Media, 2007.

78. Kofke, M.J.; Waldeck, D.H.; Walker, G.C. Composite Nanoparticle Nanoslit Arrays: A Novel Platform for LSPR Mediated Subwavelength Optical Transmission. *Optics express* **2010**, *18*, 7705-7713.

79. Maurer, T.; Nicolas, R.; Lévêque, G.; Subramanian, P.; Proust, J.; Béal, J.; Schuermans, S.; Vilcot, J.; Herro, Z.; Kazan, M. Enhancing LSPR Sensitivity of Au Gratings through Graphene Coupling to Au Film. *Plasmonics* **2014**, *9*, 507-512.

80. Pan, M.; Liang, Z.; Wang, Y.; Chen, Y. Tunable Angle-Independent Refractive Index Sensor Based on Fano Resonance in Integrated Metal and Graphene Nanoribbons. *Scientific reports* **2016**, *6*, 29984.

81. Blake, P.; Ahn, W.; Roper, D.K. Enhanced Uniformity in Arrays of Electroless Plated Spherical Gold Nanoparticles using Tin Presensitization. *Langmuir* **2009**, *26*, 1533-1538.

82. Shim, J.; Yun, J.M.; Yun, T.; Kim, P.; Lee, K.E.; Lee, W.J.; Ryoo, R.; Pine, D.J.; Yi, G.; Kim, S.O. Two-Minute Assembly of Pristine Large-Area Graphene Based Films. *Nano letters* **2014**, *14*, 1388-1393.

83. Irannejad, M.; Alyalak, W.; Burzhuev, S.; Brzezinski, A.; Yavuz, M.; Cui, B. Engineering of Bi-/Mono-Layer Graphene Film using Reactive Ion Etching. *Transactions on Electrical and Electronic Materials* **2015**, *16*, 169-172.

84. Zhu, S.; Zhou, W. Plasmonic Properties of Two-Dimensional Metallic Nanoholes Fabricated by Focused Ion Beam Lithography. *Journal of Nanoparticle Research* **2012**, *14*, 652.

85. Bukasov, R.; Shumaker-Parry, J.S. Highly Tunable Infrared Extinction Properties of Gold Nanocrescents. *Nano letters* **2007**, *7*, 1113-1118.

86. Ebbesen, T.W.; Lezec, H.J.; Ghaemi, H.; Thio, T.; Wolff, P.A. Extraordinary Optical Transmission through Sub-Wavelength Hole Arrays. *Nature* **1998**, *391*, 667.

87. Huang, X.; El-Sayed, M.A. Gold Nanoparticles: Optical Properties and Implementations in Cancer Diagnosis and Photothermal Therapy. *Journal of advanced research* **2010**, *1*, 13-28.

88. Zhao, B.; Zhao, J.; Zhang, Z. Enhancement of Near-Infrared Absorption in Graphene with Metal Gratings. *Appl. Phys. Lett.* **2014**, *105*, 031905.

89. Zuber, A.; Purdey, M.; Schartner, E.; Forbes, C.; van der Hoek, B.; Giles, D.; Abell, A.; Monro, T.; Ebendorff-Heidepriem, H. Detection of Gold Nanoparticles with Different Sizes using Absorption and Fluorescence Based Method. *Sensors Actuators B: Chem.* **2016**, *227*, 117-127.

90. Cattoni, A.; Ghenuche, P.; Haghiri-Gosnet, A.; Decanini, D.; Chen, J.; Pelouard, J.; Collin, S. Λ3/1000 Plasmonic Nanocavities for Biosensing Fabricated by Soft UV Nanoimprint Lithography. *Nano letters* **2011**, *11*, 3557-3563.

91. Shen, Y.; Zhou, J.; Liu, T.; Tao, Y.; Jiang, R.; Liu, M.; Xiao, G.; Zhu, J.; Zhou, Z.; Wang, X. Plasmonic Gold Mushroom Arrays with Refractive Index Sensing Figures of Merit Approaching the Theoretical Limit. *Nature communications* **2013**, *4*, 2381.

92. Dhawan, A.; Gerhold, M.; Russell, P.; Vo-Dinh, T.; Leonard, D. Fabrication of Metallic Nanodot Structures using Focused Ion Beam (FIB) and Electron Beam-Induced Deposition for Plasmonic Waveguides. In Quantum Dots, Particles, and Nanoclusters VI; pp. 722414.

93. Link, S.; El-Sayed, M.A. Shape and Size Dependence of Radiative, Non-Radiative and Photothermal Properties of Gold Nanocrystals. *International reviews in physical chemistry* **2000**, *19*, 409-453.

94. Fujita, J.; Hiyama, T.; Hirukawa, A.; Kondo, T.; Nakamura, J.; Ito, S.; Araki, R.; Ito, Y.; Takeguchi, M.; Pai, W.W. Near Room Temperature Chemical Vapor Deposition of Graphene with Diluted Methane and Molten Gallium Catalyst. *Scientific reports* **2017**, *7*, 12371.

95. Tyona, M. A Theoritical Study on Spin Coating Technique. *Advances in materials Research* **2013**, *2*, 195-208.

96. Rommel, M.; Bauer, A.; Frey, L. Simple and Efficient Method to Fabricate Nano Cone Arrays by FIB Milling Demonstrated on Planar Substrates and on Protruded Structures. *Microelectronic Engineering* **2012**, *98*, 242-245.

97. Jain, P.K.; Lee, K.S.; El-Sayed, I.H.; El-Sayed, M.A. Calculated Absorption and Scattering Properties of Gold Nanoparticles of Different Size, Shape, and Composition: Applications in Biological Imaging and Biomedicine. *J Phys Chem B* **2006**, *110*, 7238-7248.

98. Nicoletti, O.; de La Peña, F.; Leary, R.K.; Holland, D.J.; Ducati, C.; Midgley, P.A. Three-Dimensional Imaging of Localized Surface Plasmon Resonances of Metal Nanoparticles. *Nature* **2013**, *502*, 80.

99. Mie, G. Articles on the Optical Characteristics of Turbid Tubes, especially Colloidal Metal Solutions. *Ann.Phys* **1908**, *25*, 377-445.

100. Ibrahim, K.H.; Irannejad, M.; Hajialamdari, M.; Ramadhan, A.; Musselman, K.P.; Sanderson, J.; Yavuz, M. A Novel Femtosecond Laser-Assisted Method for the Synthesis of Reduced Graphene Oxide Gels and Thin Films with Tunable Properties. *Advanced Materials Interfaces* **2016**, *3*, 1500864.

101. Ibrahim, K.H.; Irannejad, M.; Wales, B.; Sanderson, J.; Musselman, K.P.; Yavuz, M. The Effect of Varying Ultrafast Pulse Laser Energies on the Electrical Properties of Reduced Graphene Oxide Sheets in Solution. *J Electron Mater* **2018**, *47*, 1117-1124.

102. Oh, B.; Chun, B.S.; Park, K.; Lee, W.; Lee, W.H.; Choi, J. Fabrication of Protein G LB Film for Immunoglobulin G Immobilization. *Materials Science and Engineering: C* **2004**, *24*, 65-69.

103. Makaraviciute, A.; Ramanavicius, A.; Ramanaviciene, A. Development of a Reusable Protein G Based SPR Immunosensor for Direct Human Growth Hormone Detection in Real Samples. *Analytical Methods* **2015**, *7*, 9875-9884.

104. Rahman, M.S.; Hasan, M.R.; Rikta, K.A.; Anower, M. A Novel Graphene Coated Surface Plasmon Resonance Biosensor with Tungsten Disulfide (WS2) for Sensing DNA Hybridization. *Optical Materials* **2018**, *75*, 567-573.

105. Xue, T.; Liang, W.; Li, Y.; Sun, Y.; Xiang, Y.; Zhang, Y.; Dai, Z.; Duo, Y.; Wu, L.; Qi, K. Ultrasensitive Detection of miRNA with an Antimonene-Based Surface Plasmon Resonance Sensor. *Nature communications* **2019**, *10*, 28.

106. Kriese, M.; Moody, N.; Gerberich, W.W. Effects of Annealing and Interlayers on the Adhesion Energy of Copper Thin Films to SiO2/Si Substrates. *Acta materialia* **1998**, *46*, 6623-6630.

107. Dhara, P.; Sivadasan, A. Near Field Scanning Optical Imaging of Gold Nanoparticles in the Sub-Wavelength Limit. *arXiv preprint arXiv:1705.07416* **2017**.

108. Ezugwu, S.; Ye, H.; Fanchini, G. Three-Dimensional Scanning Near Field Optical Microscopy (3D-SNOM) Imaging of Random Arrays of Copper Nanoparticles: Implications for Plasmonic Solar Cell Enhancement. *Nanoscale* **2015**, *7*, 252-260.

109. NIST Traceable Standard, Filmetrics – A KLA Company, 2019.

110. Filmetrics. Thin Film Analyzer. **2019**, *F40*.

111. Mie, G. Articles on the Optical Characteristics of Turbid Tubes, especially Colloidal Metal Solutions. *Ann.Phys* **1908**, *25*, 377-445.

112. Bohren, C.F.; Huffman, D.R. *Absorption and Scattering of Light by Small Particles*.; John Wiley & Sons, 2008.

113. A, Belay & G, Assefa. **Concentration, Wavelength and Temperature Dependent Refractive Index of Sugar Solutions and Methods of Determination Contents of Sugar in Soft Drink Beverages using Laser Lights**. **2018**, *5(2): 187*.

114. Ghosh, S.K.; Pal, T. Interparticle Coupling Effect on the Surface Plasmon Resonance of Gold Nanoparticles: From Theory to Applications. *Chem. Rev.* **2007**, *107*, 4797-4862.

115. Bahramipanah, M.; Dutta-Gupta, S.; Abasahl, B.; Martin, O.J. Cavity-Coupled Plasmonic Device with Enhanced Sensitivity and Figure-of-Merit. *ACS nano* **2015**, *9*, 7621-7633.

116. Liang, Y.; Lu, M.; Chu, S.; Li, L.; Peng, W. Tunable Plasmonic Resonances in the Hexagonal Nanoarrays of Annular Aperture for Biosensing. *Plasmonics* **2016**, *11*, 205-212.

117. Mock, J.J.; Smith, D.R.; Schultz, S. Local Refractive Index Dependence of Plasmon Resonance Spectra from Individual Nanoparticles. *Nano letters* **2003**, *3*, 485-491.

118. Li, H.; Zeng, Y.; Hu, X.; Zhang, H.; Ruan, S.; Van Bael, M.; Van Haesendonck, C. Thickness-Dependent Magnetotransport: From Multilayer Graphene to Few-Layer Graphene. *Carbon* **2017**, *124*, 193-200.

119. Ringe, E.; McMahon, J.M.; Sohn, K.; Cobley, C.; Xia, Y.; Huang, J.; Schatz, G.C.; Marks, L.D.; Van Duyne, R.P. Unraveling the Effects of Size, Composition, and Substrate on the Localized Surface Plasmon Resonance Frequencies of Gold and Silver Nanocubes: A Systematic Single-Particle Approach. *The Journal of Physical Chemistry C* **2010**, *114*, 12511-12516.

120. Tabassum, S.; Kumar, R.; Dong, L. Plasmonic Crystal-Based Gas Sensor Toward an Optical Nose Design. *IEEE Sensors Journal* **2017**, *17*, 6210-6223.

121. Chang, Y.; Chen, R.; Lee, Y.; Chao, S.; Su, L.; Li, Y.; Chou, C. Localized Surface Plasmon Coupled Fluorescence Fiber-Optic Biosensor for Alpha-Fetoprotein Detection in Human Serum. *Biosensors and Bioelectronics* **2009**, *24*, 1610-1614.